The Investigation of Scanning Tunneling Microscopy and Spectroscopy on High-T_c Superconductors: Cuprates and Pnictides

A dissertation presented

by

Yi Yin

to

The Department of Physics

in partial fulfillment of the requirements

for the degree of

Doctor of Philosophy

in the subject of

Physics

Harvard University

Cambridge, Massachusetts

September 2009

Thesis advisor

Jennifer E. Hoffman

Author

Yi Yin

The Investigation of Scanning Tunneling Microscopy and Spectroscopy on High-T_c Superconductors: Cuprates and Pnictides

Abstract

The discovery of cuprate high-T_c superconductors in 1986 has tremendously impacted the community of condensed matter physics. However, the underlying superconducting mechanism is still not well understood after over twenty years. Recently, the iron pnictide high-T_c superconductors break the monopoly of cuprates. The investigation of pnictides not only provides information on their physical properties and application potential, but also helps to explore the high-T_c superconducting mechanism by comparing with cuprates.

As a surface-sensitive tool to detect microscopic properties of materials with atomic spatial resolution and meV energy resolution, scanning tunneling microscopy (STM) has been proved effective in addressing electronic structures of cuprate superconductors. In this thesis, I present an atomically resolved scanning tunneling spectroscopy study of superconducting $BaFe_{1.8}Co_{0.2}As_2$ single crystals in magnetic fields up to 9 T. At zero field, a single gap with coherence peaks at $\bar{\Delta} = 6.25$ meV is observed with a relative standard deviation 12%, and its implication is discussed in

detail. At 6 and 9 T, we image a stationary but disordered vortex lattice, consistent with isotropic, single-flux quantum vortices. Vortex locations are uncorrelated with strong-scattering surface impurities, implying bulk pinning.

Other work contributing to this thesis is focused on a cuprate superconductor, $Bi_{2-y}Pb_ySi_2CuO_{6+\delta}$. With the density of states (DOS) maps at both zero and nonzero magnetic fields, a division normalization method is applied to separate two characteristic energy scales. We extract a homogeneous hidden small gap coexisting with an apparent inhomogeneous gap. Compared with a recent experiment performed by Boyer *et al.*, the hidden small gap is believed to be a superconducting order and the apparent inhomogeneous gap is referred to the pseudogap phase. Under the magnetic field range in our experiment, a vortex liquid state is proposed. This technique can be extended to detect the possible superconducting information in the Nernst state above T_c.

Contents

Acknowledgments

I would not be able to finish the work described in this thesis without supports from many people. First and foremost, I would like to thank my advisor, Professor Jenny Hoffman, who gives me the chance to enter this fantastic microscopic world using scanning tunneling microscope. Jenny has spent a lot of time working together with us, discussing experimental details and scientific goals. The strict scientific training will guide me all the way in future academic works. The full support of academic activities and endless encouragements also help me build broad communications with other scientists.

I would like to thank all my collaborates in Hoffman group. In particular, it is very lucky to work together with Dr. Martin Zech for two productive years. As one of the best engineers who can always find ways to solve problems, Martin helped me pass frustrated days of building STM system and finally push the instrumental work to beautiful scientific results. I learned a lot from his German-style professionalism in work. His easy-going personality and great sense of humor made the lab work full of pleasant hours. Thank Tess Williams for sharing nights and days of hard work. Her special thinking always sharps my ideas and understandings. I also owe her a lot of professional English editing. To Anjan Soumyanarayanan for enjoyable memories of scientific discussions. Thank Dr. Jeehoon Kim who share with me various knowledge of science and technology. I am also obliged to Dr. Heon-Ick Ha, Liz Main, Adam Pivonka, Ilija Zeljkovic and Nick Litombe for what I have learned from all of you.

I would also like to thank Professor Eric Hudson at MIT, who has always been ready for any of our questions on STM or high-T_c superconductors. Thank Professor Subir Sachdev who gives us many suggestions on data analysis from a theorist point

of view. My work also depends a lot on our sample growers, and I would like to especially thank Prof. Xianhui Chen and his group at USTC for supplying us with 122 pnictide samples. Thank Prof. Hiroshi Ikuta at Nagoya University and Dr. Takeshi Kondo for their Bi-2201 cuprate samples. Thank Dr. Genda Gu at Brookhaven National Laboratory for all the great Bi-2212 samples. Other thanks go to Prof. David Mandrus at Oak Ridge National Laboratory, Prof. Paul C. Canfield at Ames laboratory, Prof. Zhongxian Zhao, Prof. Haihu Wen and Prof. Nanling Wang at Institute of Physics (Beijing) for all the pnictide samples.

It is also pleasant to go across the Oxford street to discuss with STM experts Dr. Jinlin Huang and Dr. Ping Xie, and receive a lot of experimental helps. Thank James MacArthur for helping with all electronic problems and thanks Stan Cotreau and our professional machineshop workers for realizing all the solid designs. Special thanks to Vicky Green who helps to resolve all difficulties in purchasing processes and Barbara Drauschke on administration works.

This work was funded by NSF grant DMR-0508812 and by AFOSR grant FA9550-05-1-0371.

At last, thank my husband, Jianlan Wu, who read all of my papers and helps to make them readable. Thanks for him giving me full support and love all the time. Thank my father whose enthusiasm on techniques makes me feel it is enjoyable to work as an experimentalist, and my mother who makes me love the world and life.

Dedicated to my father,
my mother,
and my husband Jianlan Wu.

Chapter 1

Overview of Superconductivity

Superconductivity has been one of the most fascinating areas of condensed matter physics in the last century. As a phenomenon of conducting electricity without any resistance, superconductivity occurs in certain materials below a material-specific critical temperature T_c. To understand why and how these materials act as superconductors is the main goal of this field, motivated by both fundamental interest and application potential.

1.1 Superconductivity

At zero temperature, all multi-electron systems are in the ground state with the lowest total energy. Normal metals are reliably described by Landau's Fermi liquid theory, which is an effective single particle theory. In momentum space, spin 1/2 electrons (fermions) are filled in up to the Fermi surface with the maximum energy, the Fermi energy E_{F}, by following the Pauli exclusion principle. As the tempera-

ture increases, quasiparticles are excited and scattered to realize thermal equilibrium. Since the system is Fermi degenerate, only electrons in the immediate vicinity of the Fermi surface can be continuously excited. These excited electrons contribute to the thermal energy exchange, and the scattering process which is the source of the electrical resistance under external electromagnetic fields.

Unlike normal metals, superconductors lose their electric resistivity due to disappearance of electronic scattering. Zero electrical resistance was first discovered by H. Kamerlingh Onnes in 1911 [1]. In addition, superconductors exhibit perfect diamagnetization (the Meissner state [2]). These two characteristic electromagnetic properties together determine a superconducting phase below a critical temperature, T_c. The superconducting phase is stabilized by the energy reduction of condensed 'superconducting electrons'. By introducing superconducting electrons that do not scatter in response to the electromagnetic field, F. and H. London [3] interpreted the two characteristic properties of superconductors within the framework of Maxwell's equations. The number density of superconducting electrons, n_s, decreases continuously to zero as the temperature approaches T_c^-, corresponding to a second-order phase transition. Ginzburg and Landau [4] thus introduced an order parameter, $\psi(r) = |\psi(r)|e^{i\varphi(r)}$, with $n_s \propto |\psi(r)|^2$. They extended the London theory by including the spatial variation of $n_s(r)$ in the Ginzburg-Landau equations. The crossover between normal and superconducting states can be studied within their theoretical framework. Now we know that this order parameter, $\psi(r)$, can be treated as the wave function of the macroscopic quantum state in superconductors.

Within these two phenomenological theories, two characteristic lengths, the pen-

etration depth λ_L, and the coherence length $\xi_{\rm GL}$, are introduced. In superconductors under a magnetic field, a circulating supercurrent within a thin surface layer generates a magnetic field that cancels the external field in the bulk. This is defined as the Meissner state. The penetration depth λ_L, the distance to which the external field penetrates into the bulk, is equal to the thickness of the surface layer where the supercurrent exists. The coherence length $\xi_{\rm GL}$ is the length scale over which the superconducting density n_s can change.

The earlier phenomenological theories did not address the microscopic mechanism of superconductivity. This task was resolved by Bardeen, Cooper, and Schriefer (BCS) in 1957 based on a Cooper pairing mechanism [5]. The basic idea of the Cooper pairing picture is that in the vicinity of the Fermi energy, one electron pairs with its time-reversed partner and the Fermi surface is unstable to phonon-assisted pairing between electrons. For a translation-invariant system, such a pair is composed of two electrons with opposite momentums and spins, $\{\mathbf{k}\uparrow, -\mathbf{k}\downarrow\}$, due to the anti-symmetric nature of the pairing electrons. The Cooper pair is thus equivalent to a spin singlet with a zero total momentum. In addition to the 'pairing correlation' within the single Cooper pair, the Pauli principle restrictions induce the correlation between various Cooper pairs. These two effects together lower the total energy in the superconducting state. As a result, there is an energy gap, Δ, in the elementary excitation spectrum of superconductors, and the quasiparticle of excitation is an electron from the break-up of a Cooper pair. The energy gap is proportional to the amplitude of the superconducting order parameter, i.e., $\Delta \propto \sqrt{n_s}$. The density of superconducting electrons, n_s, represents the number of Cooper pairs. The gap in

superconductors arises from the collective behavior of the correlated Cooper pairs, unlike the band gap of semiconductors. As the temperatures increase from zero, the thermal fluctuations of electrons can break the Cooper pairs, which decrease the condensation energy and the gap size. Both n_s and Δ eventually become zero at T_c. The maximum gap size, $\Delta(T = 0\ \mathrm{K})$, and the critical temperature T_c are material dependent. Within the BCS theory, T_c is given by

$$T_c = 1.13\frac{\hbar\omega_c}{k_B}\exp\left[-\frac{1}{N_n(E_\mathrm{F})V}\right], \tag{1.1}$$

where ω_c can be approximated by the Debye frequency in phonon-coupled superconductors, $N_n(E_\mathrm{F})$ is the density of states at the Fermi level, and V is the strength of the electron-phonon interaction. Equation (1.1) works in the weak coupling regime, where $N_n(E_\mathrm{F})V \lesssim 1/4$ [6]. In this limit, the reduced gap, $2\Delta(0)/k_BT_c$, is equal to a constant, 3.52. The strong coupling case was extended by Eliashberg to include the retardation effects in pairing interactions [7]. The critical temperature is related to the atomic mass through the Debye frequency, $T_c \propto \omega_c \propto (\sqrt{M})^{-1}$. The isotope effect, the comparison of the dependence of T_c on isotopic substitution, verified the electron-phonon coupling mechanism for traditional superconductors [8, 9]. Equation (1.1) provides a strategy of improving T_c by adjusting the three parameters, ω_c, $N_n(E_\mathrm{F})$, and V. For example, the intermetallic superconductor $LuNi_2B_2C$ was discovered with a nearly optimized electron-phonon coupling, close to a structure phase transition [10]. Some specific properties of superconductors, such as the influence of impurities on T_c, can be interpreted based on Eq. (1.1). If a material has non-magnetic impurities, the change of T_c is analyzed depending on whether $N_n(E_\mathrm{F})$ varies due to the valence effect, or V is affected by the induced mechanical strain field [11]. Magnetic impurities

dramatically decrease the critical temperature of traditional superconductors [12, 13]. The interaction between the impurity and the electron spin competes with the pair correlation, resulting in the break-up of Cooper pairs and a decrease of n_s.

In response to an external magnetic field H, superconductors exhibit perfect diamagnetization. The kinetic energy arising from the shielding supercurrent increases the free energy by $H^2/8\pi$. This excess free energy becomes equal to the condensation energy when H is increased to a critical value $H_c(T)$ at a fixed temperature T (see Fig. 1.1a). All Cooper pairs are broken, and the superconducting state transfers to the normal state via a first order transition. Superconductors can also carry an externally-applied current, which is persistent similar to the shielding current. With a translational drift momentum q, the Cooper pair is changed to $\{\mathbf{k}+\mathbf{q}/2, -\mathbf{k}+\mathbf{q}/2\}$. The stiffness of the superconducting quantum phase makes the current-carrying state topologically stable, and the energy is difficult to dissipate [14]. Similar to the critical field H_c, a critical current J_c exists, at which the magnetic field induced by the applied current is equal to H_c.

Experimentalists observed that, for one class of superconductors, the external magnetic field is completely expelled as we have discussed. Most pure metals are these so-called Type-I superconductors. However, for another class of superconductors, the magnetic field can partially penetrate the bulk between a 'lower critical field' H_{c1} and an 'upper critical field' H_{c2}, above which the superconductivity completely vanishes (see Fig. 1.1b). This class is defined as Type-II superconductors, usually made of metal alloys or complex oxide ceramics. Type-I and Type-II superconductors are distinguished by $\lambda_L \lesssim \xi_{\mathrm{GL}}$ and $\lambda_L \gtrsim \xi_{\mathrm{GL}}$ (see Fig. 1.1c), respectively. This criterion is

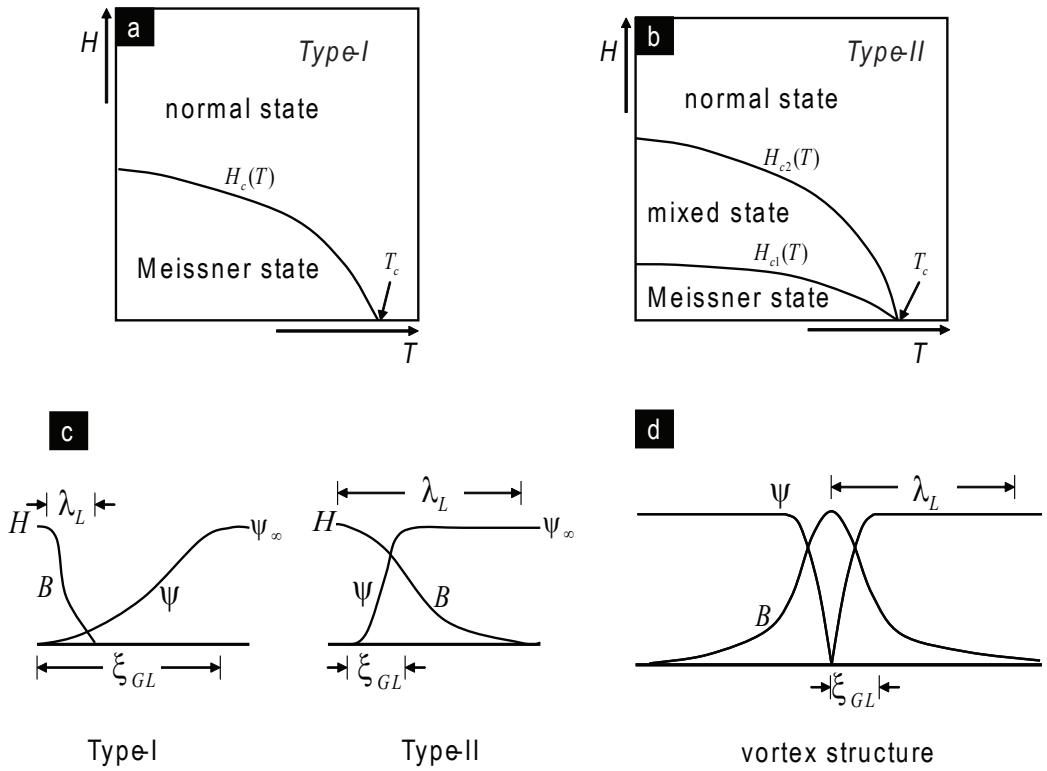

Figure 1.1: The comparison between Type-I and Type-II superconductors. (a) The H-T phase diagram of Type-I superconductors. Below the critical field $H_c(T)$, the superconducting state is in the Meissner state with perfect diamagnetization. (b) The H-T phase diagram of Type-II superconductors. Between $H_{c1}(T)$ and $H_{c2}(T)$, the field partially penetrates through the sample as quantized vortices, resulting in a mixed state. In traditional superconductors, $H_{c1}(T)$ and $H_{c2}(T)$ merge to a single critical point, T_c, at zero field. (c) Schematic diagram of the London penetration depth λ_L and the coherence length $\xi_{\rm GL}$ for Type-I and Type-II superconductors. The total field B penetrates into the sample and gradually decreases from the external field H to zero within a length scale of λ_L. The superconducting order parameter ψ changes from the bulk value ψ_∞ to zero over a length scale of $\xi_{\rm GL}$. Type-I and Type-II superconductors have $\lambda_L \lesssim \xi_{\rm GL}$ and $\lambda_L \gtrsim \xi_{\rm GL}$, respectively. (d) Vortex structure for a Type-II superconductor. Superconductivity is suppressed inside the vortex core with a radius, $\xi_{\rm GL} \ll \lambda_L$.

given by the sign of the wall energy within the interface between the normal state and superconducting state. The negative wall energy introduces a new mixed state in the

H-T phase diagram for Type-II superconductors. In the mixed state, the magnetic field penetrates through the material as quantized vortices with the smallest flux quanta $h/2e$ (see Fig. 1.1d), to produce the maximum wall energy gain. The $2e$ in the flux quanta arises from the pairing electrons. Although the pairing mechanism is unclear for some superconductors, the Cooper pairing picture is still valid, which can be demonstrated by measurement of the $h/2e$ flux quanta.

1.2 High-T_c Superconductors

To date, thousands of superconductors have been discovered. It is always necessary to look at the Periodic Table from time to time, because most of the natural elements have a role in the superconductor families of elements, alloys, or more complicated ceramic compounds.

The critical temperature, T_c, is one of the most interesting parameters for superconductors from an application standpoint. Therefore, the discovery of a copper-based superconductor, LaBaCuO, with $T_c > 30$ K, kindled excitement in the community [15]. Afterwards, many similar copper-oxide superconductors with higher T_c were synthesized, and the current record is 164 K in the mercury-based copper oxide under high pressure [16]. Because these high-T_c superconductors all have CuO_2 planes in common, they have been named the cuprate family.

The BCS theory is applicable to all the 'conventional' superconductors with phonon-coupled Cooper pairs. The mechanism of other 'unconventional' superconductors (e.g. the cuprates) is still under investigation. Phenomenologically, the 'unconventionality' may also be embodied in the symmetry nature of the pairing electrons. For

conventional superconductors, the Cooper pair is a spin singlet state ($S = 0$) with a zero total angular momentum ($L = 0$). The symmetries of the spin S and angular momentum L are not necessarily the same in unconventional superconductors. For an unconventional spin singlet pair, $L/\hbar$ is possibly an even number, e.g., $L = 2\hbar$ (d-wave) if the $L = 0$ state with the lowest energy is disabled. To detect such an anisotropic gap in the momentum space, angle-resolved photoemission spectroscopy (ARPES) has been a crucial technique. Based on the photoelectric effect, ARPES can measure the energy and momentum of the emitted electrons from the sample and determine the electronic structure around the Fermi surface. A $d_{x^2-y^2}$ gap has been experimentally proven for the cuprates by ARPES [17, 18] and further phase sensitive techniques [19, 20]. Physically, a $d_{x^2-y^2}$ gap means that electrons traveling different directions experience different potentials. The spin singlet state is not the only choice for the two-electron pair; the spin triplet state ($S = 1\hbar$) is possible with an odd angular momentum, e.g., $L = \hbar$ (p-wave), which is observed in a peculiar ruthenate oxide, Sr_2RuO_4 [21].

There are three prototype cuprates, $La_{2-x}Sr_xCuO_4$ (LSCO, L-214), $Bi_2Sr_2CaCu_2O_{8+\delta}$ (BSCCO, Bi-2212) [22], and $YBa_2Cu_3O_{7-\delta}$ (YBCO, Y-123) [23]. The abbreviation names in parentheses for the different compounds are based on the initial letters or the stoichiometry of the elements. The crystal structure of the cuprates is a perovskite type, and we use the Bi-2212 as an example in Fig. 1.2a. In the copper oxide plane, the copper ion is surrounded with a square of four oxygen ions, and above each Cu ion there is an 'apex oxygen' from the SrO plane. Each Cu constitutes a tetrahedron with neighboring oxygens. There are calcium atoms sandwiched in between two con-

secutive CuO_2 planes. Along the c-axis direction, the CuO_2 bilayer alternates with the SrO plane and the BiO plane.

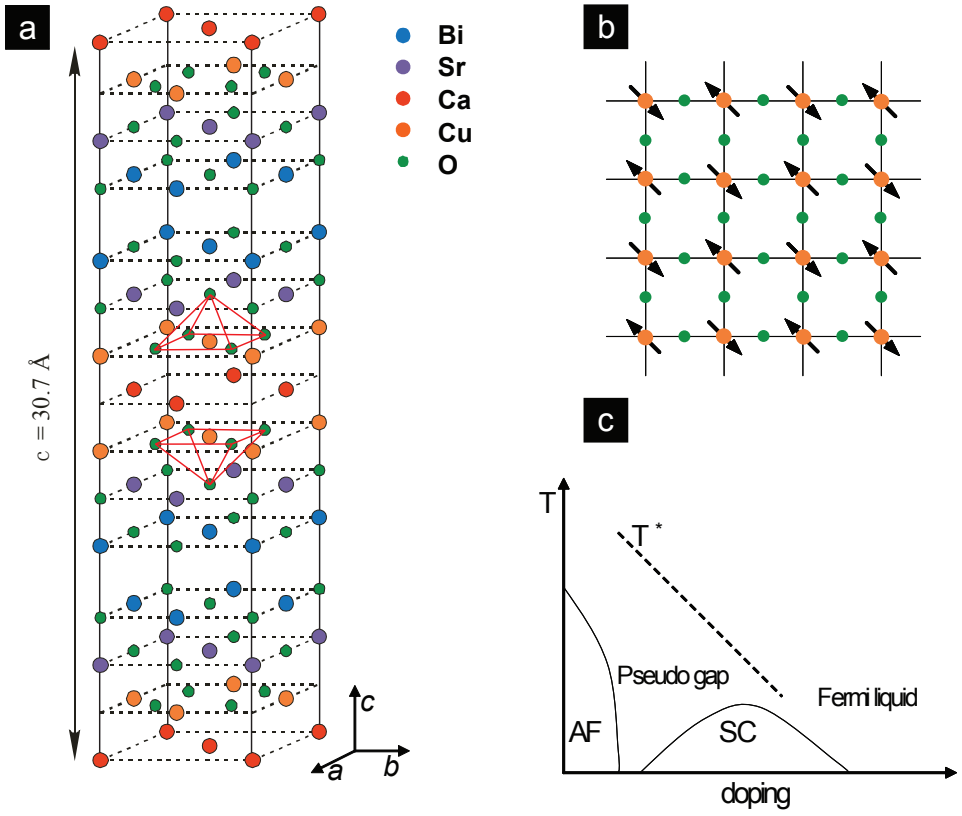

Figure 1.2: (a) A unit cell of $Bi_2Sr_2CaCu_2O_{8+\delta}$. The typical room temperature lattice constants are $a = b = 5.4$ Å and $c = 30.7$ Å. The average Cu-Cu distance is 3.8 Å. (b) Schematic diagram of a single CuO_2 plane. The black arrow represents the spin direction of Cu ions in the antiferromagnetic state. (c) A generic phase diagram for the cuprates. Above the dome-shaped superconducting regime, there is a pseudogap phase, whose properties will be discussed in Chap. 5.

For the parent cuprates, each Cu ion has one electron occupying the $d_{x^2-y^2}$ orbital state. The $d_{x^2-y^2}$ electrons hybridize with the oxygen p_x/p_y orbital, resulting in a half-filled band based on the normal band theory. For this single band of quasi-2D

electronic structure with weak dispersion along the z axis, the expected projection of the Brillouin zone on the (k_x, k_y) plane has the diamond shape shown in Fig. 1.3a. But due to the strong Coulomb interaction between d electrons, a single d electron is localized on each Cu ion. The Cu^{2+} ion has a $\hbar/2$ spin, hence, a magnetic moment. An effective single-band Mott-Hubbard model describes the parent compound as a Mott insulator [24]. Furthermore, the virtual hopping between the neighboring sites makes the antiparallel alignment of spins energy-favorable, resulting in an antiferromagnetic (AF) order. In the generic phase diagram in Fig. 1.2c, the AF state is gradually suppressed and the superconducting phase appears when the doping value increases. In the dome-shaped superconducting regime, the sample with maximum T_c denotes optimal doped. Correspondingly, on the left and right of the optimal doping point, superconductors are referred to as underdoped and overdoped, respectively. Doping is realized by the elemental substitution or by adjusting the oxygen quantity for different families of cuprates. For BSCCO, oxygen atoms are doped in between two BiO layers by annealing in oxygen gas. Every oxygen ion accepts two electrons, leaving holes as charge carriers transferred to the CuO_2 planes.

For superconducting samples, especially for optimal and overdoped samples, ARPES can measure the Fermi surface of the 2D-Brillouin zone in the normal state, a sketch of which is shown in Fig. 1.3b. For this Brillouin zone of hole-doped superconductors, the gray area covers the occupied electron state, which shrinks with increased doping. The d-wave gap distribution around the Fermi surface is approximated by a cosine function $\Delta_k = \Delta_0 \cos(2\theta)$, where θ is the Fermi surface angle. Since the measured gap is zero on the cross point between the $(0,0)$-(π,π) line and the Fermi surface,

$(0,0)$-(π,π) is referred to as the nodal direction and the cross point is called the nodal point. Correspondingly, Δ_0 is the maximum gap size on the antinodal point. The ARPES measurement of such a d-wave superconducting gap from Ding *et al.* [18] is displayed in Fig. 1.3c.

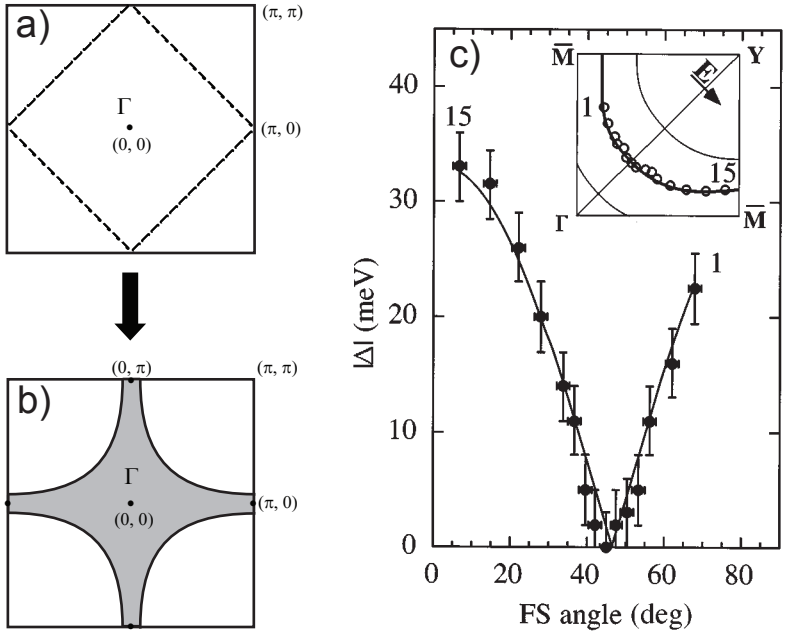

Figure 1.3: The Fermi surface and the d-wave gap of cuprate superconductors. (a) The Fermi surface at half filling shows a diamond Brillouin zone on the (k_x, k_y) plane. In reality, the parent compound is a Mott insulator because the electrons are localized by strong Coulomb interactions. (b) Sketch of the Fermi surface for doped cuprates. In both (a) and (b), the wavevectors k_x and k_y are shown modulo $2\pi/a_0$, where a_0 is the lattice constant of the CuO_2 plane. (c) Superconducting gap vs. angle along the Fermi surface for a Bi-2212 sample with $T_c = 87$ K, together with a d-wave fit. Along the Fermi surface in the inset, the authors label the momentum points, where the ARPES spectra are taken. The nodal and antinodal points are referred to as the cross point between the $(0,0)$-(π,π) line and the Fermi surface, and the cross point between the $(0,\pi)$-(π,π) line and the Fermi surface, respectively. The nodal direction has a 45° Fermi surface angle. From Ding, *et al.* [18].

Because of the peculiar Mott insulator nature of parent compounds, some theorists

argue that the BCS theory is not a good foundation for high-T_c superconductors. The new models, such as the resonating valence bond (RVB) model and related spin-charge separation picture [25, 26], are proposed based on the competition between Coulomb interaction and delocalization for doped Mott insulators. How the Fermi surface evolves from a Mott insulator state to a Fermi liquid when the doping is increased is a hot topic even today [27, 28, 29, 30, 31, 32]. Phenomenologically, another focus point for the cuprates is the role of fluctuations. The comparison between the condensation energy in the coherence volume ${\xi_{ab}}^2\xi_c$ and the thermal energy $k_{\mathrm{B}}T$ provides a rough check of the effects of thermal fluctuations. As a Type-II superconductor, the cuprates have small coherence lengths. Both the crystal and electronic structure show that the cuprates are extremely anisotropic compounds, with in-plane $\xi_{ab} \approx 2$ nm and the c-axis $\xi_c \approx 0.1$ nm for Bi-2212 [33]. The combination of quasi-2D structure, small coherence length and high critical temperature implies a strong thermal fluctuation effect for the cuprates. As a quantum coherent phase, the phase fluctuations of the superconducting order is also considered [34]. The strong fluctuations may change how the superconducting order is destroyed at T_c from predictions of mean-field BCS theory.

In spite of the controversy surrounding the theoretical treatment on the cuprates, it is generally accepted that magnetic interactions play an important role in the superconducting mechanism. A schematic picture is that the hopping of a single hole leaves a trail of ferromagnetic spins. If a second hole moves along the previous trace, the spins are changed back to the AF state. Intuitively, to save the energy gain of the AF state, two holes are coupled as a pair by dynamic spin fluctuations.

However, neither a quantitative theory nor definitive experimental results regarding the magnetic interaction are available as of today.

Before 2008, the story of high T_c superconductors would end here, disregarding other peculiar superconductors, e.g., the heavy Fermion systems. Recently, a totally new class, the iron-based superconductors (FeSC) has emerged, which will be discussed in the next section.

1.3 Iron-Based Superconductors

One of the most exciting events in condensed matter physics in 2008 was the discovery of superconductivity in iron-arsenic based compounds [35, 36, 37, 38, 39, 40]. After the initial fluorine doped $LaFeAsO_{1-x}F_x$ with a superconducting transition temperature of $T_c = 26$ K [35], superconductors with T_c up to 56 K have been obtained by replacing lanthanum with other rare earth elements of smaller ionic radii [37, 38, 39] or by Th doping [41]. Due to their stoichiometry, these compounds are referred to as 1111 type. Subsequently, the so-called 122 type, non-oxide AFe_2As_2 (A=Ba [42, 43], Sr [44, 45], Ca [46, 47, 48, 49, 50], Eu [51] or $(Sr_4Sc_2O_6)Fe_2P_2$) was also found to be superconducting when appropriately doped or pressurized. The 111 type AFeAs (A=alkali metals) [52, 53, 54] and the 11 type iron chalcogenides, prototype $Fe_{1+x}Se$ [55, 56], have been subsequently added to the list.

The rapid progress of this new field reminds us of the similar story more than twenty years earlier with the cuprates. Both families of materials become superconducting after chemical doping of antiferromagnetic parent compounds, and both have dome-shaped superconducting phase diagrams. There is new hope that investigation

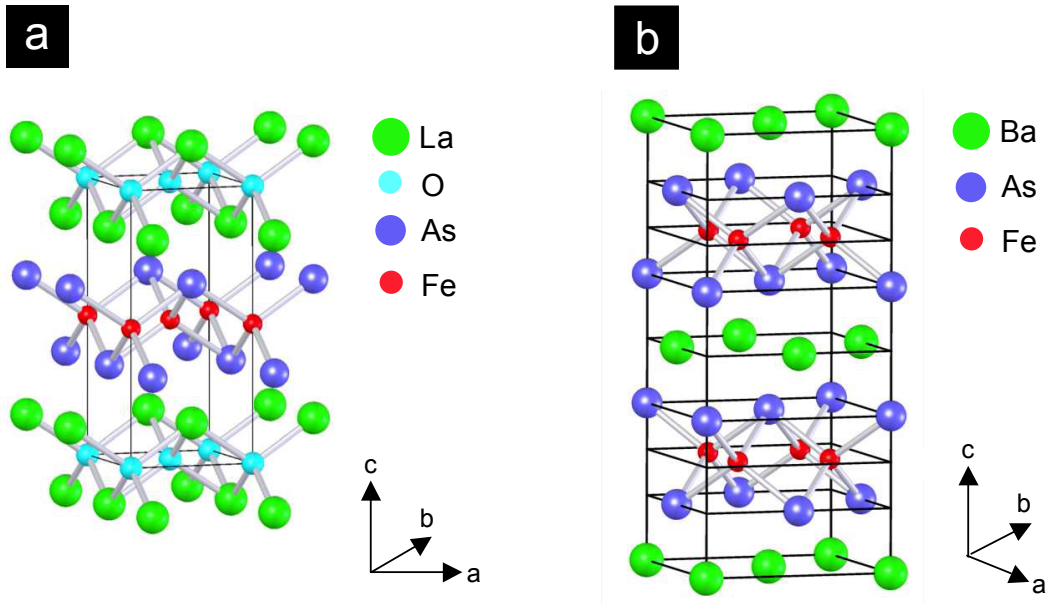

Figure 1.4: Crystal structure of the pnictides. (a) Tetragonal LaFeAsO 1111 type with room temperature lattice constants $a = b = 4.03$ Å and $c = 8.73$ Å[35]. (b) Tetragonal $BaFe_2As_2$ 122 type with room temperature lattice constants $a = b = 3.96$ Å and $c = 12.39$ Å. The FeAs layer is the effective superconducting layer in both compounds.

of the FeSC as a 'foil' for cuprates will eventually lead to a fundamental understanding of high-T_c superconductors. However, significant differences have been found to exist between these two classes of materials after exploring more properties in detail.

The parent compound of the cuprates is a Mott insulator. The neighboring oxygen atoms in the CuO_2 plane lead to a long Cu-Cu distance. Therefore, the d electrons are more localized with a strong Coulomb interaction. For the iron-based materials, the basic structure feature of the FeAs is a face sharing tetrahedra (Fig. 1.4). The Fe-Fe bonding plays a dominant role in the band formation and magnetic interac-

tions [57], albeit a modest Fe-As hybridization. Correspondingly, all five Fe d orbitals contribute to the electronic structures near E_{F}. The electronic structures are reasonably calculated in an itinerant picture, by density functional theory (DFT) or local density approximation (LDA) [58]. The Fermi surface (FS) consists of two hole-like pockets around the center point (Γ) of the Brillouin zone (BZ) and two electron-like pockets around the corner point (π, π) of the BZ [57] (see Fig. 1.5a). This FS topology has been observed by different angle resolved photoemission spectroscopy (ARPES) measurements [59, 60, 61, 62]. The metallic state of the FeSC parent compound is confirmed by quantum oscillation experiments [63, 64] and measurements of metallic band dispersion [59, 65]. In this itinerant picture, the AF state of the parent compounds has a different origin. The multi-band FS shows that cylindrical hole and electron sections meet a nesting condition. The spin density wave (SDW) instability with a commensurate translation momentum (π, π) induces a collinear spin pattern of the AF SDW order, which has been experimentally proven [66].

The stark difference between parent compounds suggests that the doped Mott insulator model is not a good starting point for the FeSC. The role of spin fluctuations is still paramount because of the proximity of the superconducting state to the AF SDW order. The spin fluctuations work as the same driving force to induce the SDW and superconductivity as the Fermi surface instability. Doping changes the relative size of the hole and electron FS sections, and weakens the nesting conditions for the SDW order. As the SDW order is suppressed, superconductivity is induced by spin fluctuations. For the superconducting order, the strong interaction also occurs at (π, π) and favors opposite sign order parameters between the center FS and the corner

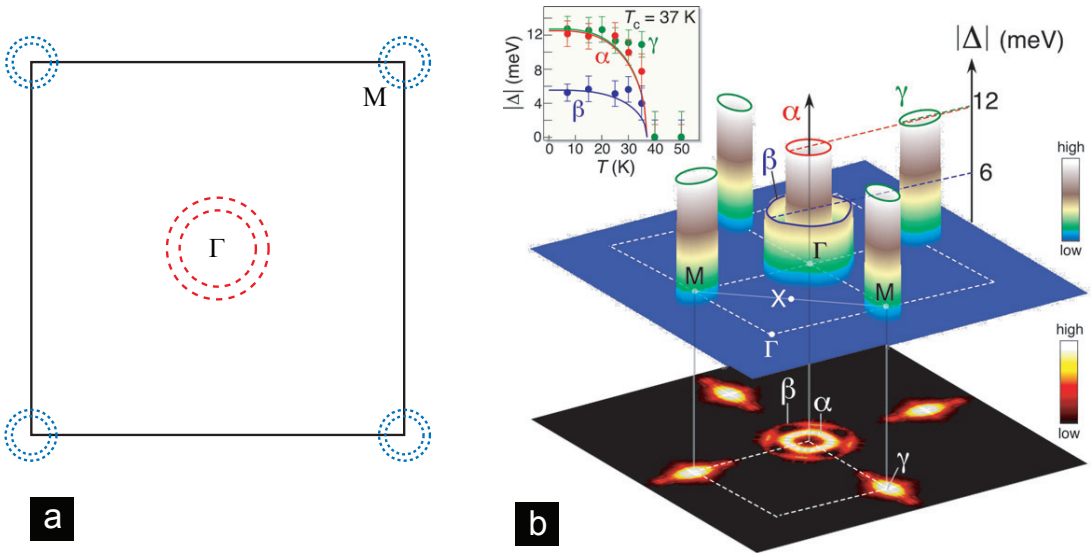

Figure 1.5: The Fermi surface of the FeSC and the superconducting gap measurement. (a) A sketch of the Fermi surface, showing two concentric hole pockets around Γ and two electron pockets around M (π, π). (b) The amplitude of the $s_{\pm}$ superconducting gaps measured in ARPES. Around both hole FS and electron FS, the superconducting gaps have isotropic distributions. From Ding, *et al.* [62].

FS. This superconducting order parameter is the $s_{\pm}$ state proposed by Mazin [67]. In the $s_{\pm}$ state, isotropic s-wave gaps open around both hole FS and electron FS, which has also been confirmed by the ARPES measurements [60, 62] (see Fig. 1.5b). For the phase detection, the IBM group used a superconducting loop consisting of niobium and a polycrystalline $NdFeAsO_{0.88}F_{0.12}$ to detect half and single flux-quantum jumps. Their results prove that the pairing in $NdFeAsO_{0.88}F_{0.12}$ is a spin-singlet with even-parity, and there is a sign change in the superconducting order parameter [68].

The goal of this thesis is to use scanning tunneling microscopy (STM) to study the superconducting order parameters in both materials. Our results, together with other emerging discoveries in the field, may help to unravel the fundamental physics

of both of these families in the near future.

Chapter 2

The Principles of STM and STS

There is a hierarchy in the principles governing our physical world. In our everyday life with a macroscopic scale, Newtonian mechanics dominates. When entering the microscopic world, quantum mechanics starts to be crucial. That an electron tunnels through an energy barrier larger than its kinetic energy is a quantum phenomenon forbidden in Newtonian mechanics. The STM is a surface measuring technique based on quantum tunneling. In this chapter we will start from the theoretical frame of general electron tunnelings, delve into the working principles of STM/STS, and discuss the standard data acquisition method in our experiments.

2.1 Theory of Electron Tunneling

For a single electron tunneling from one electrode through a potential barrier to another electrode, quantum mechanics determines that the transmission probability of the electron decreases exponentially with the thickness of the barrier, d. The

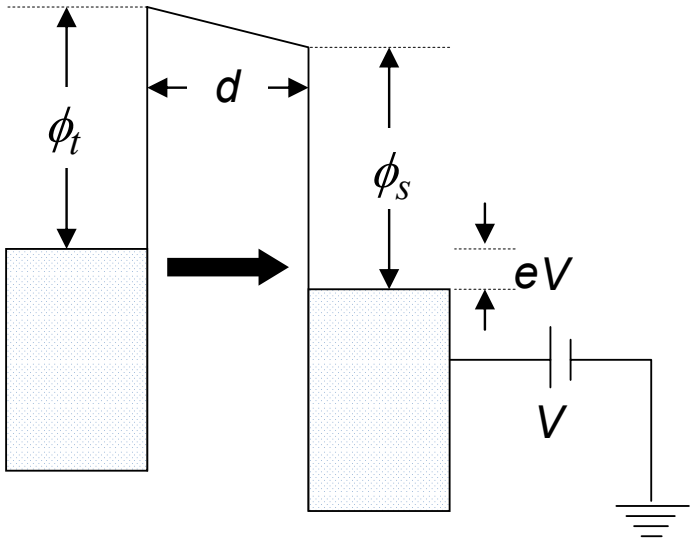

Figure 2.1: Energy diagram for a tunneling junction with a bias voltage V_s applied to the sample. ϕ_t and ϕ_s are the work functions of two electrodes, e.g. the tip and sample, respectively.

potential energy (within the range of several electron volts) of a vacuum or insulator barrier is related to the work functions of both metallic electrodes. With a nanometer scale d and a small bias voltage V between two electrodes (see Fig. 2.1), a nonzero net current runs through the barrier,

$$I \propto e^{-2\kappa d}; \quad \kappa = \sqrt{2m(\phi - \varepsilon_k)}/\hbar \approx \sqrt{2m\phi}/\hbar, \tag{2.1}$$

where ϕ is the average work function of both electrodes ($\phi = \frac{1}{2}(\phi_t + \phi_s)$), ε_k is the kinetic energy of the electron, and m is the mass of the electron.

For practical electron tunneling, Bardeen developed a many particle point of view [69], based on time-dependent perturbation theory and Fermi's golden rule. The tunneling current is expressed as

$$I = -\frac{4\pi e}{\hbar} \int_{-eV}^{0} |M|^2 \rho_t(\varepsilon)\rho_s(\varepsilon + eV)\,(f(\varepsilon) - f(\varepsilon + eV))d\varepsilon, \tag{2.2}$$

where ρ_t and ρ_s refer to the density of states (DOS) of two electrodes, e.g. the tip and sample in the STM, and M is the tunneling matrix. The Fermi distribution of the electron energy away from the Fermi energy ($\varepsilon = E - E_{\mathrm{F}}$) is given by

$$f(\varepsilon) = \frac{1}{1 + e^{\varepsilon/k_{\mathrm{B}}T}}. \tag{2.3}$$

For general tunneling phenomena, two electrodes are taken as independent systems. The tunneling process is properly approximated by equilibrium theory, since the time scale between consecutive tunneling events is much longer than the relaxation time of the quasiparticle [70]. Within this approximation, the tunneling matrix M is the expectation value of the single-particle transition probability across the barrier, and can be approximated as the exponential function in Eq. (2.1). If the t electrode is chosen with a flat DOS near the Fermi energy, both $\rho_t(\varepsilon)$ and $|M|^2$ are constants, and the tunneling current simplifies to

$$I = -\frac{4\pi e}{\hbar} e^{-2\kappa d} \rho_t(0) \int_{-eV}^{0} \rho_s(\varepsilon + eV) \left(f(\varepsilon) - f(\varepsilon + eV)\right) d\varepsilon. \tag{2.4}$$

At low temperatures, the Fermi function has a sharp cutoff at the Fermi energy. Equation (2.4) provides an energy window where electrons can elastically tunnel from the occupied state of one electrode to the empty state of the other one. The tunneling current is proportional to the integral of the DOS of the sample.

At a constant d, the bias voltage dependence of the tunneling current provides spectral information of the sample electrode. By taking the derivative of I with respect to V, the dI/dV conductance is written as a function of the bias voltage:

$$\frac{dI}{dV}(V) = \frac{4\pi e^2}{\hbar} e^{-2\kappa d} \rho_t(0) \int_{-eV}^{0} \rho_s(\varepsilon + eV) \frac{\partial f}{\partial \varepsilon}|_{\varepsilon=0} d\varepsilon, \tag{2.5}$$

where $(\partial f/\partial\varepsilon)|_{\varepsilon=0}$ is a bell-shaped function with half-width $k_{\mathrm{B}}T$ centered on the Fermi energy. At zero temperature, $(\partial f/\partial\varepsilon)$ is a Dirac δ-function and the dI/dV spectrum leads directly to the DOS of the sample. At low temperatures, the DOS is slightly smeared by the temperature broadening. Overall, the tunneling current and dI/dV spectrum provide a tool to measure the electronic structure of the sample around the Fermi level.

Giaever pioneered the use of electron tunneling to detect the energy gap of a superconductor [71]. When he brought this idea to his colleagues, everyone told him that the superconducting gap is a many-body effect and cannot be measured by a single particle spectrum [72]. The experimental success of the superconducting gap measurement leads to the so-called semiconductor model [73], in which the superconductor is represented by the density of independent quasiparticles,

$$N_s = N_0 \frac{|\varepsilon|}{\sqrt{\varepsilon^2 - \Delta^2}}, \tag{2.6}$$

where N_0 is the normal state DOS, ε is the energy away from the Fermi energy and Δ is the superconductor gap size. An energy diagram of the superconductor/insulator/normal metal (SIN) planar junction and the corresponding DOS of the superconductor are shown in Fig. 2.2. The traditional superconductor with a s-wave gap is assumed in both Eq. (2.6) and Fig. 2.2.

In the planar tunnel junction configuration, two thin metal films are fabricated as electrodes and a thin oxide layer is the insulator barrier. Giaever chose the planar junction to avoid the vibration problems of a vacuum tunneling barrier [72]. After 21 years, vacuum tunneling was realized in a new instrument, the scanning tunneling microscope, which will be discussed in the next section.

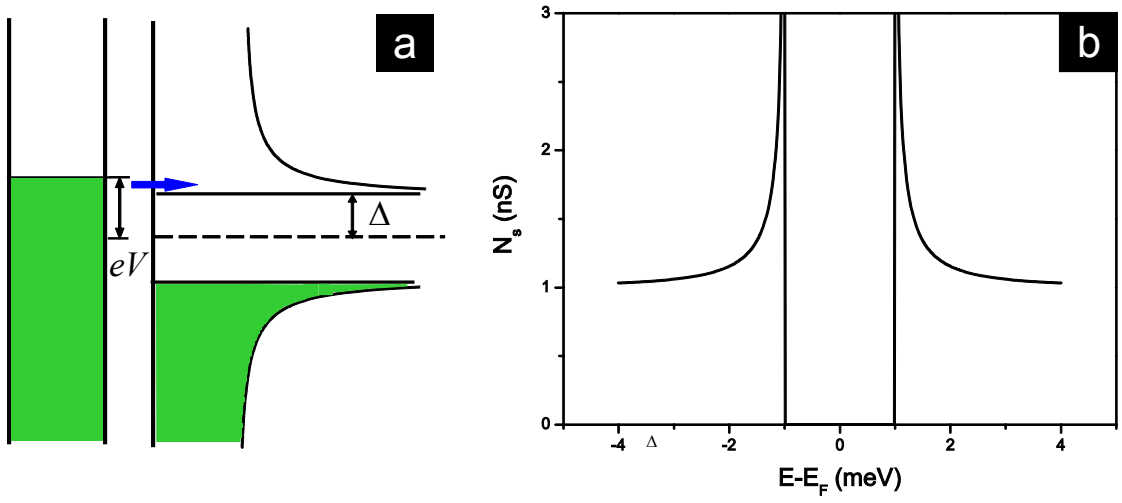

Figure 2.2: The semiconductor model of electron tunneling in a SIN planar junction. (a) The density of states is plotted horizontally for the superconducting electrode on the right and the metallic electrode on the left. Energy is along the vertical axis. The bias voltage is eV and the superconducting gap is Δ. (b) For an s-wave superconductor, N_s is plotted as a function of ε based on Eq. (2.6). The superconducting gap Δ is 1 meV and N_0 is 1 nS.

2.2 Data Acquisition in STM

In a SIN planar junction, the measured dI/dV spectrum is the spatially averaged DOS for the underlying superconductor. In the early 1970's, a device called a topografiner [74], which employs field emission from a scanning tip to a conducting sample as a surface sensing technique, was developed. In 1981, Binnig and Rohrer [75] combined electron tunneling with the topografiner, and invented the scanning tunneling microscope. In STM, there is a sharp metallic tip, which is scanned across an electrically conducting sample surface at a very small separation, typically a few angstroms. Both the tip-sample separation and the lateral position can be varied with a sub-Å precision by means of a piezoelectric scanner (see Fig. 2.3). When a negative

bias voltage is applied to the sample, electrons in occupied states of the sample will tunnel through the vacuum barrier to the empty states of the tip, resulting in a measurable tunneling current. A positive bias voltage applied to the sample will likewise cause electrons to tunnel from tip to sample. The tunneling current in Eq. (2.4) is generalized to the STM application by replacing $\rho_s(\varepsilon - eV)$ with $\rho_s(r, \varepsilon - eV)$, where r is the spatial coordinate of the sample position below the tip. As for Eq. (2.5), the dI/dV spectrum is proportional to the local DOS (LDOS) of the sample in the STM. The STM tips are usually made of platinum (Pt), platinum-iridium (PtIr) alloys, and tungsten (W), which all have a featureless DOS near the Fermi energy E_{F}.

The tunneling matrix M is more complicated in the STM than that in the planar tunnel junction [76, 77]. The main distinction is the weighting of different parts of the Fermi surface on the dI/dV spectrum. In Eq. (2.1), the effect of ε_k is that the current is dominated by the tunneling electrons with the largest k_z (normal to the junction surface), and the terms with smaller k_z are exponentially suppressed. A small part of the Fermi surface with the largest k_z contributes to the measured dI/dV spectrum. In STM, the small size tip provides a lateral confinement of the tunneling electrons. By virtue of the Heisenberg uncertainty principle, all the states around the Fermi surface with different lateral momenta are weighted. As a result, z-axis STM tunneling can measure two-dimensional materials with electronic states in the xy-plane. For cuprate superconductors, there is a d-wave gap distribution around the Fermi surface in the (k_x, k_y) plane, with a cosine function as shown in Fig. 1.3. For cuprate superconductors, N_s is ideally expressed as,

$$N_s(\theta) = N_0 \ \mathrm{Re}\left[\frac{\varepsilon - i\Gamma}{\sqrt{(\varepsilon - i\Gamma)^2 - (\Delta_0 \cos(2\theta))^2}}\right], \tag{2.7}$$

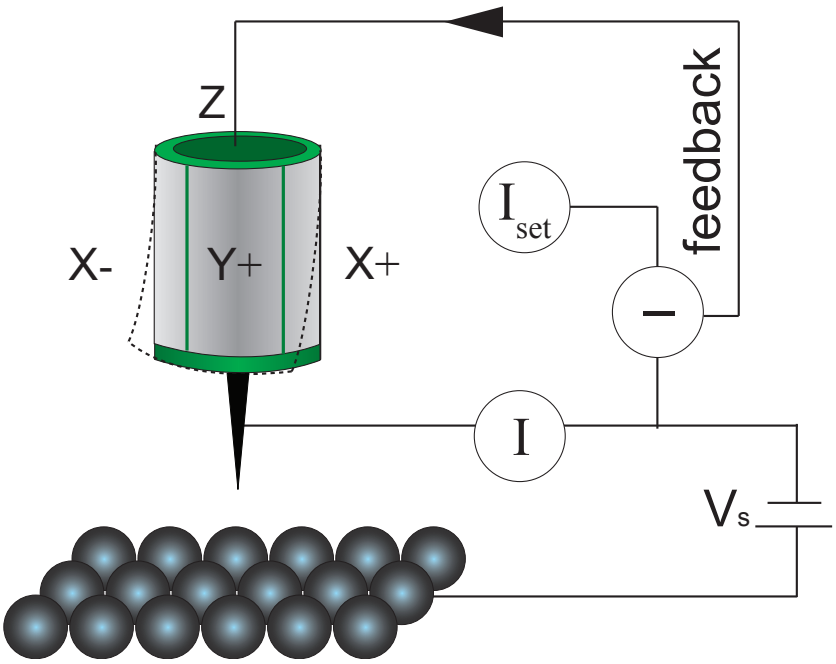

Figure 2.3: A schematic picture of STM. A voltage V is applied between the conducting sample surface and a sharp metallic tip, leading to a measurable tunneling current I with exponential dependence on the tip-sample distance. If this current is kept constant by a feedback loop while the STM tip is scanned over the surface, the surface topography and/or variation in the local DOS can be revealed. The feedback loop works by comparing the real-time current I with the setpoint I_s, and correspondingly driving the piezo tube along z-axis to keep $I = I_s$.

where Δ_0 is the maximum gap around the anti-nodal region in the momentum space and Γ is the scattering broadening parameter. The STS spectrum is an average of $N_s(\theta)$ given by $dI/dV \propto \int N_s(\theta)d\theta$. An energy diagram for STM tunneling from a normal metal tip to a d-wave superconductor is shown in Fig. 2.4. In contrast to Fig. 2.2, electrons can tunnel starting from zero energy. The d-wave feature in the momentum space becomes a V-shape spectrum close to the Fermi energy and the position of the sharp coherence peaks is the maximum gap size Δ_0.

The operating modes of the STM and the data-acquisition methods in our experi-

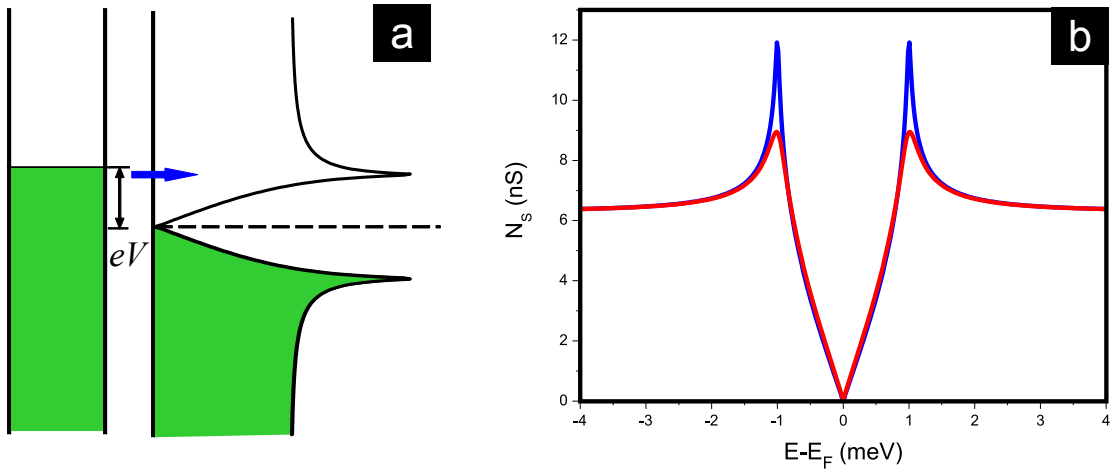

Figure 2.4: STM tunneling from a normal metal tip to a d-wave superconductor. (a) Density of states vs. energy. The bias voltage is eV. (b) N_s for a d-wave superconductor, based on Eq. (2.7). The superconducting maximum gap Δ_0 is 1 meV. The blue and red curves are spectra with Γ of 0.02 meV and 0.1 meV, respectively. Strong scattering suppresses the coherence peaks to smooth ones.

ments will be discussed in the following paragraphs. Since STM is a surface sensitive technique, the surface quality of a material limits its applicability. We will give examples using a prototype cuprate, BSCCO, with an atomically flat cleaved surface. $Bi_2Sr_2Ca_{n-1}Cu_nO_{2n+4+\delta}$ can have a variable number of CuO_2 planes in the unit cell, e.g., the bilayer Bi-2212 ($n = 2$) and single layer Bi-2201 ($n = 1$). BSCCO has two BiO mirror planes, weakly bonded by the van der Waals force (see Fig 2.5). By cleaving single crystal samples between two BiO planes, the flat and neutral BiO surfaces are exposed. The top two planes, BiO and SrO, are insulating. The dI/dV spectrum is believed to be from the next superconducting CuO_2 plane, 4.5 Å below the surface. On the other hand, the BiO plane is observed in topographic images, probably due to the diffraction of electrons by the BiO and SrO planes.

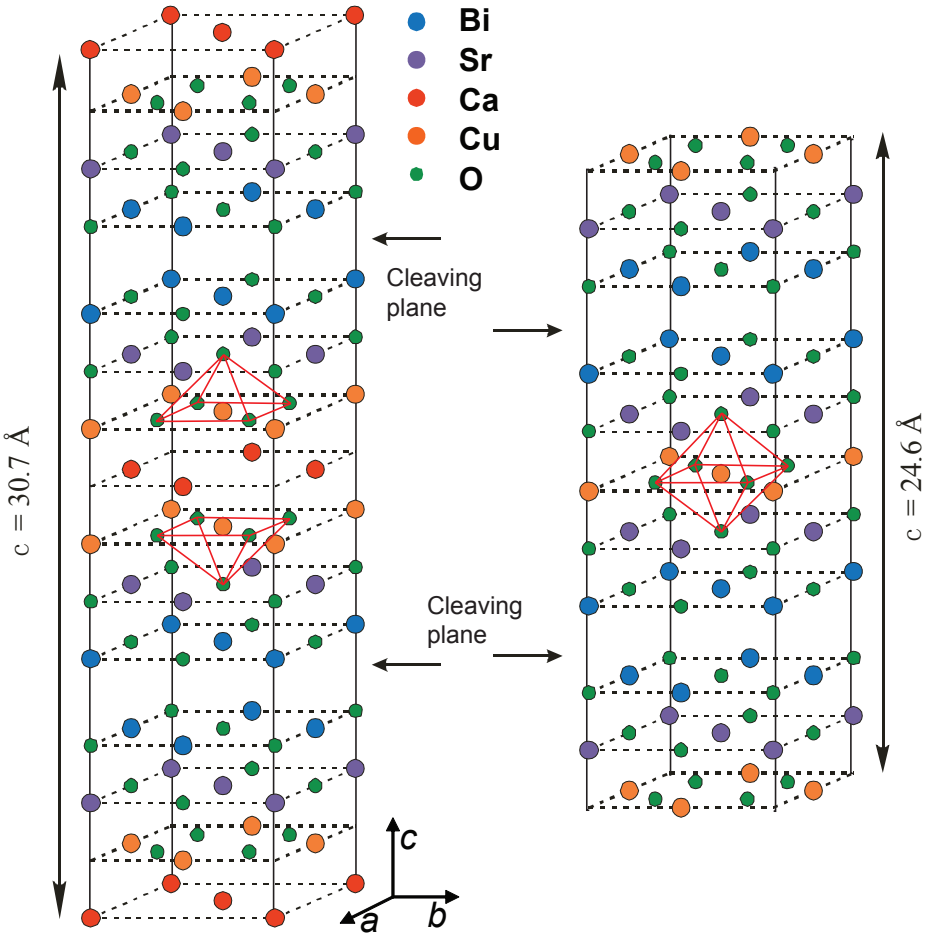

Figure 2.5: The crystal structure of two BSCCO samples: Bi-2212 and Bi-2201. The cleaving planes are shown for both structures.

Topographic image

STM is a tool special in its ability to provide real-space images with atomic resolution. The xy-plane resolution is mainly limited by the apex geometry of the tip. When the tip approaches the surface, a feedback loop control is activated to keep the tunneling current constant (see Fig. 2.3). While the STM tip is scanned over the

sample surface with a set current, the tip vertical position is adjusted accordingly, and the tip height $z(x, y)$ is recorded. This technique is referred to as constant-current topographic mode. Based on Eq. (2.4), the current depends on the tip-sample distance and the integral of the LDOS. In the case of homogeneous elemental metals, this integral is a constant. The image of $z(x, y)$ thus records the topography of the sample surface. If the integral of LDOS varies spatially, the image contains a mixture of DOS and topographic information. With the appropriate tunneling parameters, however, the topography dominates the image. Two independent parameters determine the tunneling conditions: the bias voltage V_s applied to the sample, and the tunneling current setpoint I_s. The tip-sample distance and the junction resistance ($R_t = V_s/I_s$) are specified by these two parameters. In practice, we often start with a bias voltage $V_s = -100$ mV and a set current $I_s = 100$ pA to define an R_t within the GΩ range. The absolute value, $|V_s| = 100$ mV, is much smaller than the usual work function of metal samples (~ 5 V), making the tunneling approximation applicable. For all the high-T_c superconductors we have studied, the topographic images have no dependence on bias polarity within our bias voltage range. The negative bias voltage is chosen to emphasize that the integration of LDOS is over the occupied states of the sample. The bias value, $V_s = -100$ mV, is also far from the energy scale of the superconducting gap ($\sim \pm 40$ meV).

Two topographic images of Bi-2212 and Bi-2201 are shown in Fig. 2.6, both recorded with $V_s = -100$ mV and $I_s = 100$ pA. Figure 2.6a is a 40-nm-square image of optimally doped $Bi_2Sr_2CaCu_2O_{8+\delta}$ (Bi-2212 with $T_c = 91$ K), and the high-resolution view of the center 5-nm-square area is displayed in the inset. To obtain a consistent

interpretation, a topographic image has to be compared with information from other techniques, e.g., the crystal structure measured by the x-ray diffraction. Now it is generally accepted that the Bi-2212 image reveals the BiO plane with the distorted Bi square lattice. One distinctive feature is the incommensurate supermodulation along the diagonal direction of the Bi lattice, originating from the structural mismatch of alternating layers [78, 79]. The dark-atom rows along the supermodulation ridges (like $ signs) may arise from missing or suppressed atoms [70]. For comparison purpose, a 20-nm-square image of an overdoped $Bi_{2-y}Pb_ySi_2CuO_{6+\delta}$ (Pb-Bi2201 with $T_c = 18$ K) is shown in Fig. 2.6b. The Pb atoms replace some Bi atoms, displayed as bright spots in the Bi lattice. The incommensurate supermodulation structure is quenched by Pb dopants [80]. For an atomically-resolved topographic image, the pixel numbers are often chosen to be more than four pixels per atom. The scan speed is limited by the bandwidth of the feedback loop.

Scanning Tunneling Spectroscopy (STS)

In addition to revealing the geometrical surface structure of a sample, a more important application of STM is to resolve the local electronic structure (LDOS) of the sample as a function of energy away from the Fermi level. As shown in Eq. (2.5), dI/dV is a good measure of the sample LDOS under ideal conditions, which is the foundation of STS. To map the LDOS, a grid of point spectra are taken. Before each point spectrum measurement, the tip-sample distance d is fixed with the feedback loop on (the set bias voltage V_s and the set current I_s). After turning off the feedback, we change the bias voltage V from V_s to V_{start}, sweep it through a set of discrete

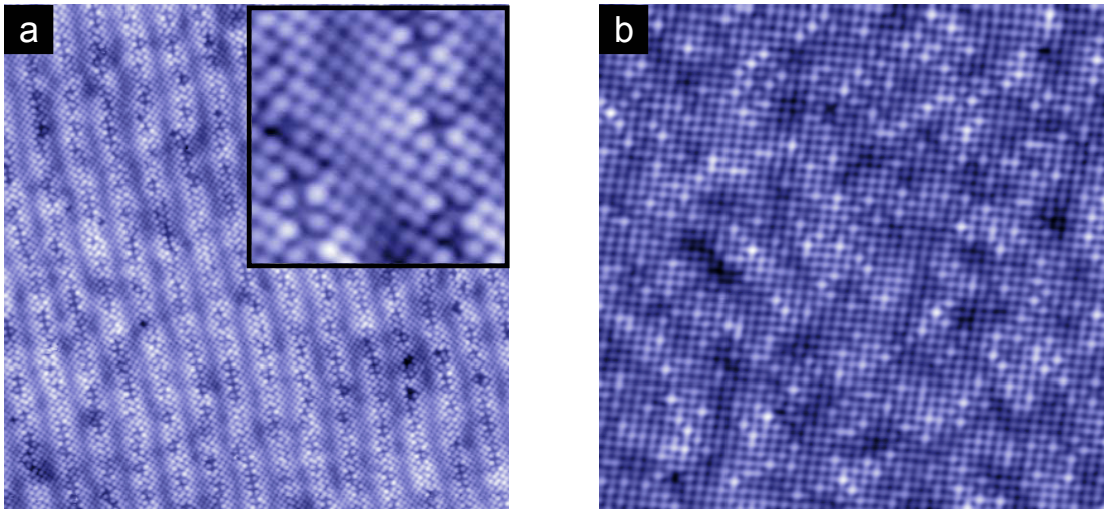

Figure 2.6: STM topographic images of the BSCCO superconductors. (a) 40×40 nm^2 area (400×400 pixels) of optimally doped Bi-2212 ($T_c = 91$ K). The bright spots, corresponding to Bi atoms, form a distorted square lattice. The inset is an enlarged view of a 5×5 nm^2 area (128×128 pixels). The average Bi-Bi distance is ~ 3.83 Å and the supermodulation has a period ~ 26 Å along the diagonal direction of the Bi lattice. (b) 20×20 nm^2 area (256×256 pixels) of an overdoped Pb-Bi2201 ($T_c = 18$ K). The bright atoms are doped Pb atoms on the Bi sites. Both images are recorded with $V_s = -100$ meV and $I_s = 100$ pA at $T = 6$ K.

values in the range of $[V_{\text{start}}, V_{\text{stop}}]$ with a constant step size ΔV, and record the current I while maintaining a constant d. To avoid a tip-sample collision during the measurement process, the time parameters are carefully set up and the sweep bias range is often chosen with $|V_{\text{start}}|, |V_{\text{stop}}| \leq |V_s|$. The dI/dV spectrum is then obtained by numerically differentiating $I(V)$. To reduce noise, a lock-in technique is used: a small AC modulation ($V_{\text{AC}} \ll V$) is summed with the bias voltage and the tunneling current is demodulated to yield dI/dV. The higher the frequency of V_{AC}, the quicker the measurement we can make. The upper frequency limit of V_{AC} is determined by

the bandwidth of the current amplifier. In our STM setup, the frequency of $V_{\rm AC}$ is optimally set to be 1.1 kHz. This frequency also avoids the 60 Hz harmonics and the frequency domain of mechanical noises. The energy resolution of the spectrum is decided by a combination of several parameters: the bias voltage separation ΔV, the amplitude of $V_{\rm AC}$, and the integration time at each bias voltage. The amplitude of $V_{\rm AC}$ is set to be comparable with ΔV; as both are small, a high energy resolution is resolved. Considering the thermal broadening at 4.2 K, $\Delta E \approx 4{\rm k_B T} = 1.4$ meV, we measure the dI/dV spectrum with a $1-3$ mV RMS modulation for $V_{\rm AC}$.

A reliable point spectrum is confirmed by reproducibility and d-independent shape. For high-T_c superconductors, the coherence length is short ($\xi \sim 10-20$ Å), and a slight contamination of the junction may destroy the superconducting features in the spectrum. A sample spectrum for optimally doped Bi-2212 ($T_c = 91$ K) is shown in Fig. 2.7. The horizontal axis is the bias voltage applied to the sample (in mV), which can be straightforwardly extended to the electron energy (in meV). Bi-2212 is a d-wave superconductor, and this spectrum has a V-shaped gap comparable to the ideal spectrum in Fig 2.4. The two coherence peaks define a gap centered on the Fermi energy ($V = 0$). Referring to the maximum gap size in the d-wave picture (see Chap. 1), this gap is equal to 39 meV. Although this value from the half distance between two coherence peaks is often larger than that from fitting the whole dI/dV spectrum, it is a good scale for comparing results from different groups. However, the reason for the asymmetric peak shapes and the energy-dependent conductance background are still open questions [70].

The signal-to-noise (S/N) ratio is another important property of the dI/dV spec-

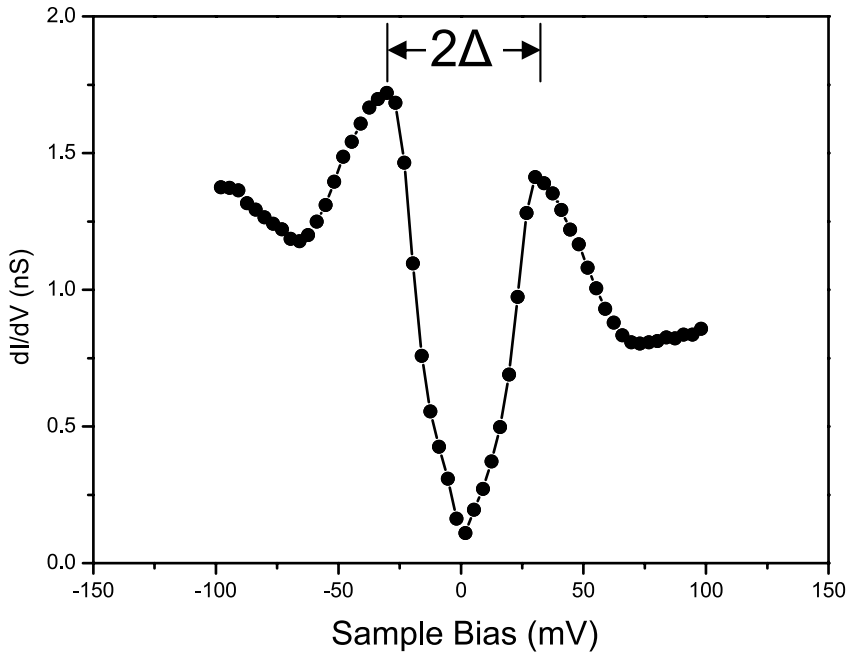

Figure 2.7: A typical dI/dV spectrum for optimally doped Bi-2212 ($T_c = 91$ K) in the range of $[-98\text{ mV}, 98\text{ mV}]$ with an energy resolution of 3.5 mV. The superconducting gap size Δ is 39 meV, determined by half the distance between the two coherence peaks. The spectrum is taken with $V_s = -100$ meV and $I_s = 100$ pA at $T = 6$ K. The lock-in amplifier is applied with a V_{AC} of 3.5 mV zero-to-peak amplitude and 1.1 kHz frequency.

trum. The S/N ratio can be improved by increasing the integration time at each bias voltage or averaging the spectra multiple times. To test the balance between a reasonable measurement time and a good S/N ratio, we compared a series of spectra, measured at the same spatial location, for one Pb-Bi2201 sample ($T_c = 15$ K), as shown in Fig. 2.8a. By recording a 'zero noise' reference spectrum (averaged 100 times), all non-averaged spectra with different integration times are divided by the reference spectrum. For each integration time, the standard deviation of the normalized spectrum is defined as its noise level. The result is displayed in Fig. 2.8b, from which we choose the integration time range of $10 - 20$ ms for our dI/dV spectra.

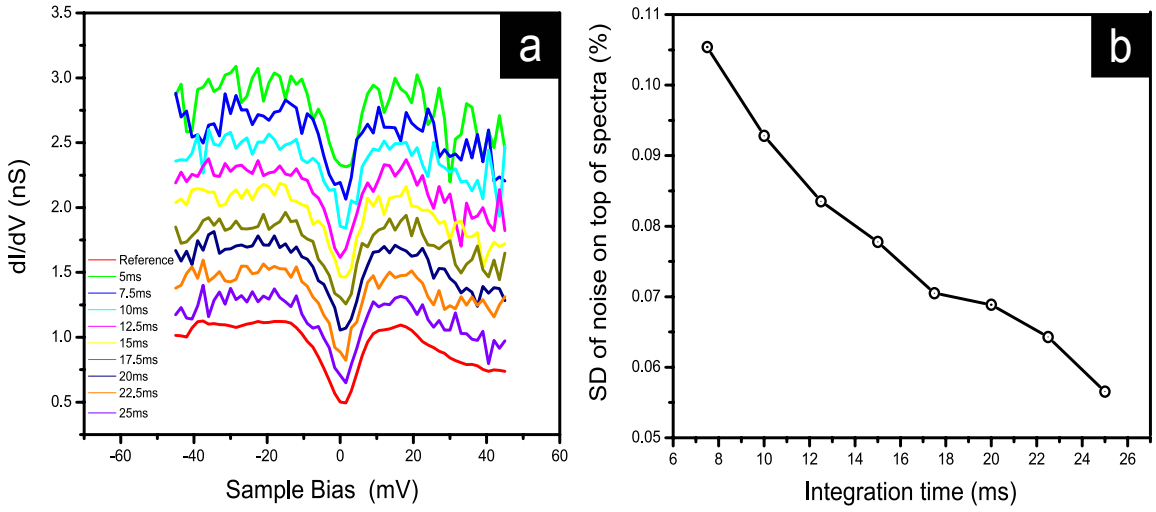

Figure 2.8: The analysis of the noise level as a function of the integration time for measured spectra. (a) A set of spectra measured at the same spatial location, for a Pb-Bi2201 sample ($T_c = 15$ K). Spectra are offset 0.2 nS for clarity, and the data are taken with $V_s = 100$ mV and $I_s = 100$ pA in the range of $[-40\text{ mV}, 40\text{ mV}]$. The energy resolution is 1.5 mV and V_{AC} has a 2 mV zero-to-peak amplitude and 1.1 kHz frequency. The integration time for each line is shown inside the figure. (b) The integration time dependence of the noise level, which is defined as the standard deviation (SD) value of the division between each spectrum and the reference spectrum.

STS DOS Map and the Fast Conductance Scanning Method

If the dI/dV spectra are recorded on a dense array of locations in real space, the spatial variation of the LDOS can be extracted. As a result, a STS DOS map is the conductance as a function of three variables: the spatial point (x, y) and the bias voltage V. During experiments, a matrix of (x, y) points is first defined. The tip is scanned across the matrix line by line, with the feedback on to maintain a constant tip-sample distance. At each spatial point, the tip is stopped, the feedback is turned off, and the dI/dV spectrum is then recorded. In practice, a topographic image can

be taken together with a STS DOS map.

The DOS map is a powerful technique for studying spatial dependence of electronic structure, including intrinsic inhomogeneity of the sample, and inhomogeneity induced by impurities or an external magnetic field. For example, the DOS map can be used to measure local gap variations and to take the vortex images under a magnetic field, as shown in later chapters of this dissertation. The gap size, Δ, is estimated by half the distance between coherence peaks. A 'gap map' can be obtained by plotting Δ for each spatial point. The average gap size $\overline{\Delta}$ is used to calculate the reduced gap $2\overline{\Delta}/k_{\mathrm{B}}T_c$, which roughly represents the coupling strength of a superconductor. Vortex imaging relies on the difference of the DOS between the normal state inside vortex cores and the superconducting state outside. Since coherence peaks are significantly suppressed inside vortex cores, the conductance at this energy can be mapped to a vortex image [81]. The conductance map at the vortex core state energy has also been used to extract the vortex image [82].

The measurement time of the DOS map depends linearly on the total number of data points in the three-dimensional space (x, y, V). The more pixels along x and y directions, the higher the spatial resolution; the smaller the voltage step size, the higher the energy resolution. For a standard 256×256 pixel DOS map with $\Delta V \sim 2$ mV in the ± 100 mV range, at least 24 hours are needed for the measurement. Sometimes, not all the information in the DOS map is necessary. For example, we may be only interested in one constant-energy slice of the DOS map. This conductance map can also be obtained by the so-called 'fast conductance scanning' method. Unlike the standard DOS mapping process, the feedback loop is always on. The bias voltage

is set at a specific value, e.g., the coherence peak position. To record the conductance, $V_{\rm AC}$ is summed with the bias with a frequency above the bandwidth of the feedback loop, and a lock-in amplifier is used to extract the conductance signal. When scanning the map area, we simultaneously record the conductance, resulting in the DOS map slice at the set bias voltage. The scan speed can be set to allow the time scale per pixel to be larger than a typical integration time in a spectral measurement. Notice that a conductance map at zero bias cannot be obtained by this fast scanning method.

To compare the standard DOS mapping and fast conductance scanning method, the data taken around an impurity in the optimally doped Bi-2212 sample ($T_c = 91$ K) are shown in Fig. 2.9 as an example. A non-magnetic impurity, such as Zn, substituting for a Cu atom in the CuO_2 plane of BSCCO suppresses superconductivity in the region nearby, and induces strong resonance peaks close to the Fermi energy in the dI/dV spectra. In the DOS map, a structured pattern is observed [83]. For our sample without intentionally doped Zn, we also observed a similar impurity, which can be possibly attributed to a Cu vacancy or an unknown non-magnetic impurity on a Cu site. In a 4-nm-square area around such an impurity, the DOS map (128×128 pixels) is recorded with $V_s = -100$ mV, $I_s = 100$ pA and the spectrum range $[-60\ {\rm mV}, 60\ {\rm mV}]$. The zero bias map slice is shown in Fig. 2.9a. By comparing it with the topographic image at the same area, we find the brightest spot at the impurity site and other observable spots at its nearby sites. Figure 2.9b demonstrates three dI/dV spectra from spatial points far away from the impurity (black), on the impurity site (red), and on the next nearest neighbor of the impurity site (blue), respectively. The red and blue lines have zero bias peaks, whereas this feature is absent in the black superconducting

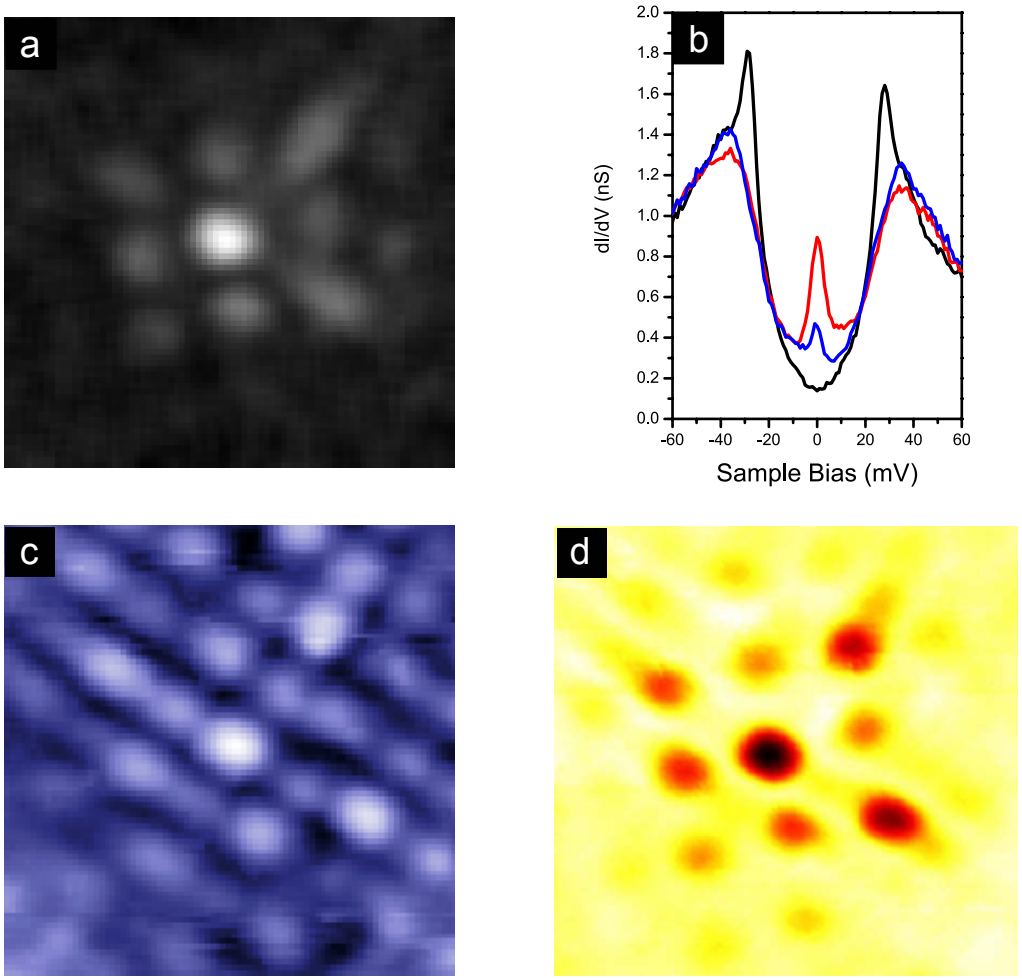

Figure 2.9: The comparison of the DOS mapping and the fast conductance scanning method using the data of an impurity in the Bi-2212 sample (T_c = 91 K). (a) A 4 nm×4 nm zero bias slice of the DOS map taken around one impurity with $V_s = -100$ mV and I_s = 100 pA. By comparing it with the topographic image, we find the correspondence between the bright spot and relative atomic sites around the impurity. (b) Three dI/dV spectra taken in the $[-60\text{ mV}, 60\text{ mV}]$ range. The black one is a superconducting spectrum at a spatial point far away from the impurity site. The red one is a spectrum at the impurity site, showing a strong resonance peak with energy close to the Fermi energy. The blue spectrum is taken at the next nearest site of the impurity, with a relative weaker resonance peak compared with the black spectrum. The contrast spectra lead to the DOS map with the complex structure. For the same spatial area, (c) and (d) are the topographic image and the simultaneous conductance map taken using the fast conductance scanning method with $V_s = -10$ mV and I_s = 100 pA. (d) has the same pattern as the structure in (a).

spectrum. Therefore, we can find the structured pattern around the impurity in the zero bias DOS map slice. For the same spatial area, we used the fast conductance scanning method to obtain the topographic image (Fig. 2.9)c and the simultaneous conductance map at $V_s = -10$ mV and $I_s = 100$ pA. This topographic image is consistent with that taken in the standard DOS mapping method (not shown here). At the same time, the -10 mV fast conductance map has the same structure as shown in Fig. 2.9a., with an even better S/N ratio. Since we choose a small bias voltage close to the resonance peak energy, the impurity structure is also reflected in the topographic image. From this comparison, we show that the fast conductance scanning is a reliable method to obtain the spatial dependence of an electronic feature with less time consumption if the appropriate bias voltage value is selected.

2.3 Summary

Electron tunneling through a classically forbidden energy barrier proves the validity of quantum mechanics in the microscopic world. Based on this quantum phenomenon, the scanning tunneling microscope was developed. STM can both test general quantum phenomena and probe the electronic properties of different materials. In this chapter, three operation modes of the STM/STS are discussed together with some example data from BSCCO superconductors. With high spatial and energy resolution, the STM has been well applied with great success to the investigation of high-T_c superconductors. For the cuprates, many important results have been addressed including pairing symmetry, gap inhomogeneity, dopant placement, and vortex pinning [70]. From a practical standpoint, STM is also ideally suited to

study new layered superconducting materials which may be initially available only in small single crystals. Compared to other spatially averaged techniques, the STM working in real space can uniquely explore the local electronic structures, e.g., the vortices and effects of impurities. In practice, the results of STM are always combined with complementary measurements, e.g., ARPES data to provide a complete picture. However, the delicate requirements for electronic tunneling and the high sub-Å precision make the STM construction complicated. In the next chapter, we will discuss the design and construction of our low temperature STM.

Chapter 3

Design and Construction of a Low Temperature STM

In the previous chapter, we discussed the working principle and operating modes of a STM. Now we discuss the real experimental setup. To study superconducting materials, we need a low temperature cryostat. To have a stable tunneling condition, we need a good vibration isolation. To have a clean tip and sample surface, we need an ultra high vacuum (UHV) environment, sample preparation, and tip treatment in vacuum. It is a tricky job to put all these concerns together [70, 84]. All of the experimental data in this thesis were taken on a home-built low-temperature STM in magnetic fields up to 9 T. In this chapter, I will present the experimental details of our STM system.

3.1 System Overview

Because the tip-sample distance is in the Angstrom range for a working STM, any vibrations from external environments will crash the tip into the sample, destroying the tunneling process. Therefore, vibration isolation is the most important criterion for a STM system. By calculating the vibration transfer function, we know that the design principle of a good STM is to make the natural resonant frequency (NRF) of the isolated system as low as possible and the NRF of the STM as high as possible [85]. For the former criterion, the commercial air spring is a good choice. The corresponding NRF is often below 10Hz with a loading within the weight capacity. The latter criterion needs a rigid STM head, inside which the relative motion is not affected by the external low-frequency vibrations. A system with multi-stage springs is always better but more complicated. The damping mechanism requires extra attention when the STM is installed by internal springs in the cryostat. In our system, we mount the STM directly on the cryostat without internal springs to avoid the nontrivial task of alignment between the sample and the sweet spot of the magnet. Externally, we have two stages of isolators as shown in the schematic diagram Fig. 3.1. The acoustic isolation room is floating on four big air springs. All mechanical pumps are placed in a separated pump room and the pumping lines are fixed in the heavy concrete wall with bellows between the pump and the floating room to isolate the vibrations from the pumps. A heavy triangular lead-filled wooden table is supported by three second-stage non-magnetic isolators[1]. A 75 L liquid helium (LHe) Dewar[2] containing

[1]Model No. 16NM-143-00, 2500 lb capacity, by Technical Manufacturing Corporation (TMC).

[2]AMI job #13069, by American Magnetics.

the cryostat is rigidly fixed to the bottom of the table. To avoid vibrations due to the boiling nitrogen, a super-insulating layer instead of a liquid nitrogen jacket is used as the shielding layer inside the vacuum jacket. A vertical geophone is also mounted on the 4 K flange to enable real-time vibration monitoring[3].

A two-axis superconducting magnet including a 9 T solenoid and 3 T split coil is installed at the bottom of the Dewar, with a 4.5" diameter (DIA) Dewar neck to minimize the LHe consumption. Detachable vapor-cooled current leads are available for the persistent magnet operation. To apply the split coil magnet field at different horizontal directions, a stepper-motor-controlled rotary platform is installed between the 300 K flange of the fridge and the Dewar[4]. No magnet materials were used in the construction of the cryostat and STM, and all electronic connectors were tested to ensure that magnetic plating is not deleterious to the experiment. A Hall sensor[5] is glued close to the sample position on the STM to roughly measure the applied magnetic field.

The home-built cryostat is designed as a continuous mode ^{3}He refrigerator with expected base temperature around 400 mK. The lowest temperature achieved to date is 1.4 K (STM stage), obtained by pumping on the ^{4}He pot with a 32.5 CFM (cubic feet per minute) rotary pump[6]. Because our initial interests are high-T_c superconductors whose critical temperatures are much higher than 4.2 K, the results shown in this thesis are all obtained at temperatures around 6 K by thermally linking different

[3]Model 2GS-1, by Geospace Technologies.

[4]Model DPRFM800, by Mcallister Technical Services.

[5]HGT-2100-10, by Lakeshore Cryogenics.

[6]Model D40B, by Oerlikon Leybold Vacuum.

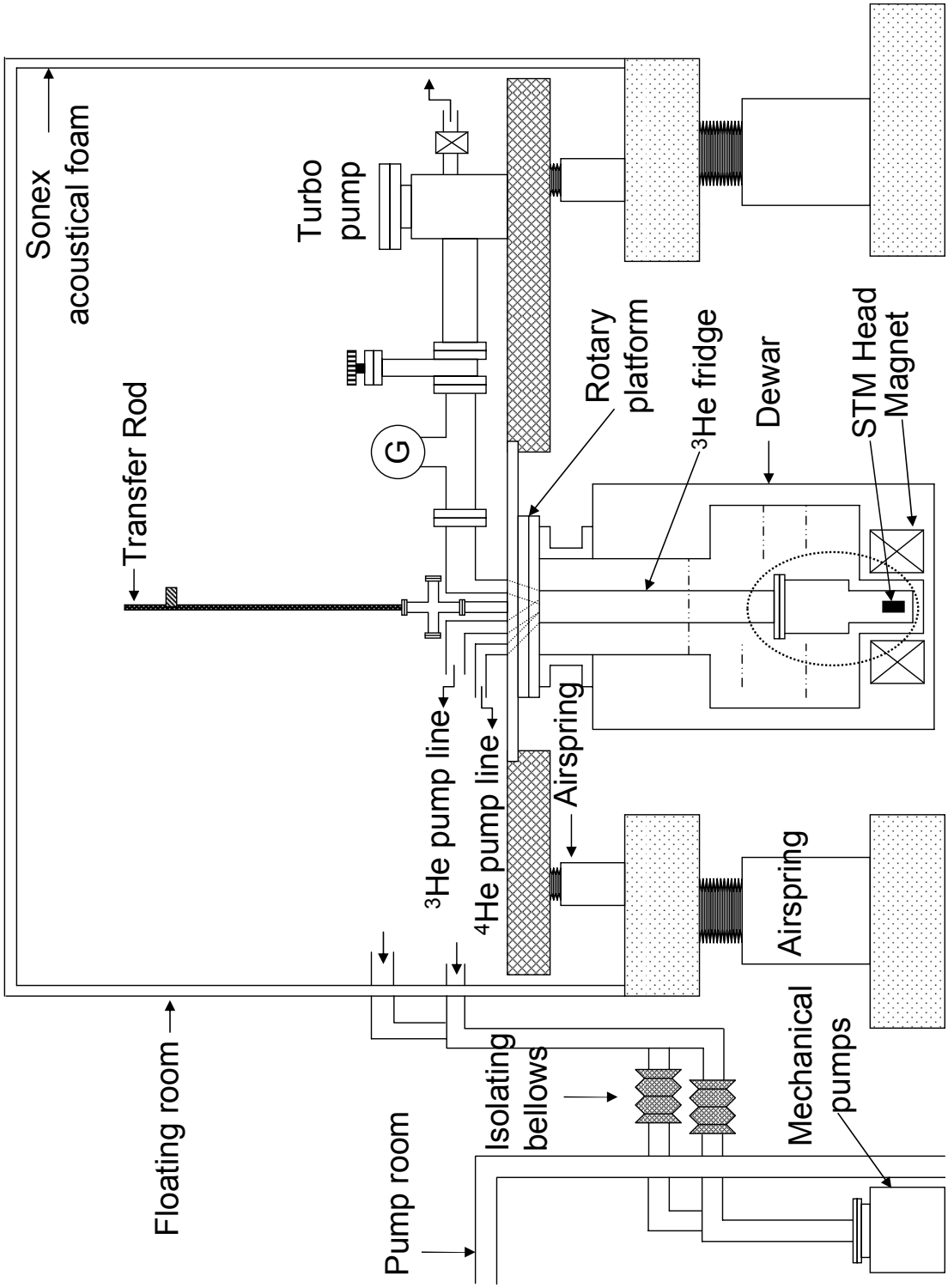

Figure 3.1: Schematic diagram of home-built low temperature STM system. The part circled by the dashed line refers to the fridge and STM which is shown in Fig. 3.2 in detail.

fridge stages with copper braids. Since the thermal link between the STM body and the 4 K flange is not strong, we can use a heater wire[7] wound around the base plate of the STM and a Lakeshore feedback control[8] to stabilize the temperature in a range between 6 K and 20 K. A calibrated Cernox sensor[9] is thermally anchored close to the sample on the STM to measure the sample temperature. Two ruthenium oxide resistance-based temperature sensors[10] are thermally anchored at the ^{4}He and ^{3}He stages to monitor their respective temperatures. As part of the ultra low temperature design of the cryostat, all electronic connections from room temperature are carefully heat-sunk at each stage, and wire materials with low thermal conductivity are chosen. Baffles are placed on the neck of the cryostat and inside the 1.5" DIA pump tubes to minimize thermal radiations from room temperature. With all the above considerations in minimizing the heat input, we typically refill the LHe bath approximately weekly.

A 60 l/s turbo pump[11] is used to pump the main vacuum space, which is connected to the top pumping line by a center 0.5" DIA and a side 1.5" DIA stainless steel (SS) 304 tube. The small center tube ends on top of the table with a mini UHV gate valve and the other vacuum tube ends with a DN 40 gate valve. The main vacuum pressure is around 10^{-6} mbar after pumping overnight at room temperatures. The working pressure measured on top of the table is 10^{-8} mbar for a cold system and

[7] 0.0056" DIA Mangrnin with HML insulation, $R \sim 150\ \Omega$, by California Fine Wine Company.

[8] Model 340, by Lakeshore Cryogenics.

[9] Model CX-1010-SD, by Lakeshore Cryogenics.

[10] Model RX-102A-AA, by Lakeshore Cryogenics.

[11] Model TMU 071, backed by XtraDry 150-2 Dry Piston Pump, by Pfeiffer Vacuum.

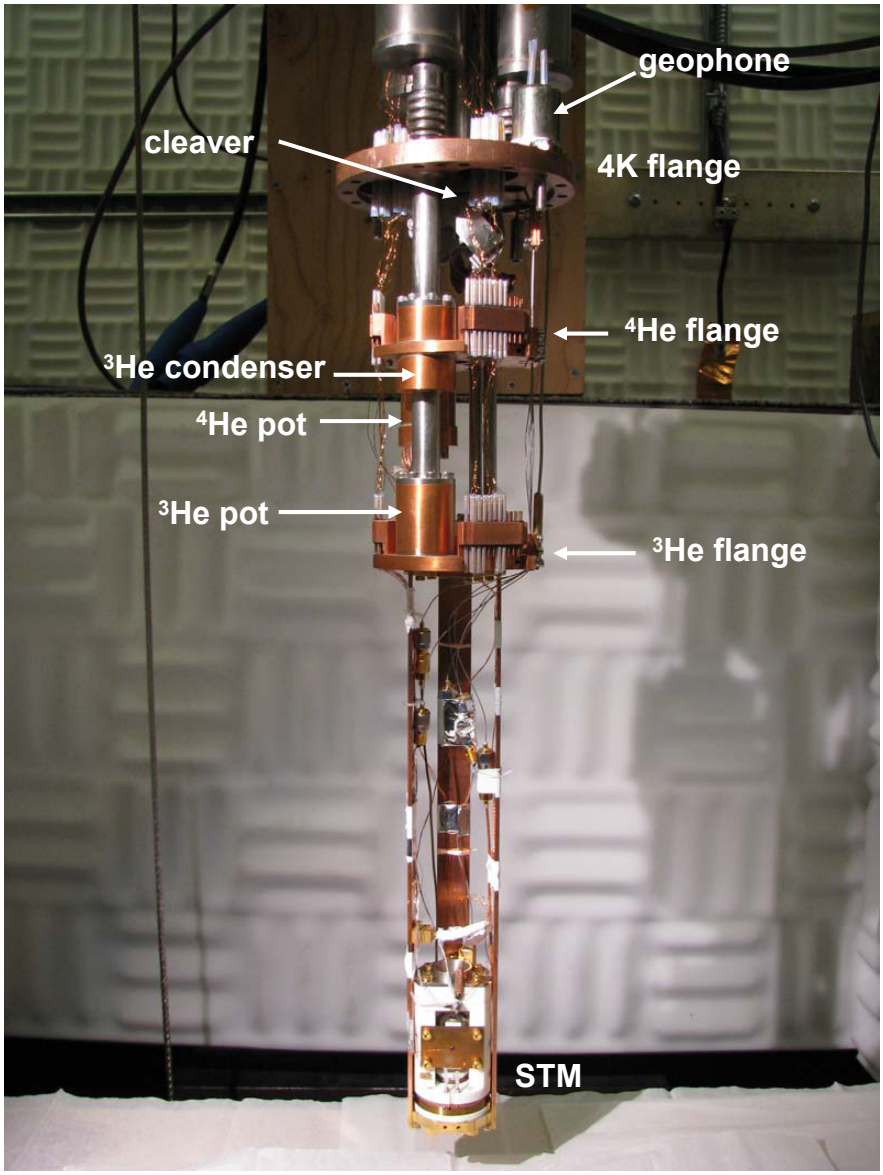

Figure 3.2: Photo of fridge and STM

the pressure around the STM head should be lower because of the cryogenic vacuum. To keep the vacuum conditions, UHV compatible metals, plastics, wires, connectors,

glues, and solders are carefully selected in the system design.

To reduce the experimental turn-around time, a top loading system is designed to transfer a sample into the cold STM. A small home-built differentially pumped load-lock space is installed on top of the mini gate valve, through which a long 0.25" DIA SS tube transfers the sample holder down to the STM head. When passing through the 4 K flange of the cryostat, the sample holder can be clamped to a copper cold plate to decrease the temperature of the sample. The sample is cleaved in a direction-controlled and spring-activated mechanical cleaver below the cold plate to expose an atomically flat and clean sample surface. The low temperature cleaving avoids contamination of the surface and possible crystal cracks from thermal cycles. The sample is locked in the STM head and the transfer tube is retracted. Afterwards, both gate valves are closed and the turbo pump is turned off.

3.2 STM Head

We designed our STM head to be rigid and compact. The small size of the STM head allows it to fit in the limited space within a superconducting magnet bore. The rigidity ensures the high NRF of the STM body, and relative vibrational movement between tip and sample is suppressed. The essential part of the STM head is the tip and the sample. We cut 80/20 Pt/Ir wires[12] to produce STM tips. Before the experiment, the STM is tested in air at room temperatures, and the tip is further cleaned at low temperatures by performing field emission on a polycrystalline gold sample. When transferring the sample, the sample holder is pressed against a BeCu

[12] 0.01" DIA, from ESPI Products Inc.

spring (flexible at low temperatures) in the top receptacle of the STM, with the sample surface upside-down. Good mechanical contact between the BeCu plate and the sample holder ensures the stable configuration of the sample. Electrical and thermal contact between the BeCu plate and the sample holder is also good. A sample bias voltage is applied to the BeCu plate, and the Cernox sensor is glued onto the BeCu plate to measure the sample temperature.

A small BeCu tube is used as a tip holder with the STM tip fit snugly inside (see Fig. 3.3). A thin copper wire is glued on the side of the BeCu tube and connects to the center of the tunneling-current-carrying BNC cable. The tip holder is glued within a ceramic tube, which is isolated from the bottom scan tube by a macor receptacle. A copper ground plate is glued on the surface of the macor receptacle attached with another thin copper wire which connects to the insulation of the current BNC cable. The ground plate improves the shielding of the tunneling current signal. The scanning function of the tip is realized by a piezo scan tube[13]. The calibrated scanning sensitivity of our piezo tube at 6 K is 257 pm/V in the z direction and 2.4 nm/V in the x/y directions. Different high voltage (HV) gains of the HV amplifier of the STM controller can output a piezo actuating voltage in the range of $\pm$450 V or $\pm$150 V. The corresponding scan range can be calculated. Our commercial scan tube was polarized at 1200 V, and it is recommended to work at a voltage smaller than $\pm$300V at room temperatures. The z range of the piezo tube decreases at low temperatures due to an approximate 1/3 reduction of the piezo strain coefficient d_{31} at 4.2K. Therefore, we actuate the piezo tube with $\pm$150 V range at room temperatures

[13]EBL # 4 piezo ceramic tube 0.125" OD $\times$ 0.020" wall $\times$ 0.250" length, by EBL products.

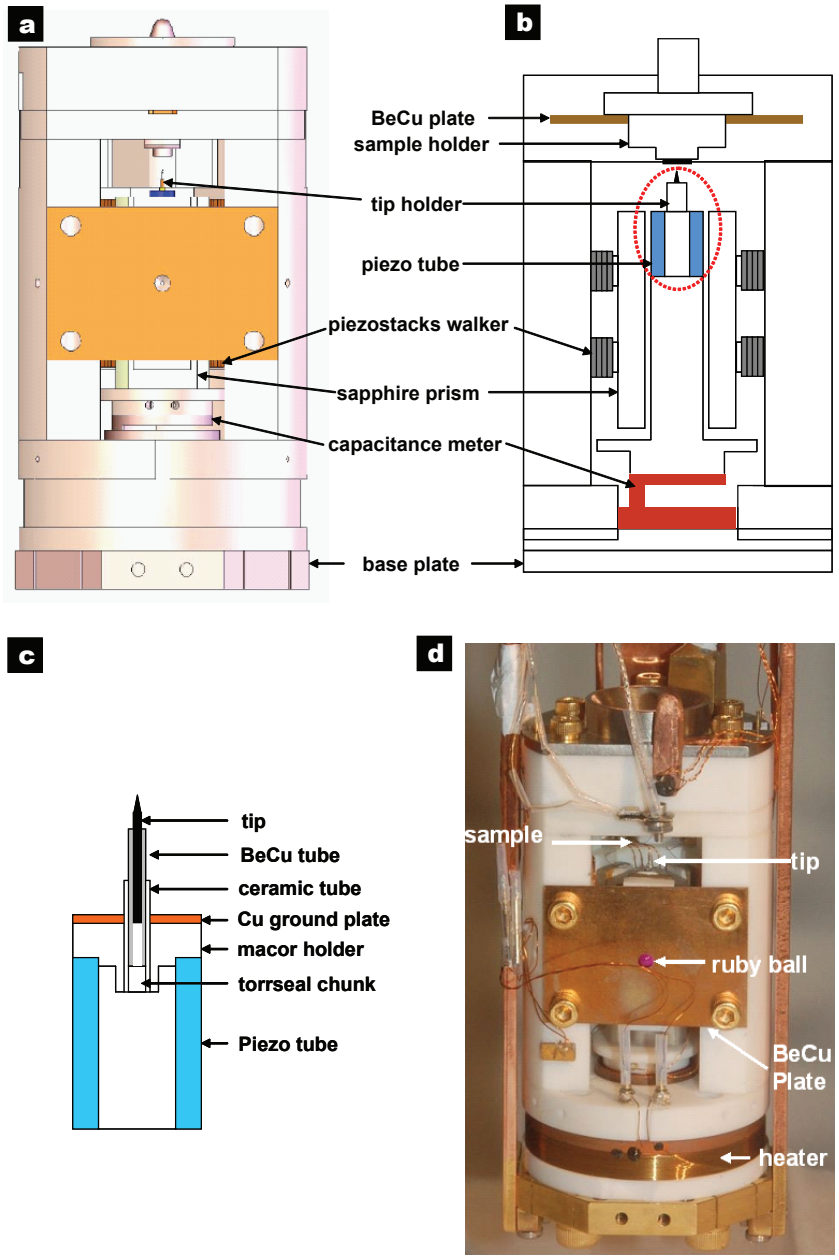

Figure 3.3: Details of our home-built STM. (a) Front view of SolidWorks schematic of the STM. (b) Schematic diagram. The part circled by the dashed line refers to the tip assembly which is shown in (c) in detail. (d) Photo of the STM.

and extend to ±450 V range at low temperatures.

Before each tunneling measurement, the tip needs to be brought from a far away

position to the tunneling distance range. This process is called a 'coarse approach', which is realized by a step walker made of six shear piezo stacks in our system [84]. The piezo tube scanner and the step walker are integrated together to the center sapphire prism[14] (see Fig. 3.3). The scanner is fixed to a macor holder, which goes through the center hole of the sapphire, and is screwed to the sapphire at the bottom. The whole sapphire piece is clamped by six sets of piezo stacks. Four of the piezo stacks are glued to the main body, and have alumina pads contacting with the sapphire prism by friction. In the front of the STM, two remaining piezo stacks are glued to a macor plate, which is compressed to the prism by a ruby ball held on with a BeCu spring plate. With such a configuration, the working principle of the walker system is as follows. Six voltage steps are applied to the piezo stacks one by one. Each set of piezo stacks will deform, but the sapphire prism will be stationary because the other stacks are holding it in place. In the end, the voltages applied to all the piezo stacks are ramped simultaneously, slowly back to zero, giving rise to one step movement of the sapphire prism and the tip. Compared with other coarse approach mechanisms, such as the inch-worm type, the besocke-style and the slip-stick type [85], our shear-piezo-stacks step walker clamps the sapphire at all times throughout the movement, which is the essential design element for making the STM head rigid. The walker also produces reliable and reproducible steps. The step size is finely tuned by the tightness of the screws which fix the front BeCu plate. A typical calibrated step size is around 70 nm with 100 V driving voltage at room temperatures. The step size has a small variation between up/down directions due to gravity. Normally, we

[14]from Markethch International Inc.

walk continuously to a safe starting point, and start the woodpecker coarse approach. Before each woodpecker step, whether the tip is close to the tunneling distance is checked by turning the z piezo feedback on. With the applied z voltage, the piezo tube is extended to attempt detecting any tunneling current. If no tunneling current is detected, the tube is fully withdrawn and the walker moves the tip one step closer to the surface. Otherwise, the walker stops and the tip is fully withdrawn to wait for the scanning experiment. The z voltage polarity and the extension range should be compatible with the step size of the walker for a safe coarse approach process.

In Fig. 3.3, there are two Cu concentric cylinders fixed to both the STM base plate and the bottom of the sapphire piece. With movements of the sapphire piece in the coarse approach, the relative capacitance between the two Cu plates changes. By measuring the capacitance using a capacitance meter, we monitor the relative tip location.

3.3 Electronics

To avoid disturbing the STM, we put most of our control electronics outside of the floating room. All the cables are carefully fixed to decouple their mechanical movements from the experimental table. The schematic architecture of all electronics is shown in Fig. 3.4. The most important control unit is the Nanonis STM control system[15], which can be used to scan STM images, make STS measurements with an internal lock-in amplifier, and couple these two functions together to produce DOS maps. The real time engine is a Pentium processor based rack computer to

[15]SPM-Controller, Nanonis GmbH, CH-8005 Zurich.

run all the deterministic control loops and the data acquisition. Inside the real time engine, a National Instruments FPGA card provides sixteen 16-bit DAC and ADC channels with a range of ±10 V. The signal conditioning connector box (SCCB) accepts analog input signals, such as the tunneling current voltage, and provides analog output signals, such as the bias voltage and the xyz scan voltages. The HV amplifier amplifies the xyz scan voltages to drive the scan piezo. The SCCB also outputs the digital signals. We use one digital signal as a TTL signal to trigger our home-built walker controller. By making good use of the extra ADC/DAC/digital channels, custom functions are integrated together with the main control system. With Labview software and a flexible programming interface, custom programs are produced, e.g. writing extra signals (temperature, magnetic field, pressure and so on) to the header of the image files.

To eliminate external electronic noise, RG 58 shielded BNC cables are used for all the channels from the STM controller to the top of the fridge. A bias adder couples the DC bias voltage with an AC lock-in output from the STM controller. The bias voltage goes down the fridge through a semi-rigid coax[16] to the BeCu plate. Another semi-rigid coax cable is used to connect the tunneling current signal from the tip to the top of the fridge. A current amplifier converts the current to a voltage which goes along the RG58 cable back to the STM controller for the measurement. All high voltage signals from the STM controller and the walker controller to drive the piezo tube and piezo stacks are filtered by π filters before going down to the STM head, through twisted manganin wires.

[16]CC-SR-10, by Lakeshore Cryogenics.

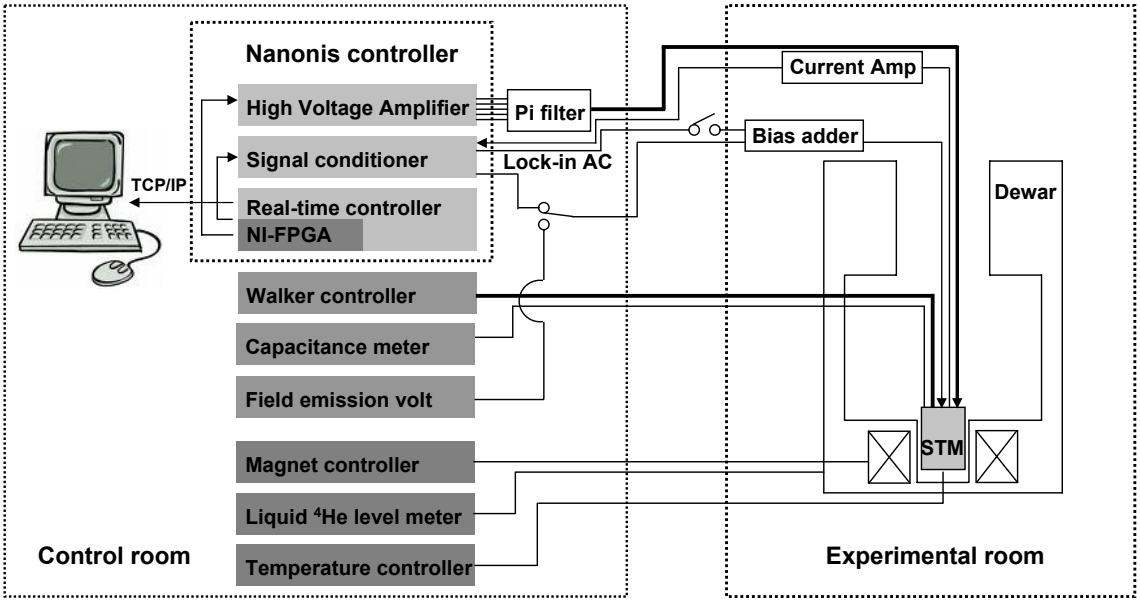

Figure 3.4: Schematic diagram of the electronics used in the experiment.

A current amplifier with a fixed gain (10^9 V/A)[17] converts the small tunneling current (within the pA range) to a voltage signal for measurement. The current amplifier is directly mounted to the vacuum coaxial feedthrough on top of the fridge to have the smallest coax capacitance between the amplifier and the STM head. The short coax cable has less induced electronic noise from the microphone effect. The current amplifier obtains a ± 15 V power supply from the STM controller to avoid ground loops. A different variable gain current amplifier[18] is necessary when performing field emission since a μA range current is needed.

There are a few other electronics in the control room. They are the field emission

[17]Model LCA-4k-1G, by FEMTO Messtechnik GmbH.

[18]DL1212, by D.L. Instruments

voltage source (with a maximum 500 V), home-built walker controller, home-built capacitance meter, temperature controller, magnet controller, and LHe level meter. The functions of these electronics are either low temperature and magnetic controls, or explained in the appendixes.

Chapter 4

STM Studies in Iron Pnictide Superconductors

Tremendous excitement has followed the recent discovery of superconductivity up to $T_c = 56$ K in iron-arsenic based materials (pnictides). This discovery breaks the monopoly on high-T_c superconductivity held by copper-oxides (cuprates) for over two decades and renews hope that high-T_c superconductivity may finally be theoretically understood and widely applied.

STM and STS have been key tools in investigating and understanding both conventional and unconventional superconductivity, and are also applied to the pnictides. In this chapter, I present our experimental results from STM/STS on the pnictides and discuss the contribution towards an understanding of superconductivity in this new class of materials[86].

4.1 Material Properties of Pnictides

In the overview of superconductivity (see Chap. 1), a short history of the discovery of the Fe-based superconductors (FeSC) was presented. Since most of the FeSC are FeAs-based, the iron pnictides or simply pnictides are also used as common names. Like the cuprates, the pnictides have a layered structure. Consequently, high-quality single crystals can be mechanically cleaved to expose atomically flat and clean surfaces suitable for characterization by surface sensitive probes such as scanning tunneling microscopy (STM) and spectroscopy (STS). This cleaving procedure, however, cannot be applied to samples less than $\sim$ 100 μm in size. To date, the largest single crystals, reaching $3 \times 5 \times 0.2\,\mathrm{mm}^3$ in size, are members of the non-oxide 122 family, grown with Sn or FeAs flux [43, 87]. In contrast, only tiny single crystals of the 1111 family exist, not larger than $200 \times 100 \times 30\,\mu\mathrm{m}^3$ [88, 89]. Therefore, most of the STM/STS studies have been carried out on Ba/Sr-122 samples, with only a few STS measurements on 1111 poly-crystals[90].

Low temperature STM and STS have been important tools for the investigation of cuprates, due to the capability of probing the electronic density of states (DOS) with atomic resolution [70]. The local DOS contains crucial information of the superconducting electronic structure: spatial inhomogeneity [91, 92, 93, 94], behavior in proximity to impurities [83, 95, 96], doping dependence [93], and magnetic field dependence [97, 98, 82, 99, 100]. This success motivates the application of STM and STS to the pnictides to gain insight to the underlying mechanism of superconductivity in these compounds.

The 122 family of pnictides becomes superconducting upon the introduction of

either hole or electron dopants. For example, $BaFe_2As_2$ becomes a hole-doped superconductor upon replacement of Ba^{2+} by K^+ [42], or an electron-doped superconductor upon replacement of Fe^{2+} by Co^{3+} or Ni^{4+} [101, 102]. The initial motivation to dope Fe^{2+} by Co^{3+} was to search for electron-doped 122 samples, based on considerations of valence and stoichiometry. The successful synthesis of a superconducting $BaFe_{2-x}Co_xAs_2$ proves that the disorder in the superconducting plane is highly tolerated. This emergence of superconductivity through chemical substitution directly into the superconducting layer is in stark contrast with the cuprates, where the substitution of impurity elements for even a small percentage of the Cu atoms can destroy superconductivity [103]. Furthermore, cobalt is a more chemical-friendly dopant compared to potassium. It is convenient to control the doping values of Co; however, the potassium or general alkali metals are volatile and escape easily in the sample-growing process.

We choose to study optimally doped single crystal $BaFe_{1.8}Co_{0.2}As_2$ in our home-built cryogenic STM. Since the Co dopants are incorporated into the strongly bound FeAs layer, the topmost layer is more similar to the bulk and remains more stable under tunneling. Our samples are grown with FeAs flux to avoid contamination with other elements [87]. The resistivity is measured on the *ab* plane of a cleaved single crystal by the standard four-probe method, and shows a sharp superconducting transition at $T_c = 25.3$ K with width $\Delta T = 0.5$ K (see Fig. 4.1).

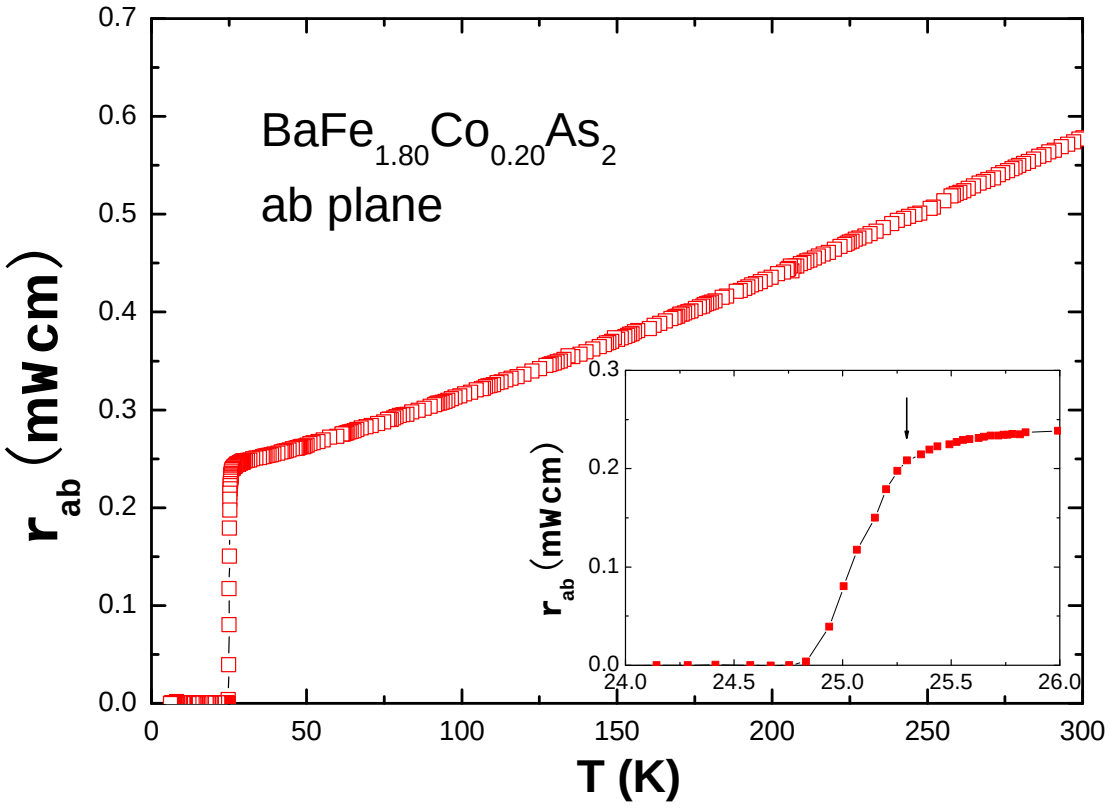

Figure 4.1: The temperature dependence of the resistivity for single crystal $BaFe_{1.8}Co_{0.2}As_2$ (data from X. H. Chen's group). Standard four-probe method is applied on the *ab* plane of the cleaved sample. The inset shows the superconducting transition in detail. The starting point of the transition happens at 25.3 K, denoted by the black arrow, and the transition width is sharp with $\Delta T = 0.5$ K.

4.2 Crystal Structure and Surface Characterization

Pnictides are layered compounds which can be mechanically cleaved to expose the *ab*-plane (see Fig. 4.2a). Consequently, all of our STM/STS studies on cleaved single crystal pnictides so far are taken along the (001) direction, but the exact composi-

tion of the exposed surface is still an open question. In the cuprate superconductor $Bi_2Sr_2CaCu_2O_{8+\delta}$ (Bi-2212), most widely studied by STM, cleaving usually occurs between mirror BiO planes coupled by weak van der Waals forces [70]. This process removes a complete BiO layer and leaves behind a charge-neutral surface. Among 1111 and 122 families of pnictide superconductors, no such neutral, charge-balanced cleavage planes exist. Pnictide cleaving recalls the cuprate superconductor $YBa_2Cu_3O_{7-\delta}$ (Y123), which cleaves between BaO and CuO chain layers without neutral exposed planes [104].

For 1111 pnictides such as LaFeAsO, the inter-layer coupling between $(LaO)^+$ and $(FeAs)^-$ layers is mostly ionic, but weaker than the ionic bonding within LaO layers and the covalent bonding within FeAs layers [106, 107]. Thus we expect LaFeAsO crystals to cleave between LaO and FeAs layers, exposing a charged surface plane. This expectation is substantiated by angle resolved photoemission spectroscopy (ARPES) measurements of the enclosed Fermi surface volume on the cleaved surface of isostructural LaFePO [59].

When studying materials that have a polar cleaved surface, the electronic structure detected using surface-sensitive techniques is likely to be different from that of the bulk, affecting measurements of the carrier density, Fermi level, and effective doping [108]. In addition, atomic reconstruction, adsorption of charged contaminants, and electronic reconstruction might occur at the surface in order to compensate for the charge imbalance [109].

In 122 pnictides, A^{2+} (A=Ba, Sr, Ca, Eu) sheets are sandwiched between $(FeAs)^-$ layers. In this case, both inter-plane bonding and A^{2+} in-plane bonding are relatively

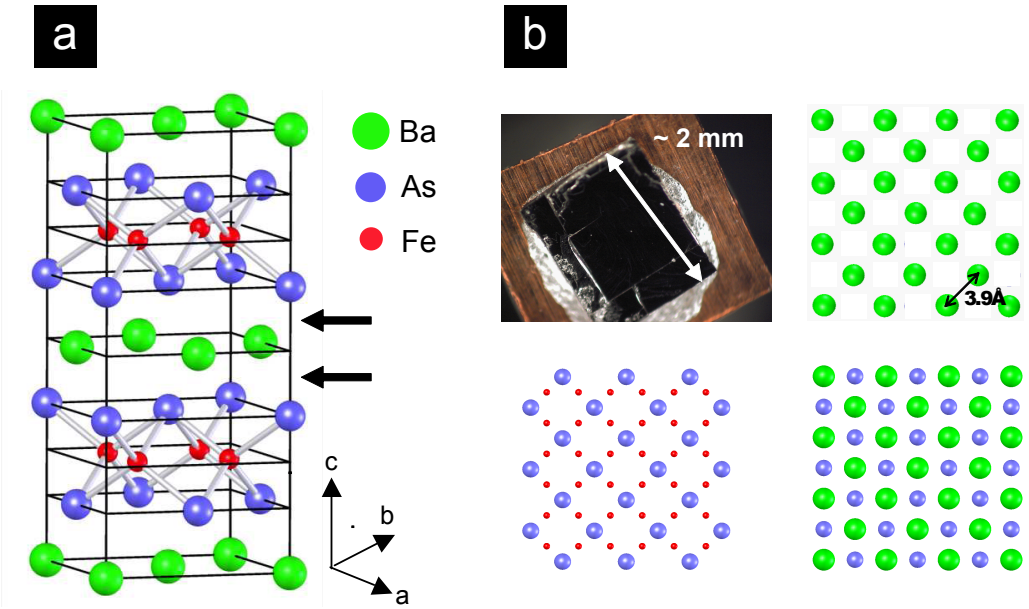

Figure 4.2: Crystal structure of $BaFe_2As_2$. (a) Tetragonal $BaFe_2As_2$ 122 type with room temperature lattice constants $a = b = 3.96$ Å and $c = 12.39$ Å [105]. Two black arrows indicate possible cleaving planes, exposing either Ba or As planes. (b) The cleaving situation of the Ba-122 sample. Top left: optical microscope image of the cleaved Ba-122, showing a smooth and shining surface. Top right: the Ba lattice if the whole Ba plane is the exposed cleaving surface. Bottom left: top-down view of the As and Fe lattices. Bottom right: top-down view of the Ba and As lattices.

weaker compared to the covalent FeAs bonding. Therefore, crystals are likely to cleave either between A^{2+} and $(FeAs)^-$ planes, leaving behind a charged surface, or within the A^{2+} plane, leaving about half of the A^{2+} atoms on each of the exposed, charge neutral surfaces. A charge neutral plane is substantiated by the Fermi surface volume measurements from ARPES studies of $BaFe_2As_2$ [110, 111]. But there is no consensus yet about how the half of the A^{2+} atoms distribute on the cleaved surface.

Figure 4.3a shows a topographic image of the surface of $BaFe_{1.8}Co_{0.2}As_2$ ($T_c = 25.3$

K), cleaved *in situ* at $\sim$ 25 K and recorded at 6.15 K in zero magnetic field. The tunneling condition is $V_s = -100$ mV and $I_s = 100$ pA. A 2×1 stripe feature with a period ~ 8 Å is present in this image. Surprisingly, when we push the tip further to the surface with a smaller junction resistance at $V_s = -20$ mV and $I_s = 40$ pA, the topographic image shows the atomic structure in detail (see Fig. 4.3b). In the inset of Fig. 4.3b, we observe single atoms, and a complex unit-cell-doubling stripelike structure in which alternate rows display contrasting brightness and clarity, as well as atomic shifts by approximately half a lattice constant along the row direction. The 2×1 stripes were observed in a previous STM study on $Sr_{1-x}K_xFeAs$ [112]. The stripelike feature is oriented at 45° to the one-dimensional spin order observed in the parent compound of these materials [66] and is therefore not likely related to this bulk order. In addition to the stripelike feature, there is another sparse, perpendicular, one-dimensional feature in the topographic image, which is a possible dislocation to relieve surface strain. Neither features show any effects on the local superconducting gap. More information is extracted from the Fourier transformation of Fig. 4.3b. The interatomic spacing, represented by peaks A and A^* in Fig. 4.3c, is consistent with x-ray diffraction measurements in either the Ba or As layer, $a = 3.96$ Å. Peaks B and C in Fig. 4.3c are related to the alternating row intensity, which may be attributed to either height or density of states variations. By filtering out the central high-intensity area of the Fourier transformation image and executing a reverse Fourier transformation as in Fig. 4.3e, we extract a real-space image (e), suggesting that alternate rows of Ba have been removed on the top surface. Therefore, we explained this complex surface structure by the removal of every second row of Ba atoms by

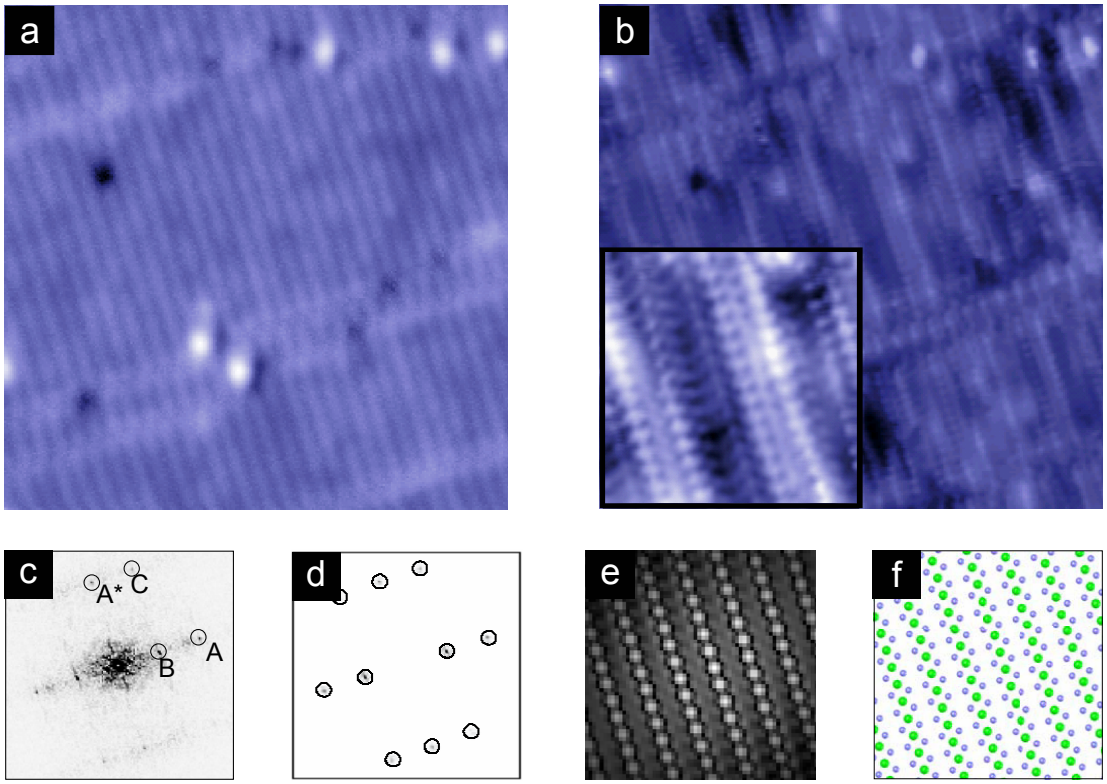

Figure 4.3: Topographic images of the single crystalline Ba-122 compound, revealing stripe-like surface structure. (a) 20×20 nm^2 constant-current topography of $BaFe_{1.8}Co_{0.2}As_2$, cold-cleaved and recorded with $V_s = -100$ mV and $I_s = 100$ pA at 6.15 K [86]. Only a stripe feature with a period ~ 8 Å is present in this image. (b) 20×20 nm^2 constant-current topography at the same area as in (a). The image is recorded with $V_s = -20$ mV and $I_s = 40$ pA at 6.15 K. The inset shows a 5×5 nm^2 zoom with atomic resolution. (c) Fourier transformation of the topographic image in (b). The main features are a central high-intensity area representing long length scale inhomogeneity, and 4 distinct points (with their symmetric equivalents): A and $A^\star$ result from atomic spacing between and along the stripes, respectively; B results from the alternating stripe intensity; C results from the shift of atoms along alternate rows. (d) The same Fourier transformation as (c) after filtering out the central high-intensity area. (e) Reverse Fourier transformation of (d), demonstrating more clearly the atomic locations of the original topography without the longer wavelength disorder. This image clearly suggests that alternate rows of Ba have been removed, exposing the shifted rows of As atoms beneath. (f) Schematic of the surface of the half cleaving scenario. Large green dots correspond to Ba atoms, small purple ones to As atoms. (e) and (f) are the same scale as the inset in (b).

cleaving: the less distinct, shifted rows (see inset of Fig. 4.3b) would consist of two rows of underlying As atoms between each row of Ba atoms (see Fig. 4.3f). The cleaving scenario, with half of the Ba atoms cleaved away, is at least consistent with the topographic image in (b).

Details of the topography vary from cleave to cleave, but the 2×1 stripe feature is found to be a predominate surface feature for most clean samples. In a larger scale ($\sim \mu$m), there are often isolated and clustered atoms, which are attributed to Ba atoms. Both the disordered Ba atoms and the half-cleaving Ba surface may be related to unstable bonding within the ionic Ba plane. In addition to the topographic configuration in Fig. 4.3, two other prototype topographic images are shown in Fig. 4.4. The 2×1 dimer stripes in Fig. 4.4a are more likely from a surface reconstruction in the As plane. The $\sqrt{2} \times \sqrt{2}$ surface (Fig. 4.4b) can be related to either a surface reconstruction or the removal of every second Ba row diagonal to the *ab* lattice vectors.

The investigation of the topographic images in Ba-122 samples indicates that surfaces of the pnictide compounds are not as stable as, for example, the surface of Bi2212, where atomic resolution has been reported even at room temperature [78, 80]. This limit has been the biggest roadblock to further STM/STS studies in the pnictides.

4.3 Scanning Tunneling Spectroscopy

The identification of the superconducting order parameter, including the gap size and symmetry, is a necessary step to determining the microscopic superconducting

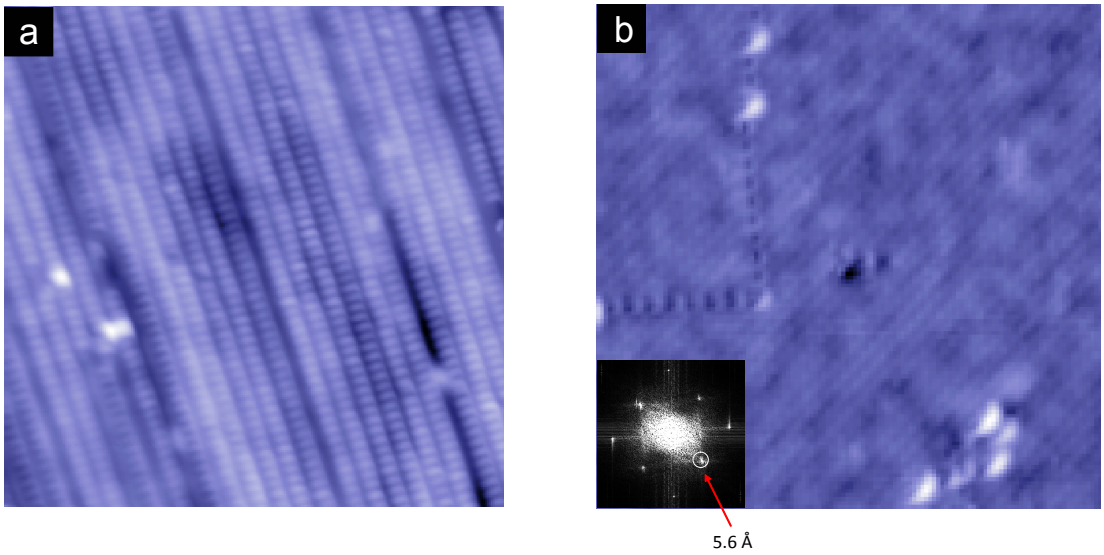

Figure 4.4: Topographic images of single crystalline Ba-122 compound, revealing stripe-like surface structure. (a) 20×20 nm^2 constant-current topography of $BaFe_{1.8}Co_{0.2}As_2$, cold-cleaved and recorded with $V_s = 100$ mV and $I_s = 500$ pA at ~ 6 K. A 2×1 dimer stripe feature is present. (b) 20×20 nm^2 constant-current topography recorded with $V_s = -100$ mV and $I_s = 300$ pA at ~ 6 K. The inset shows its Fourier transformation and the atomic spacing 5.6 Å indicates a $\sqrt{2} \times \sqrt{2}$ surface.

mechanism. The possibility of multiple gaps, potentially with different symmetries arising from the multi-band electronic structure, has motivated intense efforts in studying the electronic structure of pnictides with several complementary spectroscopic techniques, including STS.

The power of STM/STS is to measure the electronic structure with sub-atomic spatial resolution. The reliability of this measurement depends on the condition of the tunnel junction. Tip preparation methods have been honed by years of STM studies, so the condition of the tunnel junction depends mainly on the sample quality and material-specific surface stability. Differential tunneling conductance spectra, dI/dV,

measured on the optimally doped pnictides are presented in this section.

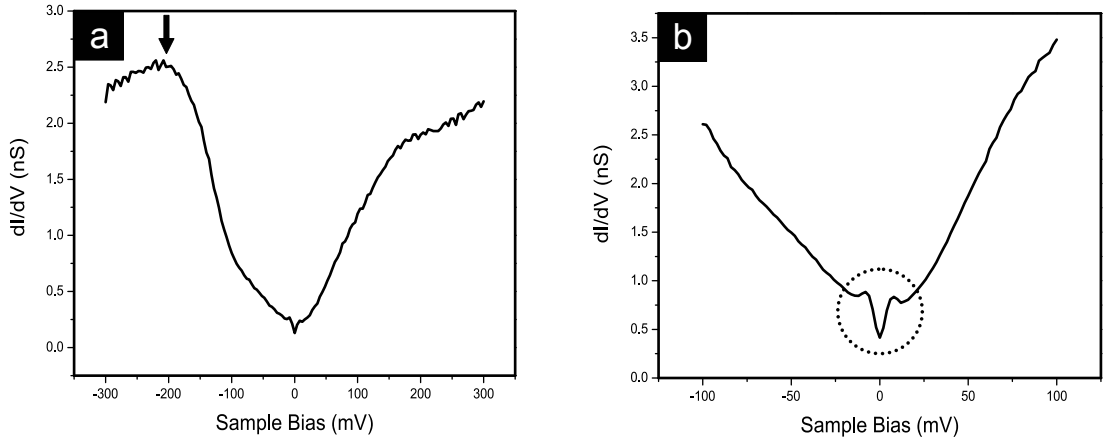

Figure 4.5: Single point spectra recorded on the same spatial point with different bias voltage range. (a) Spectrum recorded in the bias range $[-300\text{ mV}, 300\text{ mV}]$ with an energy resolution of 4 mV. The black arrow marks a broad peak at ~ 200 mV. (b) Spectrum recorded in the bias range $[-100\text{ mV}, 100\text{ mV}]$ with an energy resolution of 2 mV. Later on we will focus on the bias range circled in (b). Both spectra are taken at 12.5 K.

4.3.1 Single Point Spectrum

All the STS data shown here are taken on cleaved single crystal surfaces. The surface quality is examined before taking point spectra to ensure the reliability of the conclusion.

A single point spectrum in the bias voltage range $[-300\text{ mV}, 300\text{ mV}]$ is shown in Fig. 4.5a, taken on an electron-doped $BaFe_{1.8}Co_{0.2}As_2$ compound with $T_c = 25.3$ K. The black arrow indicates a broad peak at ~ 200 mV, which is related to a peak near the Fermi energy in the valence band spectrum measured by ARPES [59]. For

optimally Co-doped Ba-122 (T_c = 25 K), the peak position is 0.18 ± 0.02 meV below E_{F} [111], comparable to the peak position in our STM spectrum. The similar intensity of this near-E_{F} peak and the valance band peak suggests that the itinerant-electron physics rather than Mott physics is a more appropriate starting point for pnictides [59]. To see the details of the electronic structure around the Fermi level, another spectrum is taken within the bias range $[-100\ \mathrm{mV}, 100\ \mathrm{mV}]$ (see Fig. 4.5b) at the same spatial point as in (a). To clarify the feature of the superconducting gap, we will focus on the spectrum in the circled bias range in later discussions.

Figure 4.6a displays six typical single point spectra with $V_s = -20$ mV and $I_s = 40$ pA in the bias range $[-20\ \mathrm{mV}, 20\ \mathrm{mV}]$. The spectra show a clear superconducting gap structure with pronounced coherence peaks and a low differential conductance at the Fermi energy. This feature is present at all locations in the measurement region of the sample surface except near impurities. A single gap energy gap around $6 - 7$ meV is observed in all spectra, with a small variance at different spatial points and independent of the junction resistance. Furthermore, the superconducting nature of the gap is proved by vortex imaging, discussed in Sect. 4.4.

From the band structure calculation, the Fermi surface (FS) of the pnictides consist of two hole-like pockets (inner α band and outer β band) around the Γ point of the Brillouin zone (BZ) and two electron-like pockets at the M point (γ and δ band) of the BZ (see Fig. 1.5). This FS topology has been confirmed by different ARPES [59, 60, 61, 62] measurements, although FS details vary for different materials.

For the hole doped $Ba_{0.6}K_{0.4}Fe_2As_2$ [62] with a T_c of 38 K, multi-gaps open on

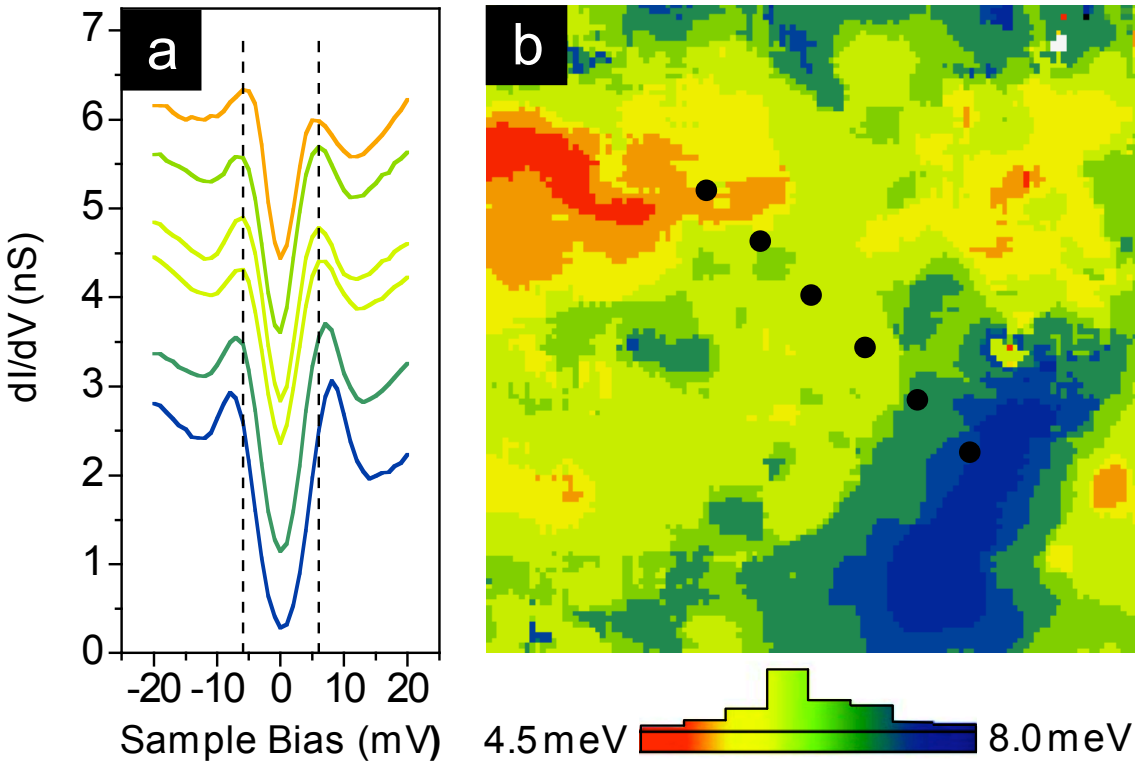

Figure 4.6: (a) A series of dI/dV spectra taken along a 11 nm line, illustrating the shape of the superconducting gap and the low differential conductance at the Fermi energy. The vertical dashed lines are guides to the eye located at ± 6 meV. (b) A $20 \times 20\,\mathrm{nm}^2$ gap map, revealing the spatial variation of the gap magnitude Δ. The gap has $\overline{\Delta} = 6.25$ meV and fractional variation only 12 %. A color-coded histogram of Δ is shown below the gap map. The six spectra in (a) (from top to bottom) are taken at the locations of the black points indicated in (b) (from upper left to lower right). Data were acquired at $T = 6.25$ K.

three different bands. The gap size is 12 meV on both α band and γ bands. On the β band there is a much smaller 3 meV gap. The similar gap sizes between the α band and the γ band lead to the author's suggestion that the inter-band interactions play an important role in the superconducting pairing mechanism. In contrast, for the electron doped $BaFe_{1.85}Co_{0.15}As_2$ [113], the α band is located entirely below the Fermi surface, leaving behind only the $\sim$ 6 meV gaps in the hole-like β band and M

centered bands with a similar gap size. Here the inter-band interactions may transfer to, between β and γ bands.

Our gap size of $6-7$ meV is in reasonable agreement with the gaps of a similar Co-doped $BaFe_{1.85}Co_{0.15}As_2$ measured in the ARPES report. STM spectra have average electronic structure in momentum space, and may have different weighting factors for different parts of the FS. Although the gap size in the β band is similar to that in the γ band, we cannot detect any hints of multi gaps in our STM spectra. Furthermore we show a single point spectra for an optimal hole doped $Sr_{1-x}K_xFe_2As_2$ in Fig. 4.7, the gap size of 5 meV is relatively compatible with the small gap on the β band measured with ARPES. In brief, we suggest that the gap measured in STM spectra may only represent information of the β band. The strong weighting on the β band is possibly related with the strong dispersion of the β band [114, 65].

However, all the superconducting gaps measured by ARPES are isotropic and nodeless in momentum space, with a less-than-20% anisotropy [62, 60]. To date, no clear information about the gap symmetry can be extracted from tunneling spectra. All spectra have been recorded at or above 4.2 K, so thermal broadening makes it difficult to extract the gap symmetry. Nodeless s-wave spectra may be smeared out, and fitting to the observed coherence peaks requires short quasiparticle lifetimes, which make s and d-wave fits indistinguishable. Ultra low temperature STS measurements are therefore expected to shed light on the gap symmetry mystery.

Most spectra have a V-shaped background, which is likely related to the normal state of the pnictides. This assumption is supported by the observation of V-shaped spectra in parent compounds [115, 116] and in vortex cores where superconductivity

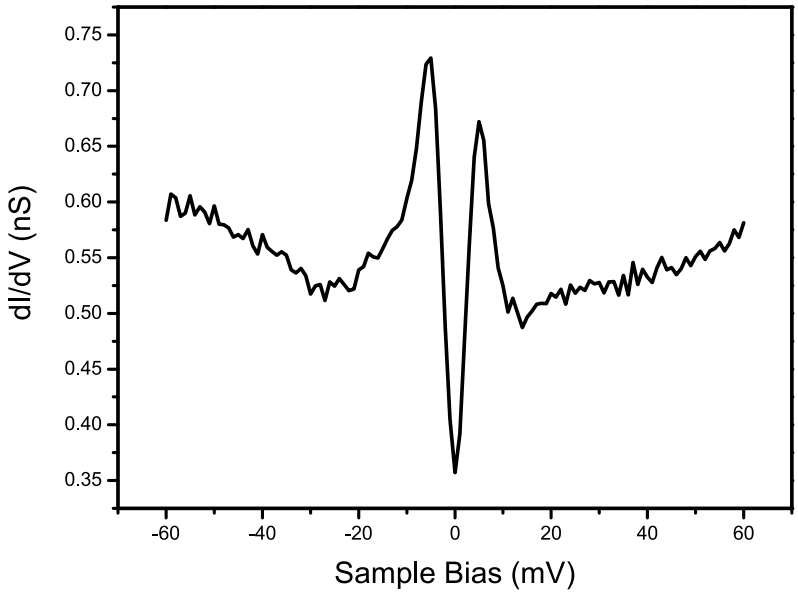

Figure 4.7: A single point dI/dV spectrum taken on the optimal hole doped $Sr_{1-x}K_xFe_2As_2$ with $V_s = -100$ mV and $I_s = 75$ pA. The spectrum is recorded in the bias range of $[-60\text{ mV}, 60\text{ mV}]$ at 6 K.

is suppressed (Fig. 4.13a). In Bi2212, by contrast, the background is roughly linear [70] and a dip-hump structure exists beyond the coherence peaks. The V-shaped background will have to be subtracted or normalized out in some fashion before any reasonable fit of the superconducting gap to obtain its symmetry.

4.3.2 Gap map

With the same STM/STS techniques used in Bi2212, a map of the magnitude of the superconducting gap Δ can be obtained for the pnictides. Fig. 4.6b shows such a gap map, taken at zero magnetic field and 6.25 K on $BaFe_{1.8}Co_{0.2}As_2$. The map

of the spatial dependence of Δ shows a total range of Δ from 4.5 to 8.0 meV. From the ∼16,000 measured spectra, we extract the average $\overline{\Delta} = 6.25$ meV and standard deviation $\sigma = 0.73$ meV. The fractional variation in gap size is calculated to be $\sigma/\overline{\Delta} = 12\%$. The gap maps reveal nm-sized patches of different gap magnitude.

One important character of spectral evolution in the map is that spectra with smaller gap energies tend to exhibit weaker coherence peaks and higher zero bias conductance (ZBC), as exemplified in Fig. 4.6a. This behavior in pnictides may be explained by impurity scattering [12, 13, 117] for an isotropic s-wave gap. Impurity scattering suppresses the order parameter, i.e., decreases the gap size. At the same time, the quasiparticle lifetime is reduced, leading to weaker coherence peaks.

Both electronic homogeneity and dependence of ZBC on the gap size in the pnictides differ remarkably from observations in the cuprates. The typical fractional variation reported in optimally doped Bi2212, $\overline{\Delta}/\sigma = 7$ meV/33 meV $\approx 21\%$ [93], is almost twice the value for Ba-122 samples. The smaller relative gap variation suggests a weaker role for intrinsic electronic inhomogeneity in the mechanism for high-T_c superconductivity in pnictides. For the inhomogeneous gaps in the cuprates, spectra show larger ZBC values with increasing gap magnitude, which is the opposite behavior to that of the pnictides [93].

A possible resolution to the contrast between pnictides and cuprates may arise from several recent studies of the pseudogap phase in the cuprates. Using a normalization technique, Boyer *et al.* reported the removal of the effects of the pseudogap and obtained a relatively homogeneous low temperature gap distribution in $Bi_2Sr_2CuO_{6+x}$ [118]. Ma *et al.* studied $Bi_2Sr_{2-x}La_xCuO_{6+\delta}$ and, due to the chosen

doping, were able to measure spectra in which the energy scales of superconducting gaps and pseudogaps were distinct [119]. In these studies, the separated superconducting gaps seem to show a different correlation between ZBC and gap magnitude compared to what is usually observed in the cuprates: the larger the gaps, the smaller the ZBC. Therefore, the apparent opposite relation between coherence peak height and gap width in the cuprates may be due to the pseudogap, which depletes the spectral weight for pairing [120].

With the single gap size of $6 - 7$ meV, the calculated reduced gap $2\overline{\Delta}/k_BT_c$ ranges from 5.5 to 6.4, falling in the strong coupling regime. This exceeds the values for weak-coupling s-wave or d-wave BCS superconductors, which are 3.5 and 4.3, respectively [121]. The reduced gap calculation is more complicated in the cuprates. From optimal doped to underdoped Bi-2212, the reduced gap ranges from 8.6 to values as high as 36 [93]. One suggestion is that the pseudogap critical temperature T^*, rather than T_c, is a more appropriate energy scale to describe the gap size [70]. Experiments which decouple the pseudogaps from superconducting gaps by coherent tunneling find reduced gap value 6 in the Bi-2212 cuprates. The extracted gap by normalization in Bi-2201 leads to a reduced gap ~ 10 [118]. But we should remember that even with raw gap sizes of optimal doped samples, the reduced gap for Bi-2201 is by a factor 2-3 larger than the one for Bi-2212 [122]. It is still too early to compare the reduced gap between the pnictides and the cuprates. The doping dependence of gap sizes for the pnictides is required in future studies.

4.4 Imaging of Vortex Lattice by STS

Vortex lattice geometry in BCS-type superconductors was first observed by the Bitter decoration [123]. Subsequent application of high resolution STM/STS techniques [124, 125] revealed detailed information about the vortex internal structure [124, 126]. The information about vortex core states, as well as vortex shape and interactions between vortices, is fundamentally linked to the properties, including pairing symmetry, of the superconducting charge carriers.

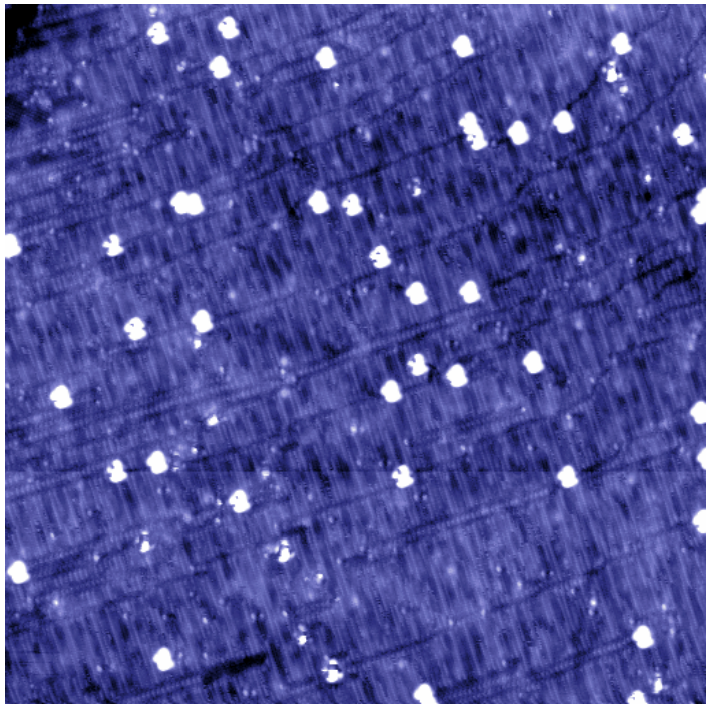

Figure 4.8: A 100-nm-square topographic image recorded in 9 T magnetic field with $V_s = -5$ mV and $I_s = 10$ pA. The bright spots are impurities.

4.4.1 Vortex Lattice Imaging

We image vortices electronically by mapping the conductance at an energy where a vortex alters the density of states. Under a 9 T magnetic field, we start with the fast conductance scanning method to scan a 100-nm-square area ($V_s = -5$ mV and $I_s = 10$ pA). The topographic image in Fig. 4.8 presents the stripelike surface similar to the zero field topography in Fig. 4.3. A conductance map is simultaneously recorded at $V_s = -5$ mV (see Fig. 4.9a), which is selected corresponding to the filled state coherence peak. A second conductance map at the same location, recorded at 6 T, is shown in Fig. 4.9b. In both maps, the vortices appear as broad depressions caused by the decreased DOS at the coherence peak energy inside the vortex. Impurities, possibly single Fe or Co vacancies, appear as sharper minima in the conductance, also visible as white spots in the simultaneously recorded topography.

After filtering out the impurities, a peak-fitting algorithm is used to extract the vortex center locations from the conductance maps. Voronoi cells [82] are over-laid onto the vortex image (Fig. 4.9c and d) and the average per-vortex flux $\bar{\phi}$ is calculated from the Voronoi cell size. We observe $\overline{\phi}(9\mathrm{T}) = 2.05 \times 10^{-15}\,\mathrm{T/m^2}$ and $\overline{\phi}(6\mathrm{T}) = 2.17 \times 10^{-15}\,\mathrm{T/m^2}$, in good agreement with the single magnetic flux quantum, $\phi_0 = h/2e = 2.07 \times 10^{-15}\,\mathrm{T/m^2}$.

Much can be learned about vortex interactions and pinning by studying the locations of vortices with respect to each other and to other structures within the superconductor. Vortex interactions can be roughly categorized into three scenarios. First, in the absence of strong pinning sites within the material, the vortex-vortex interaction force dominates, and the vortices crystallize into a hexagonal lattice, shown

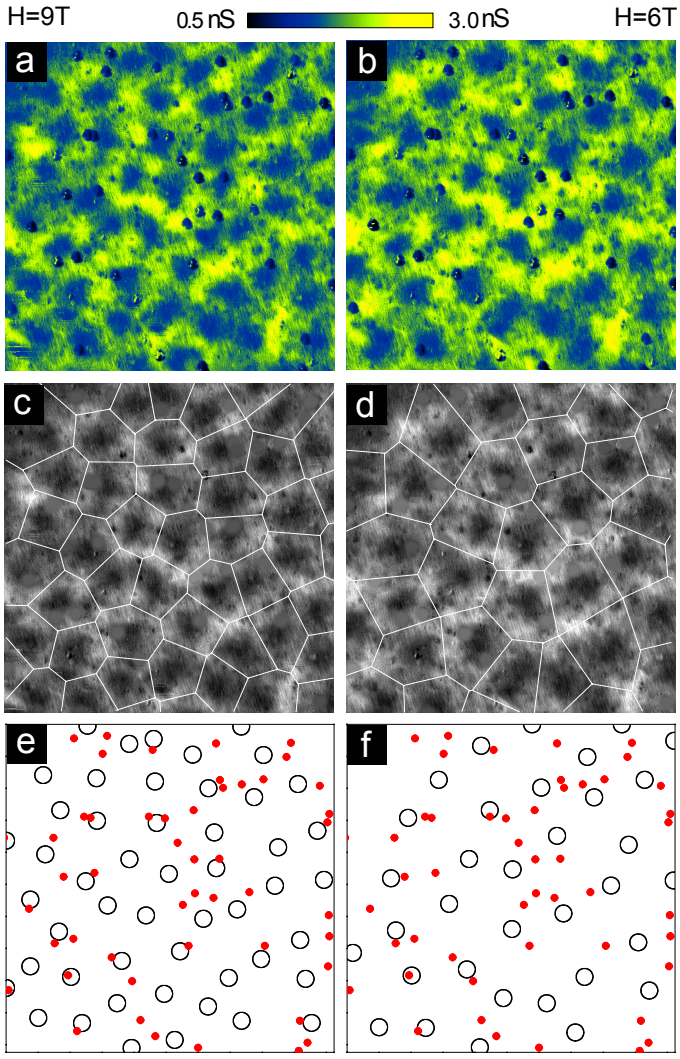

Figure 4.9: The 100-nm-square differential conductance maps recorded in 9 T (a) and 6 T(b) magnetic field, revealing the sample DOS at -5 meV. Vortices appear as dark features due to the suppression of the coherence peaks inside the vortex core. Vortices form a disordered lattice. (c),(d) A Voronoi overlay on impurity-filtered data emphasizes the vortices and demonstrates the procedure used to compute the average area associated with each vortex. (e),(f) Idealized data showing both vortices (open dark circles) and impurities. There is no statistically significant correlation between vortex and impurity locations.

schematically in Fig. 4.10a. For example, Fig. 4.10d shows the first STS-imaged vortex lattice in $NbSe_2$, recorded by Hess *et al.* [124], revealing an almost perfect

hexagonal symmetry.

In the presence of strong pinning sites, the vortex arrangement with respect to those sites depends on the anisotropy of the material. In highly anisotropic superconductors, a one-dimensional vortex line may split like a stack of pancakes into point-like objects with the freedom to move independently in each superconducting layer [127]. In this scenario, pancakes may find pinning sites independently in each layer, resulting in a high correlation between observed vortex and pinning locations in any given layer. This second scenario is shown schematically in Fig. 4.10b, and is realized in Bi2212 (Fig. 4.10e, Pan *et al.* [82]), where the vortices (depicted as circles of radius 30 Å) are clearly correlated with the impurities (visible as small, irregular black spots).

Finally, in a more isotropic superconductor with strong pinning sites, the vortices must remain as line objects, and can bend only slightly between layers to maximize their overlap with impurities throughout the bulk. In this scenario, there may be very little observable correlation between vortex locations and impurities in any one layer. This third scenario is depicted schematically in Fig. 4.10c.

As observed by low temperature STS imaging in the cuprates [97, 99, 82], the vortices imaged in $BaFe_{1.8}Co_{0.2}As_2$ form a disordered lattice, indicating the presence of strong pinning sites. This observation is consistent with recent small-angle neutron scattering experiments on a similar compound, $BaFe_{1.86}Co_{0.14}As_2$ [128]. In addition to the vortices, there are also sharp minima in conductance, independent of magnetic field, which may be attributed to strong scatterers near the surface. There is no correlation between the locations of the vortices and these near-surface impurities.

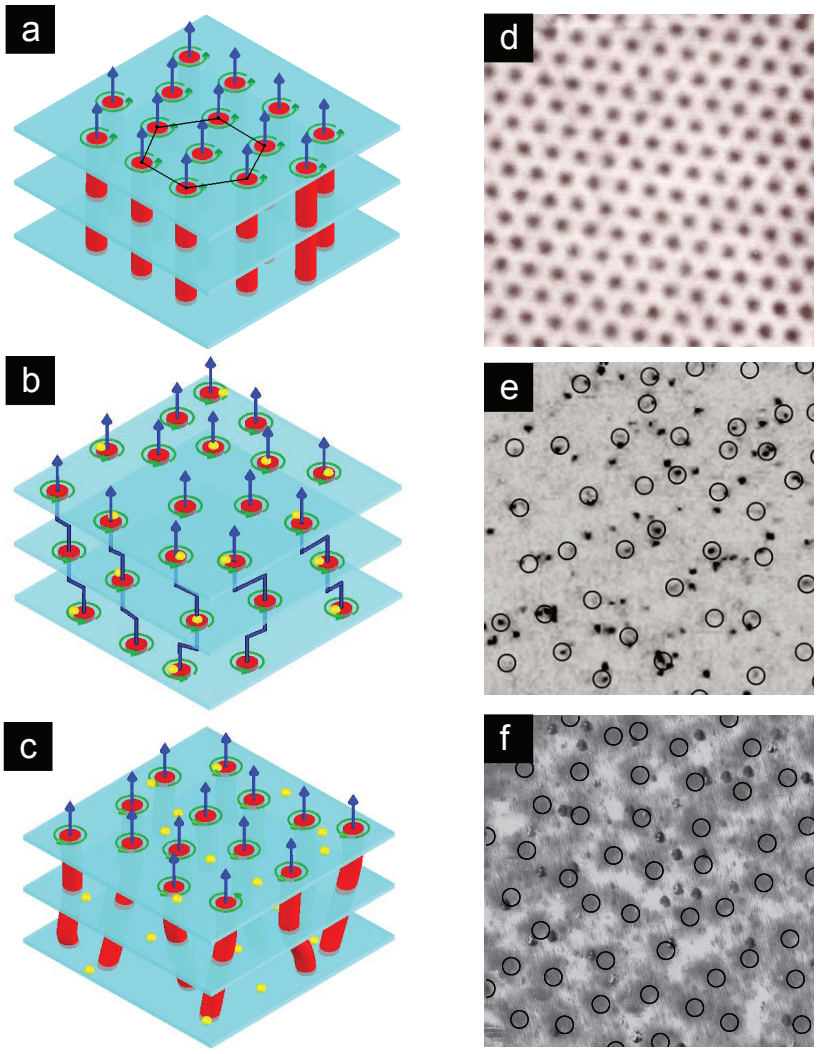

Figure 4.10: (a-c) Three different vortex interaction regimes. (a) Vortices in a clean superconductor. Both surface and bulk pinning are absent and the vortices arrange in a perfect hexagonal Abrikosov lattice due to the repulsion between vortices. (b) Pancake vortices in a superconductor with weak interlayer coupling. Some of the pancake vortices are pinned to impurities (yellow dots) within the layers and marked correlation between vortex and impurity locations is observed. Between the layers, pancake vortices are connected by Josephson vortices (blue lines). (c) Vortices in a superconductor where bulk pinning dominates. The flux penetrates the sample in a tubular fashion, but no hexagonal lattice can be formed as vortices are pinned by bulk defects. There is no correlation between surface defects and vortex locations. (d-f) Examples of these three scenarios, imaged by STS (d) in $NbSe_2$ [124] in 1 T magnetic field at 1.8 K, (e) in Bi-2212 [82] in 7 T magnetic field at 4.2 K, and (f) in $BaFe_{1.8}Co_{0.2}As_2$ [86] in 9 T magnetic field at 6.25 K.

Fig. 4.10f shows the same data as Fig. 4.9a but with vortex cores emphasized as circles of radius the coherence length. At 9 T, roughly 10.6% of the field of view is covered by vortex cores and 4 out of 49 impurities lie within a vortex core (see Fig. 4.9e). This number corresponds to roughly 8%, which is not a statistically significant deviation from 10.6%. This analysis proves that bulk pinning, and not surface pinning, must play a significant role in this superconductor.

Next we detect the direction dependence of the vortex structure. Because the local environments induce difference vortex shapes by the local perturbation, we filter out the impurities and average all the vortices in the conductance map (inset of Fig. 4.11). The dI/dV profiles, parallel to and 45° rotated with the crystal axis, are compared in Fig. 4.11. No obvious differences between two profiles are observed. In addition, the Fourier transformation of the vortex lattice is isotropic. Both phenomena indicate that vortices are isotropic, locally and globally, not significantly affected by the stripe-like surface feature, or by any residual one-dimensional spin or structural orders [66] within the bulk. The pnictide vortices without internal structures are also in contrast to predictions of d-wave vortices [129], and observations of 4-fold symmetric internal vortex structure in d-wave cuprates [100].

4.4.2 Vortex Spectroscopy

Local measurements in high magnetic field allow us to observe the destruction of superconductivity in vortex cores. Figure 4.12a shows the zero bias conductance (ZBC) from a 60-nm-square DOS map. The DOS map is taken in a region of Fig. 4.9a. Here the vortices appear as the enhanced subgap density of states, in contrast to Fig.

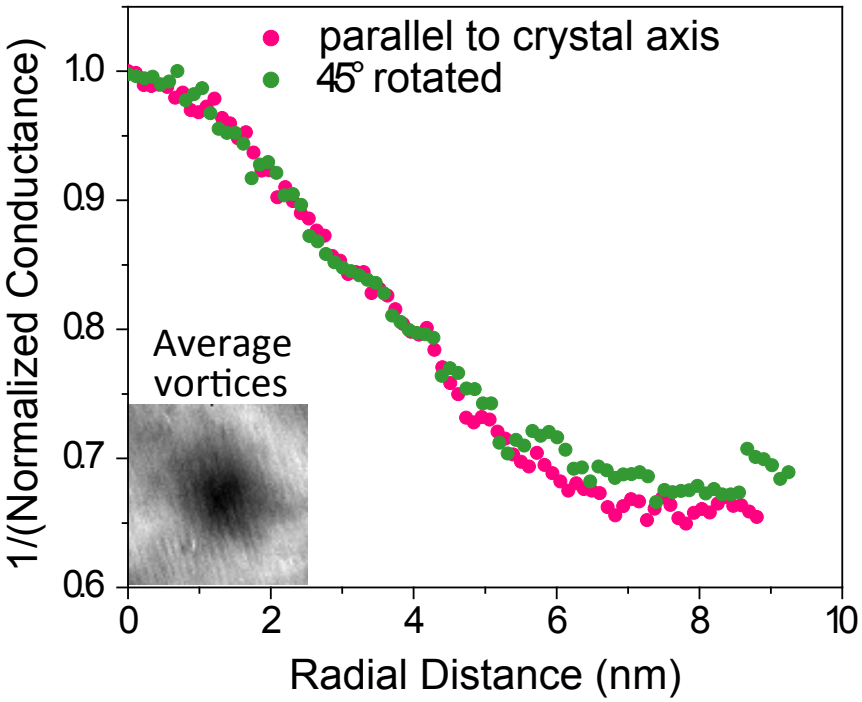

Figure 4.11: The radial distance dependence of the inverse of the normalized conductance. The two profiles are the 4-fold averaged conductance along the crystal axis and 45° rotated with the crystal axis. The absence of differences between the two profiles prove that the vortices are isotropic in space.

4.9, where the vortices appear as suppressed conductance due to the local suppression of coherence peaks. To see where the conductance contrast arises from, the dI/dV spectrum at the center of a vortex is shown together with a superconducting spectrum in between vortices in Fig. 4.12b. Compared to the superconducting spectrum, the vortex spectrum has a smaller conductance around the coherence peak voltage and a larger conductance at zero bias, leading to the vortex images in both Fig. 4.9a and Figure 4.12a.

Microscopic calculations of vortex core states show different spectral features,

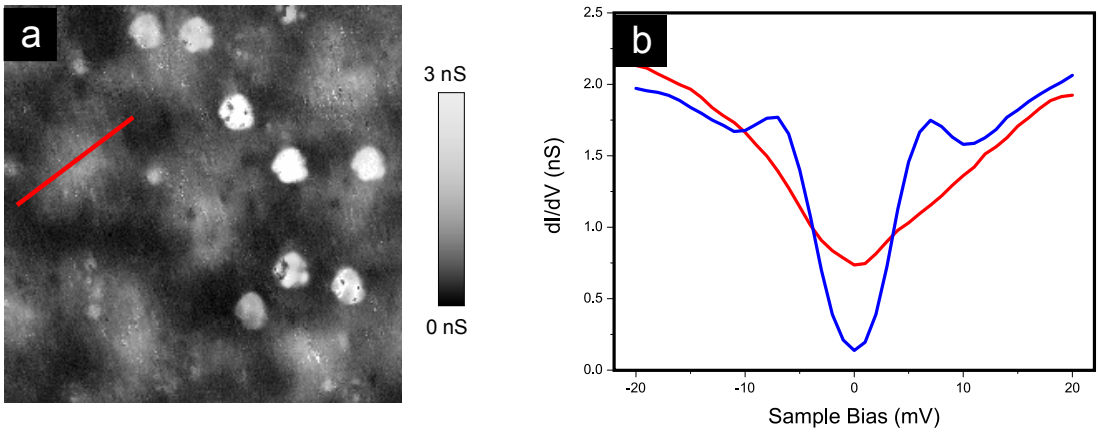

Figure 4.12: (a) A 40-nm-square map of the zero bias conductance in 9 T magnetic field at $T = 6.15$ K, showing ~ 8 vortices (broader, lighter objects). (b) The spectrum at the center of the vortex, compared with the superconducting spectrum, both taken at $V_s = -20$ mV and $I_s = 40$ pA.

varying with the pairing symmetry of the superconductor. Vortex core states in conventional s-wave superconductors are expected to show a ZBC peak, caused by tunneling of electrons to states bound with the vortex core [130, 131, 132]. It is important to note that the ZBC peak is observed only in clean superconductors, where the electronic mean free path ℓ is much larger than the coherence length ξ. For dirty superconductors, however, there is no ZBC peak and one observes instead an almost flat DOS, due to quasiparticle scattering [125].

In contrast to conventional s-wave superconductors in the clean limit, the conductance measured at the vortex center in $BaFe_{1.8}Co_{0.2}As_2$ shows only an enhanced sub-gap density of states but no ZBC peak (see Fig. 4.12b). This is also apparent in Fig. 4.13a where a linecut through one of the vortices at 9 T magnetic field is displayed. In Y123 [97] and Bi2212 [82], particle-hole symmetric subgap peaks have

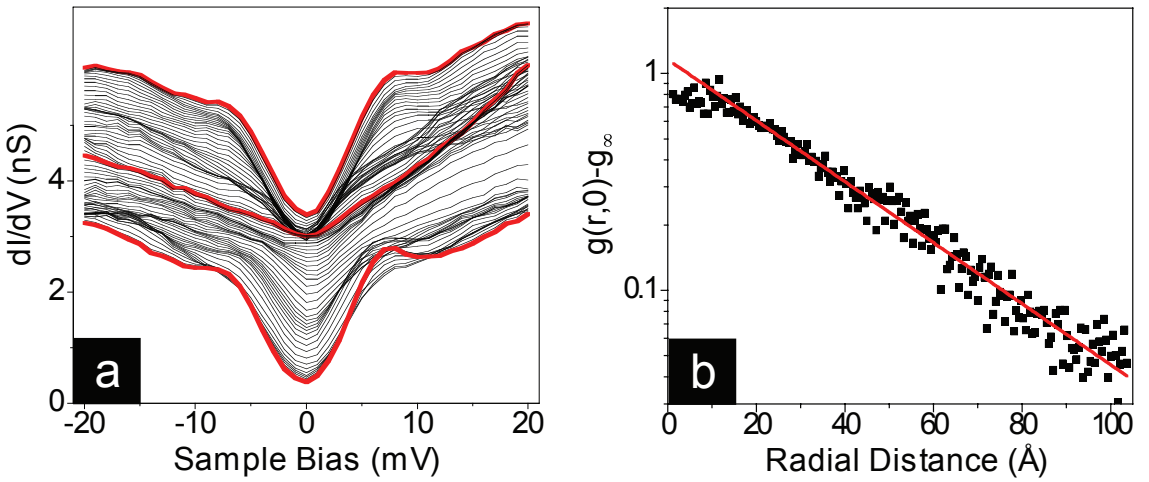

Figure 4.13: (a) A 14.5 nm long linecut of dI/dV spectra taken through a vortex location in $BaFe_{1.8}Co_{0.2}As_2$, showing the smooth evolution from the off-vortex DOS with pronounced coherence peaks to the on-vortex DOS with suppressed coherence peaks and no ZBC peak. The data were taken at 9 T magnetic field and $T = 6.15$ K. (b) Azimuthally averaged radial dependence of the differential conductance $g(r, 0)$ around a single vortex as measured (black squares) and fit by an exponential decay (red line, see text). The constant background g_∞ has been removed in order to emphasize the exponential decay on the logarithmic scale of the y-axis. The exponential fit leads to an average coherence length of $\xi = 27.6$ Å with standard deviation 2.9 Å for all vortices investigated.

been reported within vortex cores, with energies approximately $\pm\Delta/4$. We do not observe such particle-hole symmetric subgap states, although the corresponding low energy scale in this material, $\Delta/4 \sim 1.5\,\text{meV}$ would likely appear as a weak ZBC peak as well.

The spatial dependence of the vortex spectroscopy also enables the first direct measure of the superconducting coherence length in this material. We fit an exponential decay $g(r, 0) = g_\infty + A\exp(-r/\xi)$ within a distance of $r = 20$ to $100\,\text{Å}$ from

the vortex core, as shown in Fig. 4.13b. From several vortices, we find an average coherence length $\xi = 27.6\,\text{Å}$ with standard deviation 2.9 Å. Using the Ginzburg-Landau expression $H_{c2} = \phi_0/2\pi\xi^2$, we compute the upper critical field $H_{c2} = 43\,\text{T}$.

With residual resistivity $\rho_0 = 0.23\,\text{m}\Omega \cdot \text{cm}$ and Hall coefficient $R_H = 11 \times 10^{-9}\,\text{m}^3/\text{C}$, the electronic mean free path $\ell = \hbar(3\pi^2)^{1/3}/e^2 n^{2/3}\rho_0$ is approximately 81 Å. Given that our coherence length $\xi = 27.6\,\text{Å}$ is almost three times smaller than ℓ, the superconductor under investigation is considered to be a clean superconductor and therefore the lack of sub-gap peaks cannot be explained by scattering effects and remains an open question.

In contrast to the cuprates, where substitutions into the critical superconducting CuO_2 plane lead to strong scattering and the reduction of T_c [95, 103], the 10% of Co atoms doped directly into the superconducting FeAs plane in this material do not provide a strong scattering signature. Strong scatterers are dilute in this material, corresponding to only 0.029% of the Fe sites, leading to an average spacing comparable to $\ell \sim 81\,\text{Å}$.

4.5 Conclusion and Discussions

To summarize, we have presented the first atomically resolved STM/STS studies on a single crystal pnictide superconductor $BaFe_{1.8}Co_{0.2}As_2$ in magnetic fields up to 9 T. We observe a single gap with $\overline{\Delta} = 6.25\,\text{meV}$ and relative standard deviation only 12 %, in contrast to the more inhomogeneous and localized behavior of Δ in the cuprates. We have imaged a stationary but disordered vortex lattice, uncorrelated with the locations of surface impurities. This result demonstrates that vortices expe-

rience bulk pinning at fields up to 9 T, even in a clean single crystal of this pnictide with a low T_c ($\approx$ 25.3 K). The absence of sub-gap peaks within the vortex cores contrasts with observations in both d-wave cuprates and conventional s-wave superconductors. The Co dopants are found to have negligible effects on the density of states, in contrast to the dilute strong scatterers.

Although research in the pnictides is still in its early stage, there exist some significant achievements by STM/STS on these compounds. To date, STM/STS studies have contributed information about the cleaved surface structure, the superconducting gap, and vortex core states. Investigations of numerous surfaces have revealed a stripe like structure in almost all 122 compounds, both doped and un-doped. dI/dV spectra of doped single crystals show a clear superconducting gap with pronounced coherence peaks. In addition to single point spectra, maps of the gap distribution have been displayed on single crystalline 122 samples, providing information about the spatial inhomogeneity of the gap. From vortex imaging, a short coherence length is directly measured for the first time by any technique.

Looking forward, there are several key questions that remain to be addressed by STM/STS. The biggest roadblock to further STM/STS studies is the surface characterization. Surface morphologies are observed to depend sensitively on cleaving conditions. In addition, surface instability and polar cleavage planes are complex and unsolved problems. It is thus very difficult to achieve repeatable atomic resolution topographies on these compounds.

Another key issue is the gap symmetry. Single point spectra at ultra-low temperatures would allow better fitting without complications of thermal broadening. A

different approach to extract the gap symmetry is to probe the local DOS around both magnetic and non-magnetic impurities, which has been successfully applied to the cuprates [83, 95]. Similar experiments in pnictides together with the comparison to theory, could address the gap symmetry question.

The momentum space information might also be accessed by Fourier transforming DOS maps and extracting quasi-particle interference (QPI) patterns [126]. The QPI patterns should be used to explore the pairing symmetry as proposed in Ref. [133]: a detectable absence of interference peaks surrounding the reciprocal lattice vector would be evidence of the out-of-phase extended s-wave pairing.

In conclusion, there are a lot of potentials for STM/STS to contribute significantly to resolving the most important open questions in pnictide superconductivity, but additional work is needed to overcome surface-related challenges.

Chapter 5

Two Energy Scales in Cuprate Superconductors

Superconductivity is a collective phenomenon, arising from instability of the Fermi surface induced by electron-phonon (or electron-boson) interactions. Inspecting different interactions in a superconductor is essential to understand its superconducting mechanism. Normally, these interactions are also prone to induce competing or cooperating orders, such as magnetic orders. The dazzling array of orders can either conceal or elucidate the underlying superconducting mechanism.

Since the discovery of a peculiar pseudogap phase in cuprates [134], a debate has raged between scientists who interpret the pseudogap as a precursor of the superconducting state and those who think it is a different competing order [34, 135]. The number of gaps and their mechanism are the focus of recent studies [136, 137]. In this chapter, we use vortex imaging and a division normalization technique to separate two energy scales, providing more information to reveal the relation between the

pseudogap and superconducting mechanism.

5.1 The Pseudogap of Cuprate Superconductors

A pseudogap, defined as a gap feature of unknown origin in the electronic excitation above T_c, is observed in cuprate superconductors by a number of experimental techniques [134]. Nuclear magnetic resonance (NMR) experiments were the first to detect a normal state pseudogap in underdoped YBCO by measuring the spin-lattice relaxation rate [138] and the Knight shift [139]. Proportional to the spin susceptibility, these two variables were found to decrease with temperature below a characteristic temperature T^* ($> T_c$). This observation suggests that some spins remain paired above T_c, reducing magnetic susceptibility from spin fluctuations. A spin gap was proposed based on this discovery, and its formation is more like a broad crossover around T^* than a real phase transition. The pseudogap was later confirmed by other techniques which use charge channel detection, such as optical conductivity [140] and electronic specific heat [141]. Within the charge channel, the pseudogap is described by a depletion of the density of states (DOS) around the Fermi energy. The normal state gap feature has also been observed in spectra measured by ARPES [142, 143] and STM [98, 122]. These two techniques were quickly adapted to study cuprate superconductors, and provide more detailed information about the pseudogap.

In the overview of superconductivity (see Chap. 1), we discussed the gap symmetry in cuprate superconductors. A d-wave gap ($\Delta(\theta) = \Delta_{SM} \cos 2\theta$) opens on the Fermi surface, with a zero gap and maximum gap Δ_{SM} at nodal ($\theta = \pi/4$) and antinodal points ($\theta = 0$), respectively. This anisotropic superconducting gap is observed

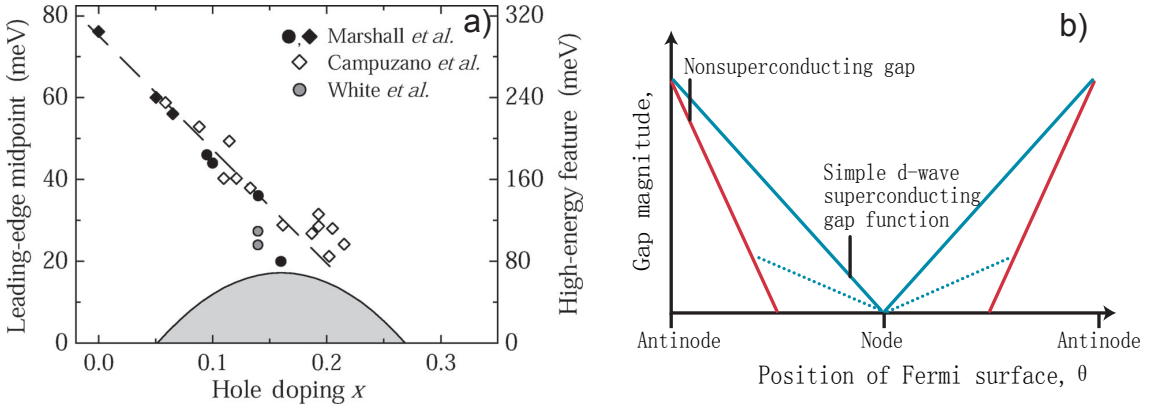

Figure 5.1: (a) The dashed line represents the doping dependence of pseudogaps in antinodal spectra (ARPES data for Bi-2212). The data points for this line were obtained by three groups. The dome-shaped line represents the doping dependence of T_c. Details of data are referred to the original paper. Cited from Ref. [144]. (b) Gap magnitude as a function of position on the Fermi surface. Solid blue line: simple d-wave gap function appropriate to the one-gap scenario. Dotted blue line: superconducting gap appropriate to the two-gap scenario; red line: pseudogap which exists in a broad temperature range below and above T_c. Cited from Ref. [137]. Here the d-wave function, $\cos 2\theta$, is simplified using a straight line. As of now, there is no consensus on the θ position of the maximum superconducting gap. The dotted line can be alternatively extrapolated to the antinodal point [119].

in ARPES data [17, 18]. Surprisingly, a similar 4-fold symmetry is found for the pseudogap phase well above T_c [142, 143], except for a gapless arc region around the nodal point [145]. Beyond the arc region, the pseudogap amplitude starts to increase, with maximum value, Δ_{PM}, at antinodal points. As the temperature increases from T_c to T^*, the gapless arc region expands [145] and the pseudogap is gradually filled in. The maximum pseudogap size Δ_{PM} decreases monotonically with doping [146] (data of the prototype Bi-2212 are shown in Fig. 5.1a), similar to the doping dependence of T^* [143] (see Fig. 1.2c). The superconducting gap and the pseudogap are connected

smoothly at T_c, i.e., Δ_{SM} is comparable with Δ_{PM}. As a result, Δ_{SM} also decreases with doping, not proportional to T_c as expected from the BCS theory. The pseudogap picture proposed by ARPES is corroborated by STM studies with better energy and spatial resolution [98]. The absolute bias voltage of coherence peaks in STM spectra correspond to Δ_{SM} and Δ_{PM}, below and above T_c, respectively. The gap feature also evolves smoothly through T_c without apparent changes [98, 122], consistent with the ARPES observation that Δ_{SM} and Δ_{PM} have similar values.

The doping dependence of Δ_{SM} and Δ_{PM} triggers a lot of debates on the physical nature of the pseudogap. One opinion is that the pseudogap is a precursor of the superconducting gap, consisting of non-coherent Cooper pairs [34]. When the temperature is decreased below T_c, Cooper pairs become coherent throughout the material, entering the superconducting state. In the precursor picture, the critical temperature T_c is determined by the superfluid density instead of the coupling strength [147, 148]. In the resonance valence bonding (RVB) theory, preformed pairs with a pseudogap energy scale above T_c are naturally described by the spin singlet liquid, and superconductivity results from the condensation of doped holes into the ground state [147]. The idea of preformed pairs arises directly from the smooth evolution of spectra through T_c and the similar momentum dependence of pseudogaps and superconducting gaps. Furthermore, short-range phase coherence is detected by high-frequency conductivity [149] above T_c and a phase with fluctuating vortices is discovered using the Nernst effect [150], giving support to the picture of the non-coherent state. However, the critical temperature determined by the Nernst effect has a dome shaped line above T_c, but does not reach up to the pseudogap critical

temperature, T^*.

The other opinion is that two different orders coexist on the Fermi surface, around antinodal and nodal points, respectively. Tanaka *et al.* extrapolated two distinct Fermi-momentum-dependent energy gaps in the superconducting state by ARPES measurements in deeply underdoped Bi-2212 [151]. In this two-gap scenario, the pseudogap is located around the antinodal points and exists together with the superconducting gap below T_c. The previous Δ_{SM} is either an energy scale representing a mixture of the pseudogap and the superconducting gap with similar sizes or just a pseudogap continuing below T_c. The schematic picture of the two-gap scenario is displayed in Fig. 5.1b. This scenario is supported by Raman studies which detected opposite doping dependence of two gaps [152]. In a STM study, Boyer *et al.* made a division normalization between spectra below and above T_c to separate two energy scales, and found a small gap hidden in the spectra [118]. The energy scale of the small gap, related to earlier observations of low-energy kinks in tunneling spectra [93], is believed to represent the real superconducting order.

External magnetic fields penetrate cuprates, forming magnetic vortices. Superconductivity is suppressed inside vortices and normal state vortex cores are separated by the surrounding superconducting state. Using the STS method under magnetic field to extract information on both normal and superconducting states at the same temperature, we expect to build another direction to explore the two-gap scenario.

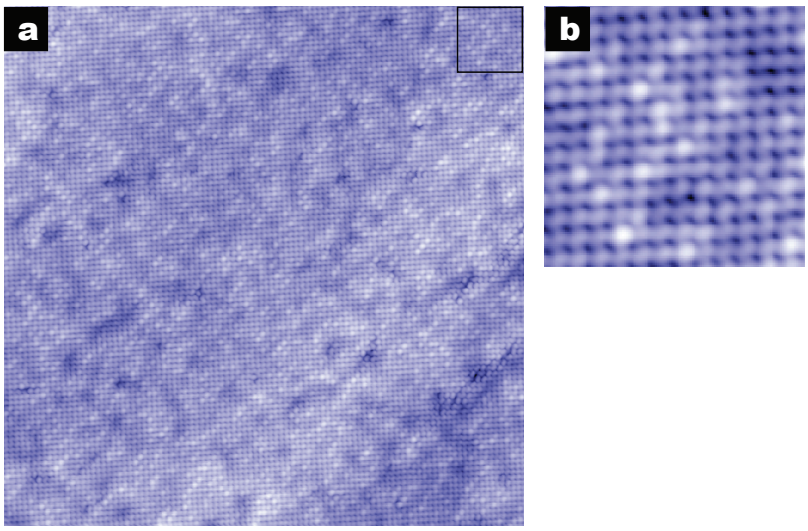

Figure 5.2: (a) 40×40 nm^2 topographic image of overdoped Pb-Bi2201 ($T_c = 15$ K). Bright atoms are doped Pb atoms on Bi sites. The top right frame of a 5-nm-square area is enlarged in (b) with a 4× magnification. The image is taken with $V_s = -100$ mV and $I_s = 100$ pA at $T = 6$ K.

5.2 Topography and Gap Inhomogeneity in Bi-2201

Bi-2212 is the most commonly studied cuprate in STM measurements, since it cleaves conveniently between two weakly bonded BiO sheets to expose a charge neutral and atomically flat plane. In our experiments, we choose a Pb-substituted Bi-2201 sample instead, with a low critical temperature of $T_c^{\max} = 35$ K. This choice fits the working temperature of our STM system. For all data shown in this chapter, the sample is overdoped $Bi_{2-y}Pb_ySi_2CuO_{6+\delta}$ [153] with $T_c = 15$ K.

The floating-zone-grown single crystal Pb-Bi2201 is cold cleaved in our cryogenic vacuum and inserted into the STM head. Bi-2201 exposes a flat BiO surface after cleaving, similar to Bi-2212 (see Fig. 2.5). An atomically resolved topographic image

of the BiO plane is shown in Fig. 5.2a. A subunit is enlarged for a better view of the Bi square lattice (Fig. 5.2b). In this square lattice, bright Pb atoms replace some Bi atoms, eliminating the incommensurate supermodulation structure [80]. The electronic structure is not affected by the change due to the Pb-induced surface structure, at least within the measurement range of ±100 meV around the Fermi level.

After choosing a clean area with an atomically resolved topographic image, the single point dI/dV spectra are taken at different spatial locations. The measured dI/dV spectra are believed to originate from the CuO_2 plane, separated from the STM tip by insulating BiO and SrO layers. Three representative spectra are displayed in Fig. 5.3. The top spectrum with a small superconducting gap has sharp coherence peaks, and the gap size is estimated by half the distance between coherence peaks. For the bottom spectrum with a large gap, the coherence peaks are suppressed, and the bias voltage value for the maximum conductance is used to determine the gap size. Notice that the gap size extracted from STM measurements corresponds to the maximum value at antinodal points on the Fermi surface (see Fig. 2.4). A negative correlation between the gap size and the coherence peak sharpness was also found in Bi-2212 [91]. For pnictides, we observed that the gap size is positively correlated with coherence peak sharpness, which is attributed to impurity scattering. The opposite behavior in cuprates implies a different mechanism. Unlike pnictides with a $s_{\pm}$ symmetric gap, cuprates have a d-wave superconducting gap. In the last paragraph of this section, we will discuss the origin of the antinodal gap inhomogeneity.

By measuring a survey of point spectra on this clean area, we collect the three-dimensional data set of the DOS. A gap map is subsequently extracted, shown in Fig.

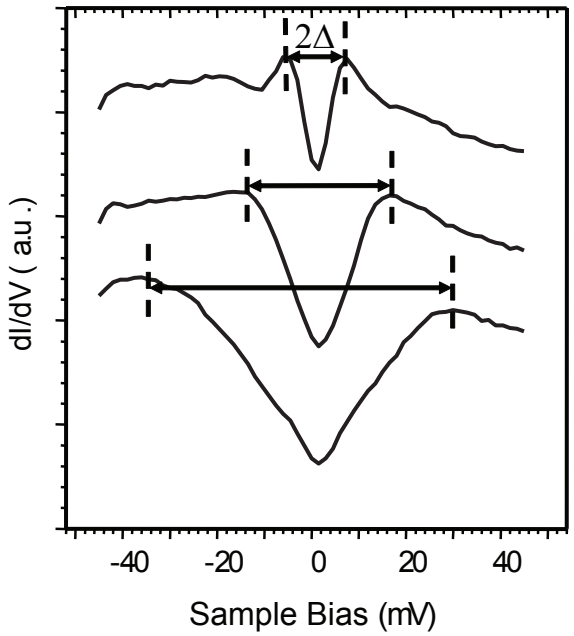

Figure 5.3: Three characteristic dI/dV spectra of overdoped Pb-Bi2201 ($T_c = 15$ K) taken at three different spatial points, respectively. The spectrum is recorded in the bias range of $[-45\text{ mV}, 45\text{ mV}]$, with $V_s = -100$ mV and $I_s = 100$ pA at $T = 6$ K. A gap size is defined by half the distance between coherence peaks as shown in the figure. The spectra show variant gap sizes and spectrum shapes, presenting the electronic inhomogeneity.

5.4a. The dI/dV spectrum shape and the gap size vary largely as the spatial location changes. This spatial inhomogeneity is nm-scale, which is well known in Bi-2212 [92]. Next we sort dI/dV spectra and average those with the same gap size. The negative correlation between the gap size and the peak sharpness holds for the averaged sorted spectra in Fig. 5.4b as well. The spatially variant apparent gap size is denoted as Δ_{inhomog}.

The inhomogeneity of dI/dV spectra and gap map in cuprates has been well discussed [70]. Earlier studies are focused on two issues: whether the inhomogeneity

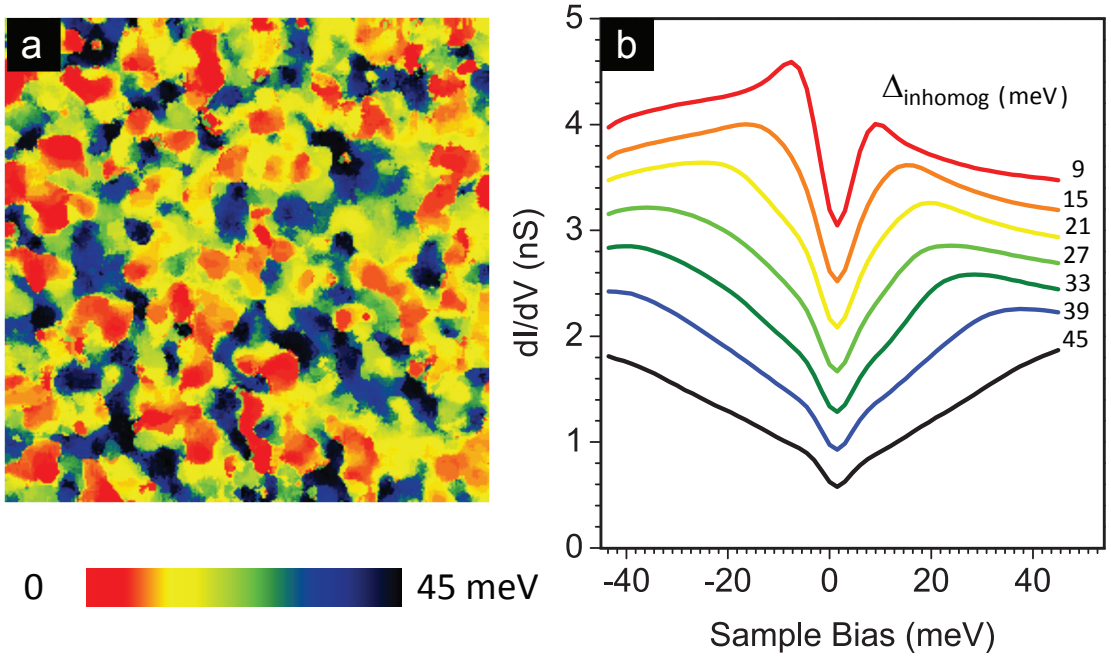

Figure 5.4: (a) 40×40 nm^2 gap map of overdoped Pb-Bi2201 (T_c = 15 K). The gap map is calculated from a 256×256 pixel spectral survey which is recorded with the same condition as in Fig. 5.3. (b) The averaged dI/dV spectra associated with different Δ_{inhomog} are sorted by increasing Δ_{inhomog}, from top to bottom. All spectra are extracted from the same 256×256 pixel spectral survey referred to in (a). Spectra with different Δ_{inhomg} are shown with even vertical offsets to enhance visibility.

is a universal phenomenon for cuprates and whether homogeneous samples can be achieved through oxygen annealing [154]. As emphasized by McElroy [155], the STM spectrum is a convolution of the tip and surface shape, and a blunt tip may lead to a homogeneous DOS map. With the improvement of experimental techniques, the existence of the inhomogeneity is generally accepted [70]. Inhomogeneity is ascribed to the random distribution of doped oxygen atoms [156], and the local gap size becomes larger closer to oxygen atoms. This relation is further verified by the partial Fourier transformation of DOS maps in Bi2201 [157]. It is reported that the antinodal spectra

gradually lose the coherence peak intensity as the doping value decreases [158], due to the decreasing superfluid density upon underdoping. This observation provides us a reasonable interpretation of the spectral inhomogeneity in cuprates: a spectrum with a larger gap size is more possibly from the underdoped regime, and its coherence peaks are less pronounced. The spectral inhomogeneity requires us to track the same scan area atom-by-atom when performing any mathematical operations between DOS maps under different conditions.

5.3 Division Normalization in Superconductors

For the same Pb-Bi2201, Boyer *et al.* tracked DOS maps on the same area below and above T_c, and used the division normalization to extract a hidden small gap [118]. This small gap is buried in an apparent broad gap before division and vanishes near T_c, implying that it may represent the real superconducting order. The apparent broad gap is associated with the pseudogap, which coexists with the superconducting gap below T_c. A STS spectrum is convoluted with thermal broadening, which limits the application of dividing spectra at two temperatures. On the other hand, an external magnetic field can suppress the superconducting state completely above H_{c2}, or inside vortices between H_{c1} and H_{c2}. The division approach can be extended to comparing spectra at zero (without vortices) and moderate non-zero (with vortices) fields. More importantly, we can address a crucial question for the normal state inside vortices: is it a pseudogap state? The answer to this question can facilitate fundamental understanding of high-T_c superconductors. In our low temperature STM system, we can measure atomically resolved spectra and track atoms under a magnetic field

($H \leq 9$ T) and/or temperature ($T \leq 20$ K). Accordingly, we will apply the division normalization approach under magnetic fields to investigate the two-gap scenario.

In Chap. 2, we presented the superconducting DOS derived in BCS theory in Eq. 2.4. Here we recall this equation,

$$N_s = N_0 \frac{\varepsilon'}{\sqrt{\varepsilon'^2 - \Delta^2}}; \quad \varepsilon' = \varepsilon - i\Gamma, \tag{5.1}$$

where N_0 is the normal state DOS, Δ is the gap size, ε is the energy, referenced to the Fermi energy, and Γ is the dissipation rate. In elementary superconductors, the normal state is metallic and N_0 is a constant near the Fermi surface. In intermetallic compounds and ceramic oxides, the normal state becomes more complicated due to possible coexisting orders. As a function of energy ε and spatial coordinate $\vec{r}$, the normal state DOS N_0 can bury information of the superconducting gap Δ in the spectrum of N_s. If we obtain N_0 by a reliable approximation, the real superconducting information can be extracted by the following,

$$\frac{N_s(\vec{r}, \varepsilon)}{N_0(\vec{r}, \varepsilon)} = \frac{\varepsilon'}{\sqrt{\varepsilon'^2 - \Delta^2}}. \tag{5.2}$$

By assuming N_0 is weakly dependent on temperature, Boyer *et al.* used a dI/dV spectrum at a temperature T_N slightly above T_c to approximate the normal state DOS [118]. We also notice that the temperature to approximate N_0 is well above T_c in Ref. [159].

In our experiments under magnetic fields, superconducting and normal states exist outside and inside vortex cores, respectively. Due to the spatial dependence of the DOS, it is impossible to directly compare N_s and N_0 within the same DOS map. Since the whole system is in the superconducting state at zero field, the division

normalization can be alternatively realized by dividing the DOS map at zero field by another in the same spatial region at a nonzero field. The assumption behind this approach is that N_0 weakly depends on magnetic field H. A schematic picture of our division approach with vortex imaging is shown in Fig. 5.5. At zero field, dI/dV spectra at all spatial locations correspond to the superconducting DOS N_s (red curves). At a moderate nonzero field, spectra in the superconducting regime are still N_s whereas those inside vortices become the normal state DOS N_0 (black straight lines). After the division normalization, spectra inside vortices present the information of Δ whereas those outside vortices become trivial constants. However, things can become much more complicated in real experiments.

As discussed in the beginning of this chapter, microscopic interactions induce physical orders. For example, charge density wave (CDW) and spin density wave (SDW) are two orders triggered by electron-phonon and electron-electron interactions, respectively [160]. Various orders can coexist, behaving differently as measurement conditions change: phase separation (orders vary spatially) in real space or segment variation on the Fermi surface in momentum space. A good example is 2H-$NeSe_2$ with a CDW order below 33 K and a superconducting order below 7.2 K [161]. These two orders coexist below 7.2 K and are predicted to be well separated in momentum space. ARPES, as a momentum-resolved technique, is normally expected to detect such coexisting orders. As a spatially-resolved technique, STM produce spectra as weighted averages of spectra around the Fermi surface. In 2H-$NeSe_2$, since the CDW and superconductor orders have well separated energy scales, STM can also distinguish these two orders (gaps) in the averaged spectrum.

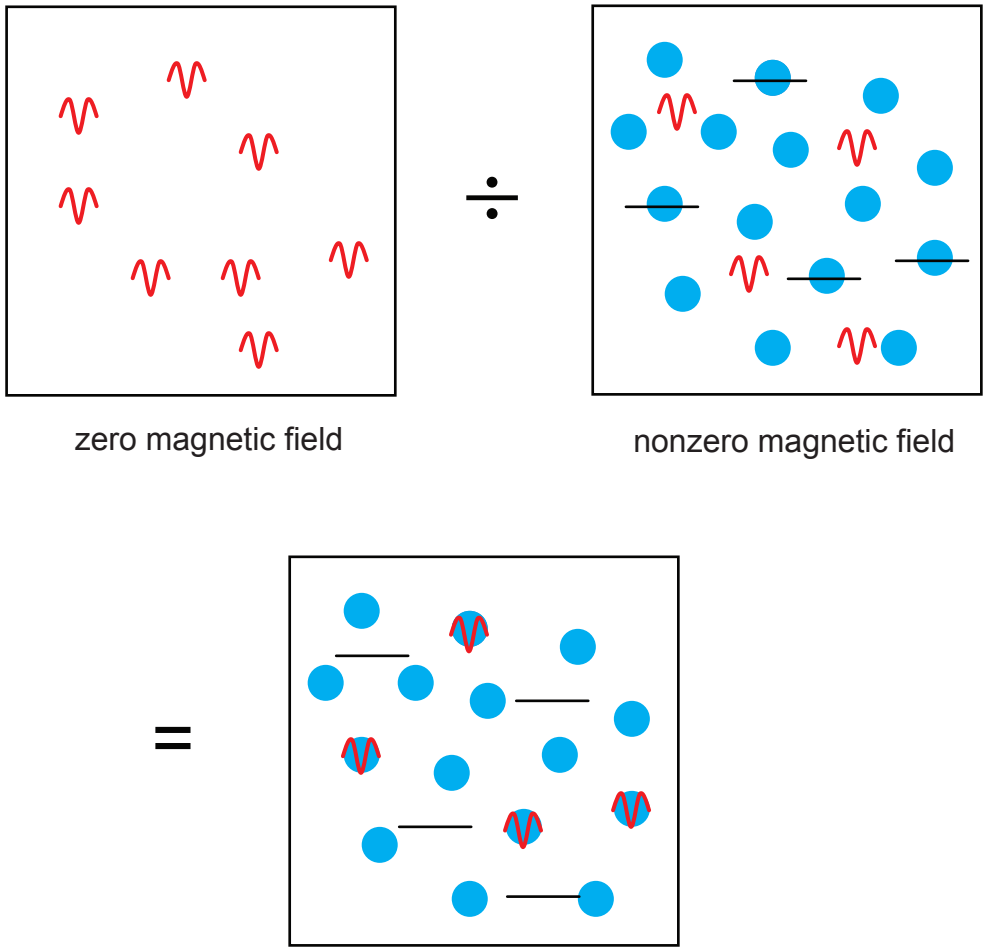

Figure 5.5: Schematic diagram for the division normalization under magnetic field. At zero field, red curves represent superconducting DOS N_s at all spatial locations. At a moderate nonzero field, the spectra inside blue vortices become the normal state DOS N_0. For simplicity, without considering its structure, N_0 is represented by a constant metallic DOS (black straight lines). After the division, information of Δ is extracted in spectra inside vortices, independent of the possible complicated structure of N_0. Outside vortices, the divided results are trivial constants.

Before presenting our experimental results, we discuss several possible difficulties in the division normalization approach:

1. Both the normal state DOS N_0 and the superconducting gap Δ depend on the angle θ along the Fermi surface. Accordingly, the explicit normalization formula for d-wave superconductors is rewritten as

$$\frac{\overline{N}_s(\varepsilon)}{\overline{N}_0(\varepsilon)} = \frac{\int N_0(\varepsilon,\theta)\frac{|\varepsilon|}{\sqrt{\varepsilon^2-\Delta(\theta)^2}}d\theta}{\int N_0(\varepsilon,\theta)d\theta}, \tag{5.3}$$

where $\overline{N}_s$ and $\overline{N}_0$ are averaged DOS, measured by STM. The normal state DOS is still mixed in the spectrum after division. However, if we assume a d-wave pseudogap (similar to the superconducting spectrum function) and Δ_{PM} in N_0 is well separated from Δ_{SM} (applicable in Bi-2201), the division can still produce a reliable spectrum of Δ_{SM}. A simulated example with $\Delta_{PM} = 25$ meV and $\Delta_{SM} = 7$ meV is shown in Fig. 5.6, from which we can find that the gap size from division is almost the same as the exact Δ_{SM}.

2. When a magnetic field is applied along the c-axis of layered cuprates, a screening supercurrent flows around vortex cores within the ab plane. The Doppler shift from the supercurrent was used to explain the sub-gap splitting within vortices of $NbSe_2$ [81], which has never been reported in cuprates. The Doppler shift may change the energy of quasiparticles near vortices, and the gap size would become a function of distance to the vortex core [162]. For spectra outside vortices in Bi-2212, various reports demonstrate that spectra in between vortex cores at 6 T are almost the same as those at zero field [70]. Although the Doppler shift may be hidden in the lifetime effect of a smoothed spectrum [70], we can assume that the supercurrent only has a negligible orbital-depairing effect for spectra near vortex cores. The Doppler shift thus will not affect our general conclusions.

3. In general, a vortex core is considered to be in the normal state. However,

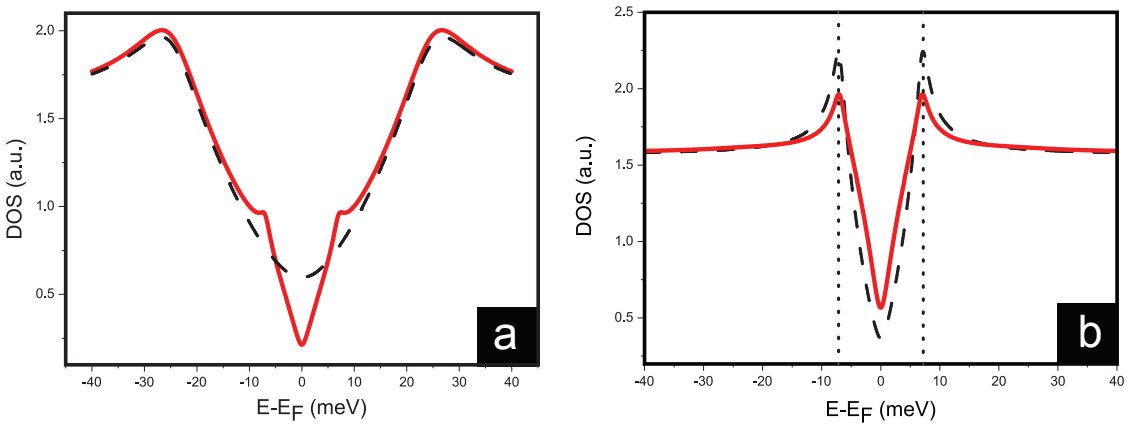

Figure 5.6: (a) The simulated normal and superconducting states DOS are plotted: the black dashed line denotes N_0 whereas the red solid line denotes N_s. Both the pseudogap and the pure superconducting gap are assumed to follow the d-wave function in Eq. 2.7. The chosen parameters are $\Delta_{PM} = 25$ meV, $\Gamma_{PM} = 5$ meV, $\Delta_{SM} = 7$ meV, and $\Gamma_{SM} = 0.7$ meV. (b) The normalized spectrum after dividing N_s over N_0 (red solid line) vs. the exact superconducting spectrum (black dashed line). For a better view, all the DOS of the solid line are multiplied by a constant of 1.58. These two lines share almost the same peak bias energies at 7 meV. The gap depth of the normalized spectrum is smeared out due to incomplete removal of N_0.

as shown by some experiments (e.g., the isolated state in $NeSe_2$ [81]), vortex spectra also exhibit nontrivial structures. For cuprates, a pair of symmetric subgap peaks are observed in vortex spectra of Bi-2212 and YBCO, although a conclusive picture is not yet reached. As we know, vortex spectra were not reported in the past for Bi-2201. Nevertheless, subgap peaks in vortex spectra may result in symmetric dips in the normalized spectra after division. Such dip features are not observed in any of our normalized spectra.

5.4 Division Normalization under Magnetic Field and Possible Vortex Liquid State

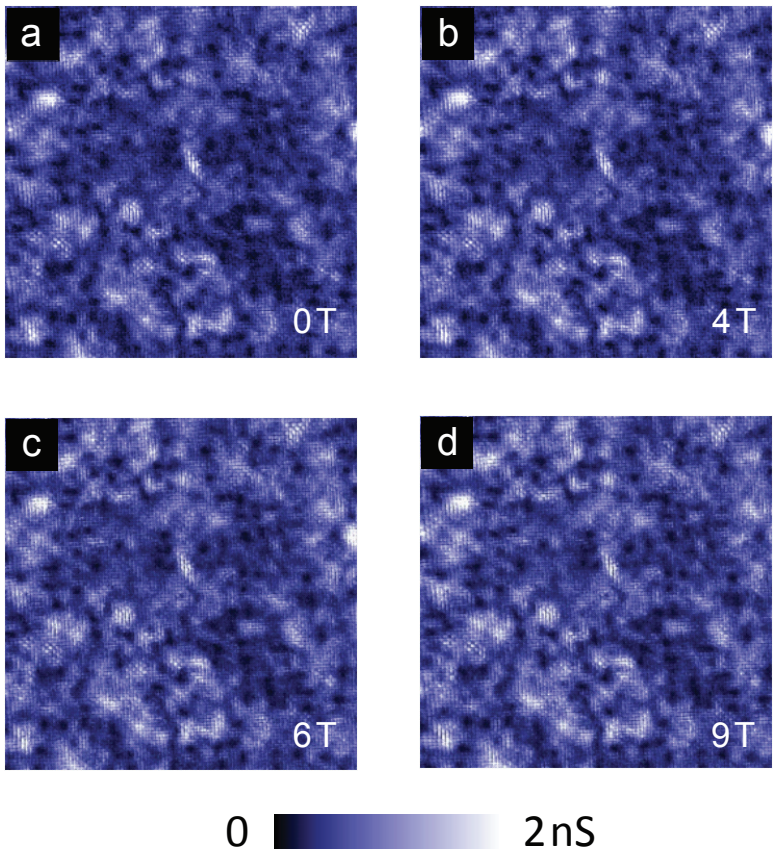

Figure 5.7: 40×40 nm^2 zero bias conductance maps taken at the same scan area under magnetic fields of 0T, 4T, 6T and 9 T, respectively ($T = 6$ K). All maps share the same color bar. No obvious changes are observable between the zero field map and nonzero field maps. In particular, vortex images are not detected in three nonzero field maps.

The external magnetic field is applied along the c-axis of a single crystal Bi-2201. By carefully tracking topographic images, four DOS maps at the same scan area (40-

nm square) are taken under magnetic fields of 0 T, 4 T, 6 T and 9 T, respectively. Following the vortex imaging approach (similar to that in pnictides), we use the dI/dV conductance at zero bias voltage to extract vortices. The resulting zero-bias conductance maps for four magnetic fields are shown in Fig. 5.7. We do not observe distinct vortices at all three moderate nonzero fields. In addition, these three nonzero-field conductance maps are qualitatively the same as that at zero field. To further clarify, we sort dI/dV spectra and average those with same gap sizes for each DOS map. As shown in Fig. 5.8, we observe that the negative correlation between gap size and peak sharpness is persistent for all magnetic fields H. For each gap size, the averaged conductance spectra almost do not change with field. On the other hand, as H increases, spectra become subtly smoothed out: both peak height and zero-bias well depth decrease for all gap sizes. Straightforwardly, we can raise two interesting questions: what exact changes to the electronic structure are brought by external magnetic fields and why are vortices not observed in conductance maps? The first question will be explored by the division normalization method whereas the second will be discussed following our analysis.

Despite the absence of vortices, we make a point-by-point division of zero-field spectra over nonzero-field spectra. A careful cross correlation between two maps is performed to register the same spatial location for each atom before the division. After dividing the DOS map at 0 T over another one at 9 T, we subsequently extract a new gap map from the normalized DOS map (see Fig. 5.9a). Compared to the original zero-field gap map in Fig. 5.4a, the normalized gap map is much less inhomogeneous with gap sizes in the vicinity of 7 meV. The spatial homogeneity of gap sizes is

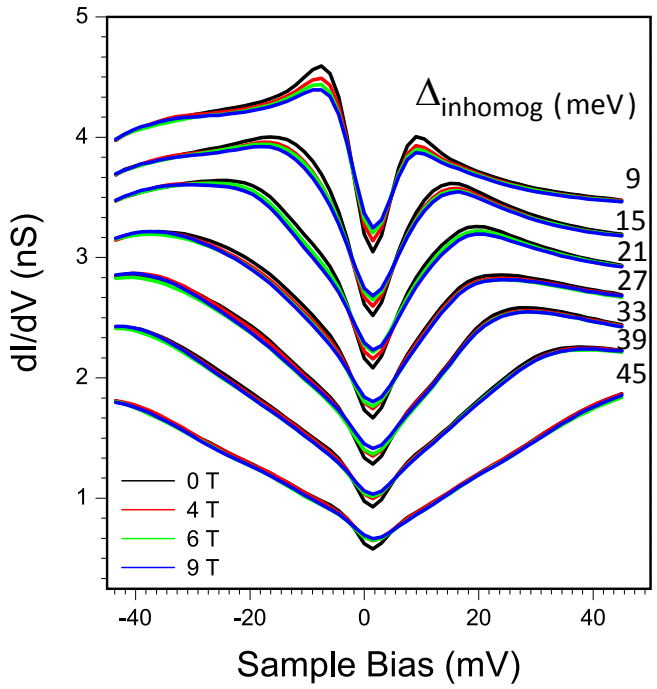

Figure 5.8: A set of spectra taken at different magnetic fields. Each spectrum is an average of spectra with the same gap size in a single DOS map. These lines are sorted by increasing apparent gap size (9 meV $\leq \Delta_{\text{inhomg}} \leq$ 45 meV), from top to bottom. For each Δ_{inhomg}, the spectra exhibit similar shapes as field increases. Spectra with different Δ_{inhomg} are shown with even vertical offsets to enhance visibility.

also observed in other normalized gap maps using 4 T and 6 T DOS maps as the denominator.

We further do the point by point division between zero-field and in-field DOS maps and average the divided spectra with the same zero-field gap sizes. The normalized spectra are presented in Fig. 5.9b, where the corresponding apparent gap size Δ_{inhomg} is labeled for each curve. Small gap sizes from these normalized spectra with a broad range of apparent gaps are all around 7 meV, with very small variation. In other words, the previous inhomogeneity of apparent gaps disappears in normalized spectra, and the hidden order Δ_{homog} is homogeneous. In addition, gap sizes of normalized

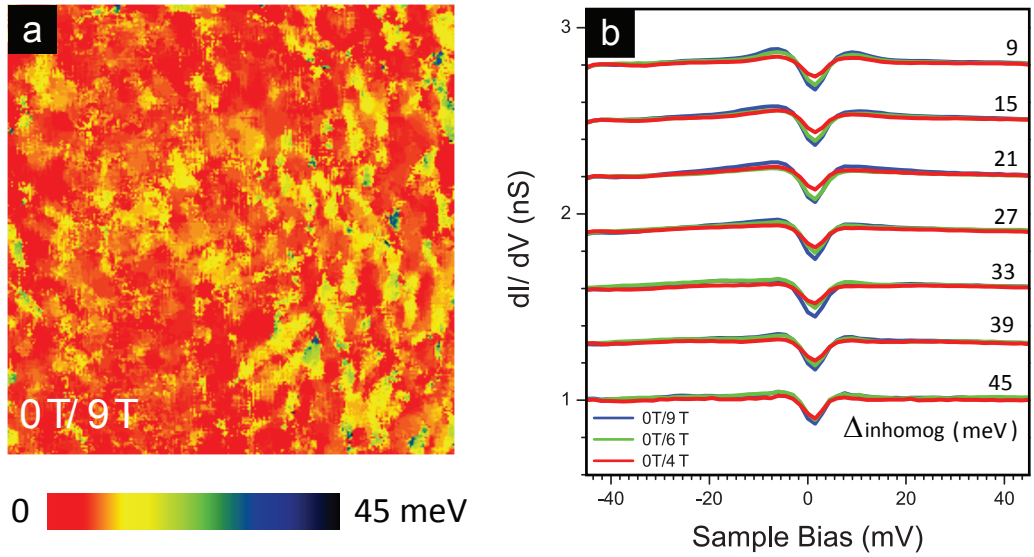

Figure 5.9: (a) By dividing the 0 T DOS map over the 9 T DOS map, a 40×40 nm^2 gap map is extracted. The color scale is the same as that for Fig. 5.4a. A homogeneous gap spans the whole area. (b) By divide the zero-field and in-field DOS maps point by point, the divided spectra with the same zero-field gap sizes are averaged. The normalized spectra exhibit gaps with very similar sizes, independent of the apparent gap size Δ_{inhomeg}. The gap depth increases with field.

spectra are almost independent of the magnetic field H.

Finally, we average all dI/dV spectra for each DOS map, and divide the overall-averaged spectrum at zero field over those at three nonzero fields, respectively. The overall normalized spectra for 4 T, 6 T and 9 T are compared in Fig. 5.10. This analysis effectively cancels out possible errors induced by imperfect spatial registration between different DOS maps. It is clear that the small gaps Δ_{homog} are almost the same (≈ 7 meV) for all three fields, and only peak heights and zero-bias well depths increase with field (see Fig. 5.10b). We note that our results are in good agreement

with those obtained by the division over different temperatures in Ref. [118]. Both experiments separate two types of gaps: the apparent one Δ_{inhomog} is inhomogeneous with a broad range whereas the hidden one Δ_{homog} is homogeneous. The values of the hidden gaps are also quantitatively the same: $\Delta = 6.7 \pm 1.6$ meV in Ref. [118] and $\Delta_{\text{homog}} = 7$ meV in our experiment. All these consistencies from two different experimental techniques indicate that the small gap extracted by the division normalization should represent a real physical order. Although further experimental evidence is required, we agree with Boyer *et al.* that the small gap reveals the superconducting order and the apparent gap should be referred to the pseudogap.

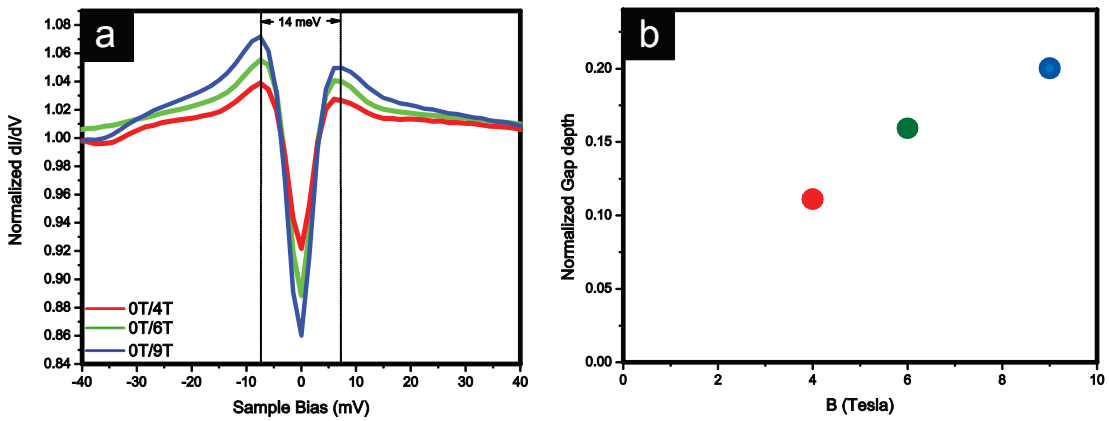

Figure 5.10: (a) The overall-averaged spectra for each DOS map are used to produce the normalized spectra by dividing zero-field spectrum over three nonzero-field spectra (blue line from 9 T, green line from 6 T, and red line from 4 T). A small gap ≈ 7 meV is presented for all the three normalized spectra. The gap depth, calculated by the vertical distance from the coherence peak (the average of two peaks) to the gap bottom, increases with field. The results of gap depths are plotted in (b), associated with the same color for each field. To demonstrate the effect of increasing field in the division normalization, a simulation is tested in App. A.

On the other hand, the reason for the absence of visible vortices still needs to be

answered. One possibility is that all three fields used in our experiment are higher than H_{c2}, under which the whole system is in the normal state and no vortices exist. The gradual evolution of spectra with increasing H only reflects the field dependence of normal state DOS in this case. Another possibility is that the system is in a vortex liquid state under the three fields we chose. Given the quasi two-dimensional layered structure of cuprates, vortices are very sensitive to thermal fluctuations and the vortex liquid state occupies a large phase space in the $H-T$ phase diagram. In our experimental time scale (10 ms) which is much larger than the vortex lifetime in the liquid state, the spectrum at each spatial location is a weighted average of both N_s and N_0. The weight of N_0 in the measured spectrum is proportional to the vortex density, which increases with the magnetic field H.

Figures 5.11a-b present a set of c-axis resistivity ρ_c [164] data for a Pb-Bi2201 with $T_c = 13$ K (from [163]). The temperature and field dependence of ρ_c exhibits a semiconductor-like upturn and a crossover peak, respectively. These two characters arise from the competition between tunneling channels of Cooper pairs and quasiparticles. The zero-resistivity temperature $T_{\rho=0}$ in Fig. 5.11a is related to the irreversibility field [165], which can be roughly connected with the transition from a disordered vortex lattice (vortex solid) to a vortex liquid state [166]. The peak temperature $T_{\rm peak}$ in Fig. 5.11a and the peak field $H_{\rm peak}$ in Fig. 5.11b give rise to an underestimate of H_{c2} [167]. Figure 5.11c presents a rough phase diagram of vortices, where the vortex liquid state is the region between lines of $T_{\rho=0}$ and $T_{\rm peak}$ ($H_{\rm peak}$). Based on this figure, our STM measurements with $T = 6$ K and 4 T $\leq H \leq$ 9 T are most likely in the vortex liquid state. The conjecture that we are above H_{c2} has

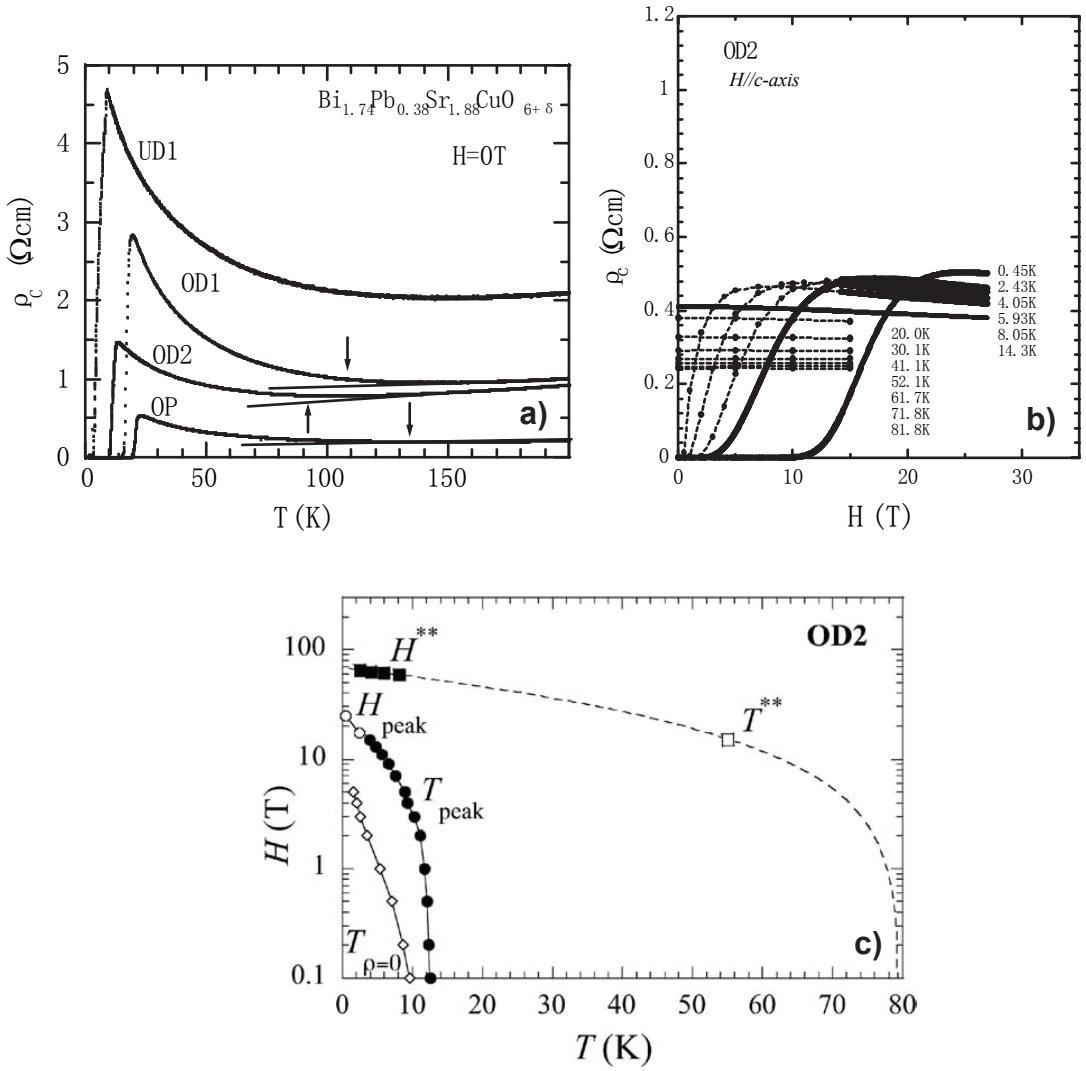

Figure 5.11: (a) Temperature dependence of ρ_c for $Bi_{1.74}Pb_{0.38}Sr_{1.88}CuO_{6+\delta}$ with different doping at zero field. Sample OD2 has a $T_c = 13$ K, which is closest to our Pb-Bi2201. (b) Magnetic field dependence of ρ_c for the sample OD2. (c) H-T phase diagram of OD2. All three figures are from Ref. [163].

to be rejected. In addition, the vortex density increases with H and the weight of N_0 in each dI/dV spectrum increases. As a result, the small superconducting gap becomes more pronounced as H increases. In App. A, we will give a detailed deriva-

tion based on simulated spectra. Our results in Fig. 5.10 are consistent with this prediction. However, to confirm the vortex liquid state conjecture, a larger phase space at different temperatures and magnetic fields are required to be explored in the future. Especially by lowering the temperature to approach a vortex solid state, we can clarify the division normalization results inside vortex cores.

5.5 Conclusion and Discussions

Following the division normalization method under magnetic fields, we extract a homogeneous hidden small gap coexisting with an apparent inhomogeneous gap. The hidden small gap we believe to be a superconducting order, which can be linked to a low-voltage shoulder in previous tunneling spectra [93]. Our results are consistent with those obtained by comparing spectra below and above T_c. We believe that the normal state in vortex cores is compatible with the pseudogap state above T_c. Although the pseudogap state was suspected to exist in vortex cores [168], it is the first time that we know of that a serious analysis has been made to verify this point. The fact that the penetrated magnetic field cannot suppress the pseudogap states limits different theories.

Although the two-gap scenario is confirmed in our STM measurements, further detailed studies, such as the doping dependence of the small superconducting gap, are required to flesh out the complementary picture. The underlying mechanism of the pseudogap is still unclear. Wise *et al.* [157] studied the relation between the checkerboard pattern in DOS maps of Bi-2201 and spectral inhomogeneity. It was proposed that the pseudogap state is a CDW order originating from the Fermi sur-

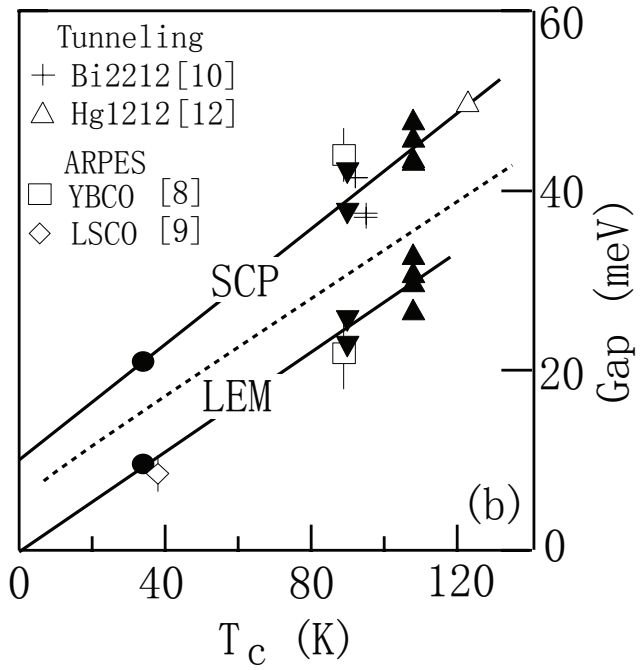

Figure 5.12: Two solid lines of superconducting gap sizes estimated by ARPES measurements: the superconducting peak position (SCP) and the leading-edge midpoint (LEM). These two lines are separated by the dashed line. The horizonal axis is the critical temperature T_c of various optimally doped cuprates. Cited from Ref. [169].

face nesting near the antinodal region. As discovered by several groups [100, 170, 93], the checkerboard pattern and the nesting CDW order are believed to coexist. However, the following controversies need to be resolved, to prove that the CDW order is the pseudogap order: 1) The pseudogap scales linearly with doping throughout the cuprate family and loses linear dependence of T_c. When comparing different systems at optimal doping, Feng *et al.* observed the antinodal gap scales linearly with T_c [169] (see Fig. 5.12). In other words, the pseudogap is not unrelated with the superconducting phase. 2) The CDW order cannot explain the angle dependent d-wave

feature of the pseudogap. Fermi surface nesting normally leads to a single value gap. 3) For underdoped cuprates, a series of experiments suggest that T_c is limited by the superfluid (superconducting carrier) density [171, 172, 148]. Feng *et al.* also interpreted weakening of antinodal coherence peaks of spectra upon underdoping using the decrease of superfluid density [158]. Whether the critical temperature depends on the superfluid density or the hidden small gap has to be reconciled for underdoped cuprates.

The Nernst state above T_c was proposed as a superconducting state with moving vortices, similar to the vortex liquid state. For the former state, vortices are thermally excited with opposite polarities as topological defects at zero field [173], whereas the latter state are often considered under magnetic fields. Our division normalization method under magnetic fields can be expected to detect the possible superconducting information in the Nernst state above T_c.

In the end, I briefly address the relation between our vortex liquid phase and recent results of quantum oscillation experiments[27, 28, 29]. Quantum oscillations are often associated with closed Fermi surface pockets. Recent quantum oscillation experiments on cuprate superconductors have revealed some electron pockets near the antinodal region and hole pockets near the nodal region of the Brillouin zone[27, 28, 29]. Some phenomenological theories have been proposed to reconcile the pseudogap phase above T_c at zero field and the observed quantum oscillations at high fields[174, 175]. It is worthwhile to emphasize that quantum oscillations can also occur in a regime where some vortex pinning prevails[29] and the persistence of Landau quantization in the mixed state of Type-II superconductors have been a

general phenomenon discussed earlier[176]. Although our experiments did not reach the high magnetic fields applied in quantum oscillation experiments, it is still possible that some Fermi surface information could be discovered.

Appendix A

Division Normalization in the Vortex Liquid State

In this appendix, I discuss the electronic density of states (DOS) for superconductors with two gap symmetries and derive the division normalization in the vortex liquid state. Some formulas have been presented in the main body of this thesis, but they are recollected here in an integrated manner.

In the BCS theory, the superconducting DOS in momentum space is given by

$$N_s(\varepsilon) = N_0 \; n_s(\varepsilon) = N_0 \frac{\varepsilon}{\sqrt{\varepsilon^2 - \Delta^2}}, \tag{A.1}$$

where N_0 is the normal state DOS, ε is the energy away from the Fermi energy, and Δ is the superconducting gap. For convenience, we introduce a reduced (dimensionless) superconducting DOS, $n_s(\varepsilon)$, to represent the superconducting gap information without the influence of N_0. To add scattering from pair-breaking sources, ε is replaced by $\varepsilon - i\Gamma$, where Γ denotes dissipation. For s-wave superconductors, N_s is rewritten

as

$$N_s(\varepsilon) = N_0 \ \mathrm{Re}\left[\frac{\varepsilon - i\Gamma}{\sqrt{(\varepsilon - i\Gamma)^2 - \Delta_0^2}}\right], \tag{A.2}$$

where N_0 is a constant, and Δ is angle-independent in momentum space, $\Delta = \Delta_0$. Rigorously, Eq. (A.2) is only valid when the energy is greater than the Fermi energy ($\varepsilon > 0$); with a mirror symmetry, the DOS for negative ε is directly given by $N_s(\varepsilon) = N_s(-\varepsilon)$. The same symmetry theoretically holds for all the DOS considered in this thesis.

For high-T_c superconductors, although the BCS theory is no longer valid, Eq. (A.1) can still phenomenologically describe the quasiparticle DOS N_s after modifications. For cuprates, the gap is anisotropic in momentum space. With a *d*-wave distribution, the gap becomes $\Delta(\theta) = \Delta_{SM} \cos 2\theta$, where θ represents the position along the Fermi surface as shown in Fig. 1.3, and Δ_{SM} is the maximum gap size on the antinodal point with $\theta = 0$ and $\pi/2$. Since STM is operated in real space, a STS spectrum is derived as an average over the Fermi surface in momentum space,

$$\overline{n}_s(\varepsilon) = \int n_s(\varepsilon, \theta) d\theta = \int \mathrm{Re}\left[\frac{\varepsilon - i\Gamma}{\sqrt{(\varepsilon - i\Gamma)^2 - (\Delta_{SM} \cos 2\theta)^2}}\right] d\theta, \tag{A.3}$$

where the normal state DOS N_0 is considered as a constant and omitted. A typical *d*-wave DOS spectrum is plotted in Fig. 2.4, and half the distance between two coherence peaks is used to approximate Δ_{SM} in practice. The assumption that the normal state N_0 is a constant is questionable for ceramic compounds. Although the explicit form of N_0 is unknown yet, it is possible to approximate N_0 by a pseudogap-like function due to their compatibility. For simplicity, we also assign a *d*-wave function to N_0,

$$N_0(\varepsilon, \theta) \approx N_0' \ \mathrm{Re}\left[\frac{\varepsilon - i\Gamma'}{\sqrt{(\varepsilon - i\Gamma')^2 - (\Delta_{PM} \cos 2\theta)^2}}\right], \tag{A.4}$$

where N_0' is a new constant coefficient in the unit of nS, and Δ_{PM} and Γ' denote the maximum gap and scattering dissipation for the pseudogap, respectively. As a result, the integrated dI/dV spectrum is given by

$$\overline{N}_s(\varepsilon) = \int N_s(\varepsilon,\theta)d\theta = \int N_0(\varepsilon,\theta)n_s(\varepsilon,\theta)d\theta, \tag{A.5}$$

which is the fundamental assumption of the two-gap scenario we apply in Chap. 5.

Pseudogaps Δ_{PM} and superconducting gaps Δ_{SM} are usually mixed with each other in STS spectra. In principle Eq. (A.5) can be used to fit spectra and evaluate Δ_{PM} and Δ_{SM}, but it is practically difficult due to many possible limitations such as spectrum asymmetry. Alternatively, we can apply the division normalization approach,

$$\overline{n}_s^{\mathrm{div}}(\varepsilon) = \frac{\overline{N}_s(\varepsilon)}{\overline{N}_0(\varepsilon)} = \frac{\int N_0(\varepsilon,\theta)n_s(\varepsilon,\theta)d\theta}{\int N_0(\varepsilon,\theta)d\theta}. \tag{A.6}$$

Although $\overline{n}_s^{\mathrm{div}}(\varepsilon)$ differs from the exact reduced superconducting DOS spectrum $\overline{n}_s(\varepsilon)$, Δ_{SM} evaluated from these two functions are almost the same demonstrated by the example in Fig. 5.6. Boyer *et al.* chose spectra above T_c to approximate $\overline{N}_0(\varepsilon)$[118]. Since an external magnetic field can lead to normal state vortices, we instead treat vortex spectra in nonzero fields at the same temperature as $\overline{N}_0(\varepsilon)$, which avoids thermal broadening. Notice that due to inhomogeneity of the DOS, spectra used in the division normalization have to be measured at the same spatial location.

Interestingly, vortices are not imaged in our experiments with conditions of $H =$ 4/6/9 T and $T = 6$ K for Pb-Bi2201 samples. We propose that the system is most possibly in the vortex liquid state by comparing the H-T phase diagram of vortices [163]. Vortices can move around in space, and a nonzero-field STS spectrum $\overline{N}_H(\varepsilon)$ taken in the time scale of ms includes both $\overline{N}_s(\varepsilon)$ and $\overline{N}_0(\varepsilon)$, which can be roughly written

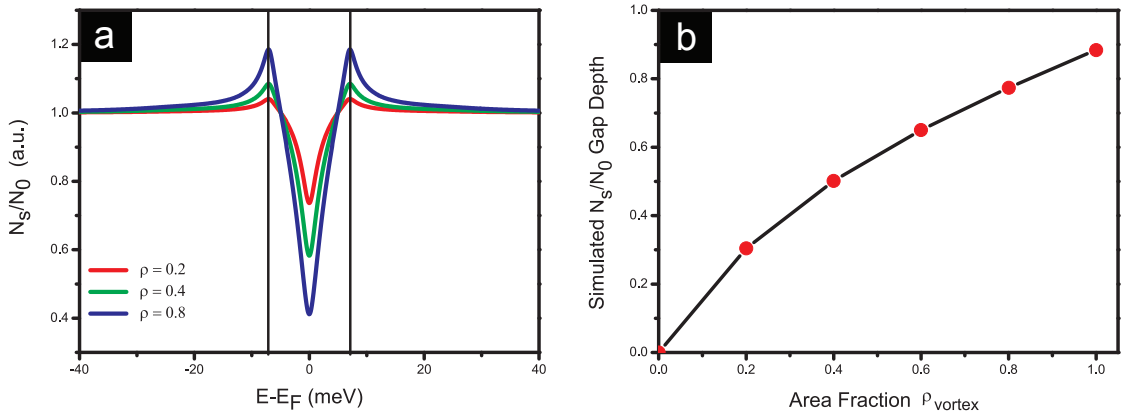

Figure A.1: (a) Simulated normalized spectra with different vortex area fractions ρ_{vortex} in the vortex liquid state. The same parameters as in Fig. 5.6 are chosen. A small gap ≈ 7 meV is presented for all normalized spectra, independent of ρ_{vortex}. (b) The gap depth (see text) vs. the vortex area fractions.

as an average form,

$$\overline{N}_H(\varepsilon) \approx x\overline{N}_0(\varepsilon) + (1-x)\overline{N}_s(\varepsilon). \tag{A.7}$$

Here the normal state weight x is approximately evaluated by the area fraction of vortices, ρ_{vortex}, which increases with field. Accordingly, the division normalization in our experiments is more properly given by

$$\overline{n}_H^{\text{div}}(\varepsilon) = \frac{\overline{N}_{H=0}(\varepsilon)}{\overline{N}_H(\varepsilon)} = \frac{\overline{N}_s(\varepsilon)}{x\overline{N}_0(\varepsilon) + (1-x)\overline{N}_s(\varepsilon)}. \tag{A.8}$$

In Fig. A.1a, we present simulated calculations of $\overline{n}_H^{\text{div}}(\varepsilon)$ for three different x with the same parameters used in Fig. 5.6. We observe that gap sizes extracted from three different spectra are exactly the same. The gap depth, defined as the vertical distance from the coherence peak to the zero-bias well bottom, increases with the vortex density. As shown in Fig. A.1b, the gap depth is a hyperbolic function of the ρ_{vortex}. In other words, the gap depth for a higher field is smaller than the expectation

by linearly fitting results of lower fields. It is important to notice that the conclusions of both gap size and gap depth from the above simulated calculations are impressively consistent with our experimental results presented in Chap. 5, further supporting the proposed vortex liquid state.

Appendix B

Differential Conductance Spectroscopy Routine

In the STS mode, a dI/dV spectrum measurement is optimally realized using a lock-in technique. The internal lock-in amplifier of a Nanonis STM controller is integrated in the dI/dV spectrum measurement. In this appendix, I present the spectroscopy routine and its timing diagram. Notice that the following steps are automatically executed by the Nanonis controller.

In Fig. B.1, a timing diagram of half cycle dI/dV spectroscopy displays the bias voltage versus time. A spectroscopy routine and the time parameters (typical values given in parenthesis) are explained below. The corresponding procedure numbers are correlated with either an execution time point or a range of time in the process.

1. Start the spectroscopy measurement. Lock-in is on; both ***Frequency*** (1.11 kHz) and zero-peak ***Amplitude*** (1.5 mV) are set. Tip stops on a spatial point and the feedback is still on.

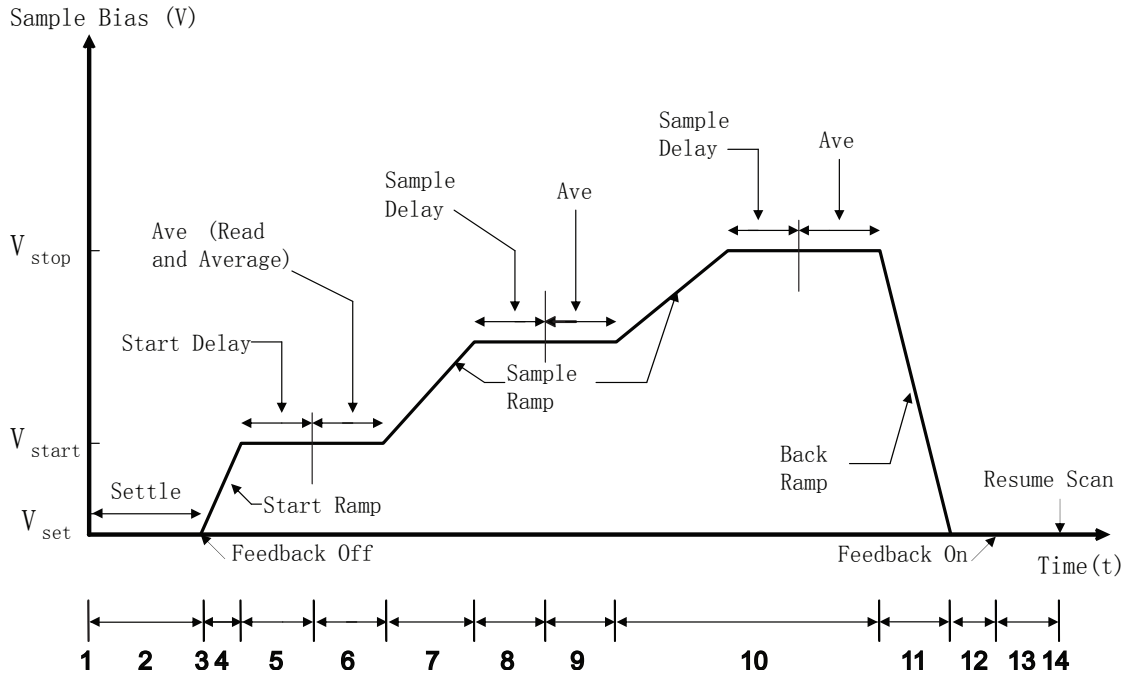

Figure B.1: Timing diagram for a half cycle dI/dV spectroscopy.

2. Wait for a short settle time, which is set by ***Z averaging time*** (50 ms). Within the settle time, feedback is on and the averaged z position (z_{aver}) is measured.

3. Stop the feedback and z voltage is set to z_{aver} (Z-controller hold mode).

4. Ramp the bias voltage to V_{start} with the start ramp speed set by ***Max. slew rate*** (10 V/s).

5. Wait for a while after the bias is ramped to the starting point of the bias range. The start delay time is equal to the addition of ***Initial setting time*** (5 ms) and ***Setting time*** (100 μs).

6. Acquire and average modulation current during the ***Integration time*** (10 ms) for this bias voltage.

7. Ramp to next bias level with the sample ramp speed set by *Max. slew rate*. The bias step size follows the division of $V_{\text{start}} - V_{\text{stop}}$ by the number of points.

8. Wait for a short time before the data acquisition. The sample delay time is equal to *Setting time*, which is often shorter than *Initial setting time* because a single bias step is often smaller than $V_{\text{start}} - V_{set}$.

9. Repeat step 6.

10. Repeat steps 7, 8, 6 in sequence until V_{stop} is reached.

11. For this half cycle routine, ramp bias voltage directly from V_{stop} back to V_{set}. The ramp speed is also set by *Max. slew rate*.

12. Wait for a short time with feedback off. The time is equal to the addition of *Setting time* and ***End setting time*** (5 ms).

13. The feedback is back on and the tip stays at the same spatial point for a while, set by ***Z control time*** (50 ms).

14. Stop the spectroscopy measurement. Move to the next position if the tip was scanning before the spectroscopy.

Appendix C

Schematic Diagrams of Electronics

In this appendix, schematic diagrams of three electronics are presented with their modules instead of design details. These electronics are designed and built by my colleagues. I have experienced the testing, modification and application processes. The information here may serve as an integrated reference for future students.

C.1 Walker Controller

The walker controller is designed and built by Dr. Kamalesh Chatterjee at MIT. It consists of one HV supply board, two ± 12 V DC supply boards and three functional electronic boards: amplifier board, delay board and drive board, as shown in the functional block diagram (see Fig. C.1). The walker controller accepts two analog signals from a control computer as input signals and outputs six driving signals to the step walker which consists of six shear piezo stacks. The waveform and trigger analog signals, shown schematically in Fig. C.2, are created using a NI DAQ board

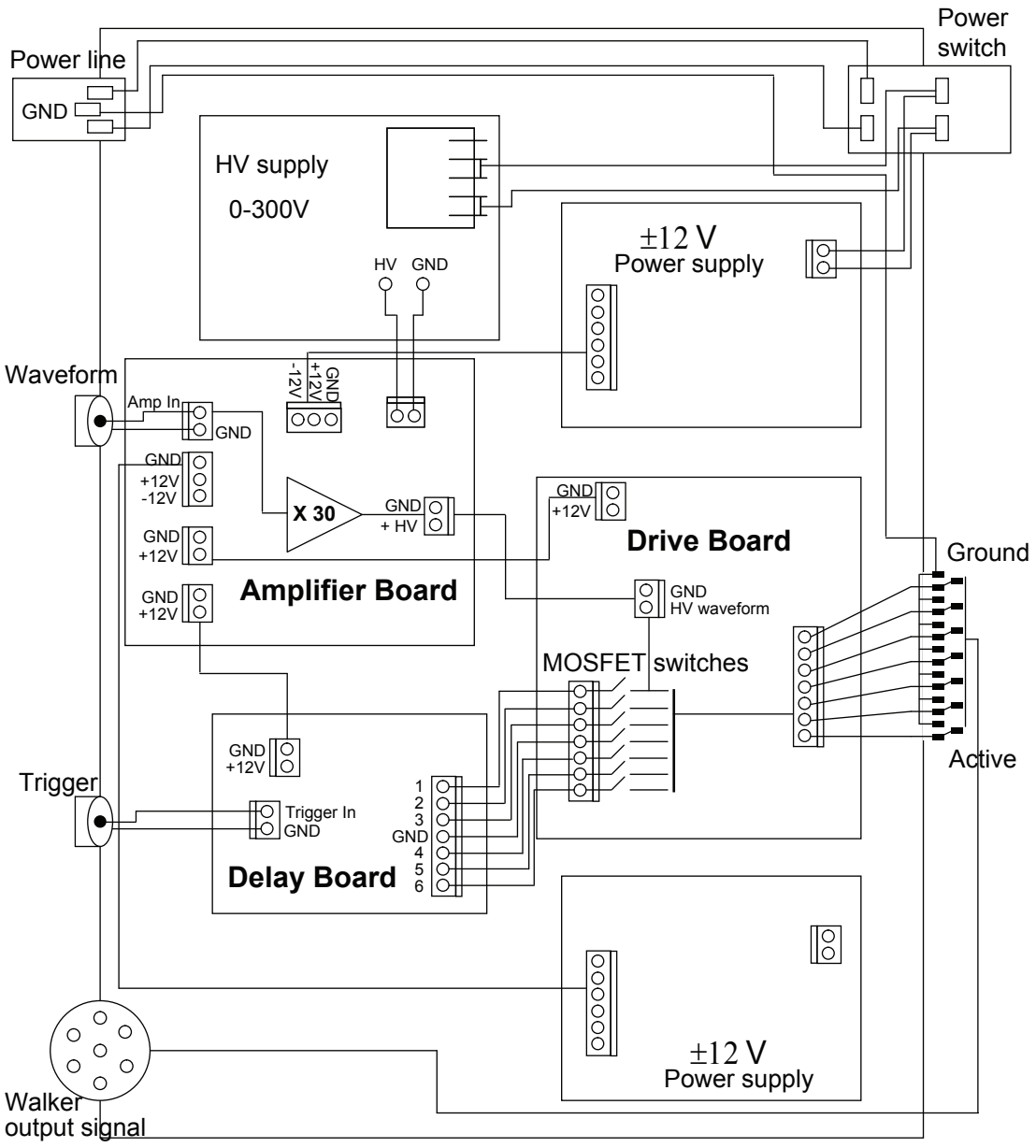

Figure C.1: Functional block diagram of the walker controller. Designed and built by Dr. Kamalesh Chatterjee at MIT.

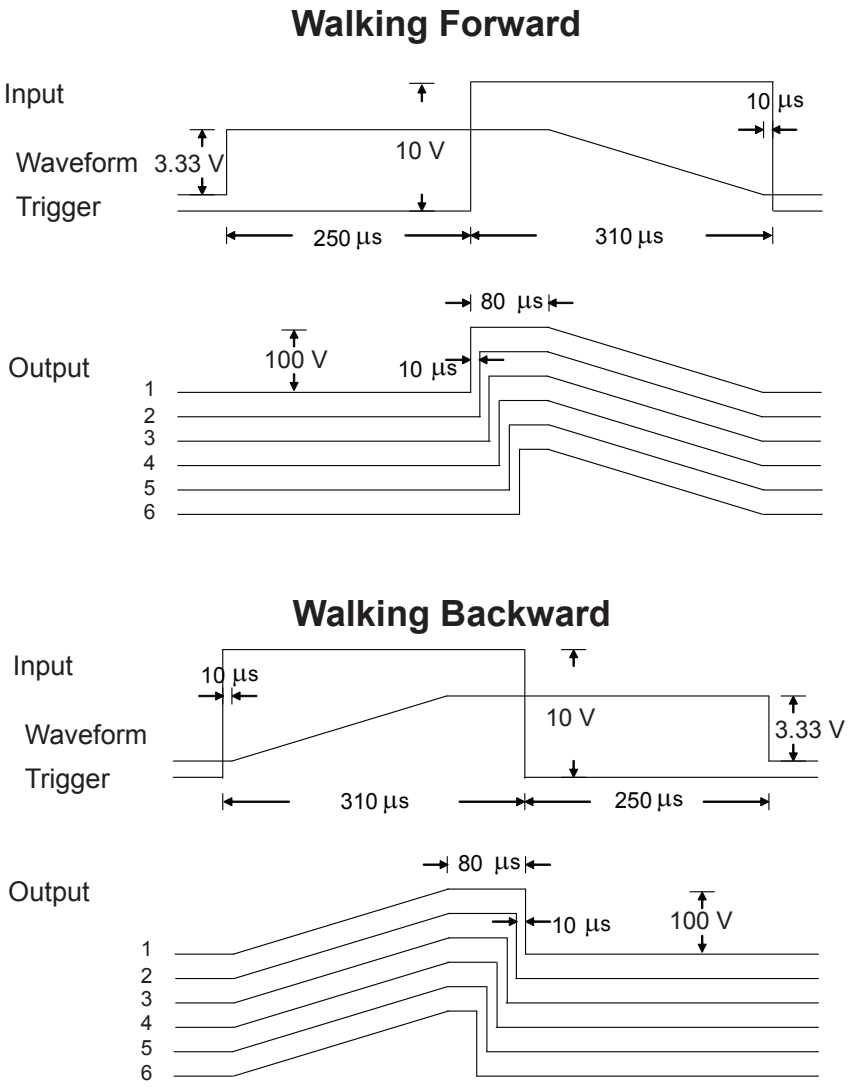

Figure C.2: Timing diagram for the input and output signals of the walker controller. Both forward and backward modes are presented. The walker controller accepts two analog signals, one waveform and one trigger, as inputs, and outputs six drive signals.

(PCI-6731) and Labview software. The working principles are referred to Chap. 3 for both forward and backward modes. As an example, we choose the output voltage as 100 V, which means that the input waveform for the walker controller has a 100/30

V amplitude. The proportion is from the ×30 amplifier board, shown in Fig. C.1. The time scales are close to our normal working conditions.

C.2 Capacitance Meter

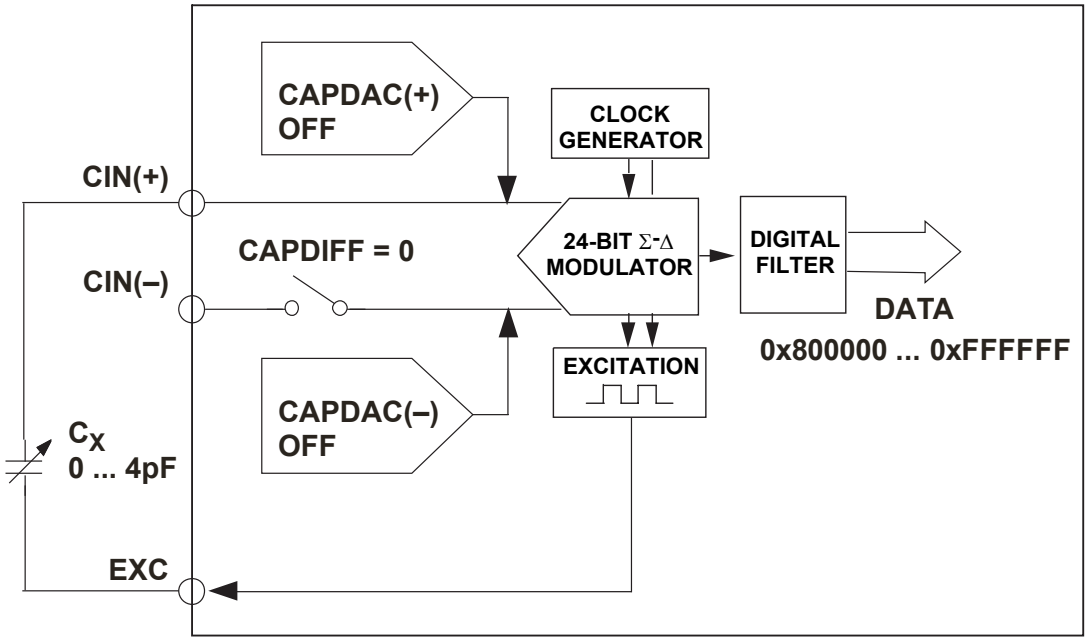

Figure C.3: Single-ended input mode of AD7746 in its simplified block diagram. Modified from AD7746 data sheet.

The capacitance meter is designed and built by Jim MacArthur at Harvard University. In our STM, the capacitance between two Cu concentric cylinders is monitored to check the relative tip-sample distance. Two semi-rigid coaxes, connected to the Cu cylinders, are guided out of the fridge and work as two inputs for the capaci-

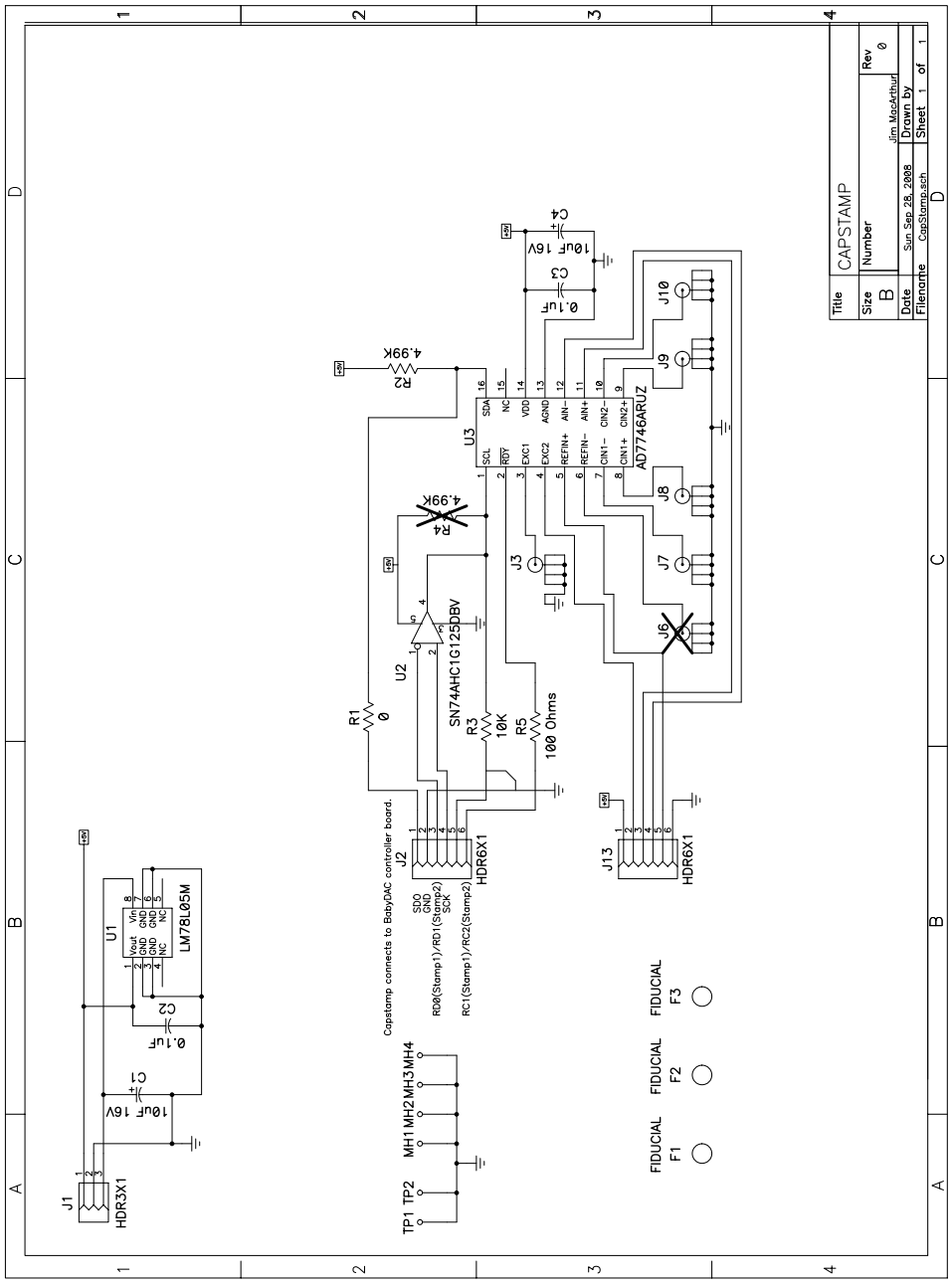

Figure C.4: Breakout board diagram for the Analog Devices 7746 capacitance sensor. Designed by Jim MacArthur at Harvard University.

tance meter. The capacitance meter is based on a single chip capacitance-to-digital converter Analog Devices 7746 (AD7746), whose block diagram is shown in Fig. C.3 (from AD7746 data sheet). The input range (±4.096 pF) of AD7746 is sufficient for our application. The chip operates with a single power supply $\sim$ 5 V. We have one channel of floating capacitive sensor, which is measured in the single-ended mode of AD7746 as shown in Fig. C.3. Two coaxes are directly connected to CIN1(+) and EXC1 pins. Detailed design of the breakout board for AD7746 is also presented in Fig. C.4. The control computer communicates with the capacitance meter with an asynchronous serial port. Both capacitance reading and changes of configuration register are realized through the serial port.

C.3 Field Emission High Voltage Source

In the field emission process to clean the STM tip, a high voltage source in the range of hundreds of volts is needed. Our field emission high voltage source is designed by P. Bonnefil at the University of California at Berkeley and built by Dr. Heonick Ha. The main functional parts of this bipolar voltage source are two Bertan PMT modular high voltage power supplies with regulated output up to 500 V. The output-current limit is modified to 200 μA. A schematic block diagram is shown in Fig. C.5.

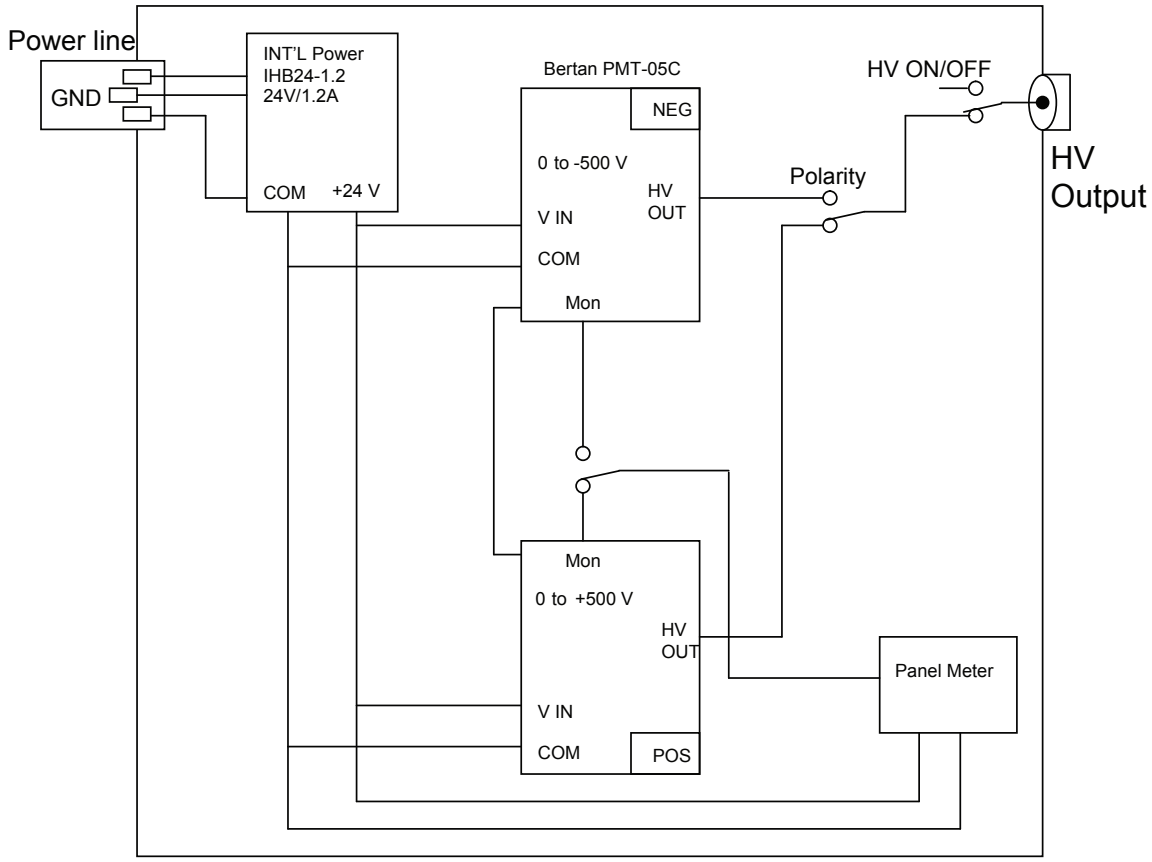

Figure C.5: Blocked diagram for the high voltage source for field emission. It is designed by P. Bonnefil at University of California at Berkeley and built by Dr. Heonick Ha.

Bibliography

[1] H. K. Onnes. On the sudden change in the rate at which the resistance of mercury disappers. *Commmun. Phys. Lab. Univ. Leiden*, 124c:1, 1911.

[2] W. Meissner and R. Ochsenfeld. Ein neuer effect bei eintritt der supraleitfähigkeit. *Naturwissenschaften*, 21:787, 1933.

[3] F. London and H. London. *Proc. R. Soc. London*, A149:71, 1935.

[4] V. L. Ginzburg and L. D. Landau. *Zh. Eksp. Thor. Fiz.*, 20:1064, 1950.

[5] J. Bardeen, L. N. Cooper, and J. R. Schrieffer. Theory of superconductivity. *Phys. Rev.*, 108:1175, 1957.

[6] J. R. Schrieffer. *Theory of superconductivity.* Perseus Books, Reading, MA, USA, revised printing edition, 1999.

[7] Eliashberg. *Zh. Eksp. Theo. Fiz.*, 38:966, 1960.

[8] E. Maxwell. Isotope effect in superconductivity of mercury. *Phys. Rev.*, 78:477, 1950.

[9] C. A. Reynolds, B. Serin, W. H. Wright, and L. B. Nesbitt. Superconductivity of isotopes of mercury. *Phys. Rev.*, 78:487, 1950.

[10] P. Dervenagas, M. Bullock, J. Zarestky, P. Canfield, B. K. Cho, B. Harmon, A. I. Goldman, and C. Stassis. Soft phonons in superconducting $LuNi_2B_2C$. *Phys. Rev. B*, 52:R9839, 1995.

[11] J. Bardeen, L. N. Cooper, and J. R. Schrieffer. Theory of superconductivity. *Phys. Rev.*, 108:1175, 1957.

[12] A. A. Abrikosov and L. P. Gor'kov. *Zh. Eksperim. i Teor. Fiz.*, 39:1781, 1960.

[13] A. A. Abrikosov and L. P. Gor'kov. *Soviet Phys. -JETP*, 12:1243, 1961.

[14] S. M. Girvin. Just what is superconductivity. *Nat. Phys.*, 1:83, 1995.

[15] J. G. Bednorz and K. A. Müller. Possible high T_c superconductivity in the Ba-La-Cu-O system. *Z. Phys. B*, 64(2):189, 1986.

[16] L. Gao, Y. Y. Xue, F. Chen, Q. Xiong, R. L. Meng, D. Ramirez, , C. W. Chu, J. H. Eggert, and H. K. Mao. Superconductivity up to 164 K in $HgBa_2Ca_{m-1}Cu_mO_{2m+2+\delta}$ ($m = 1$, 2, and 3) under quasihydrostatic pressures. *Phys. Rev. B*, 50:4260, 1994.

[17] Z. X. Shen, D. S. Dessau, B. O. Wells, D. M. King, W. E. Spicer, A. J. Arko, D. Marshall, L. W. Lombardo, A. Kapitulnik, P. Dickinson, S. Doniach, J. DiCarlo, T. Loeser, and C. H. Park. Anomalously large gap anisotropy in the a-b plane of $Bi_2Sr_2CaCu_2O_{8+\delta}$. *Phys. Rev. Lett.*, 70:1553, 1993.

[18] H. Ding, M. R. Norman, J. C. Campuzano, M. Randeria, A. F. Bellman, T. Yokoya, T. Takahashi, T. Mochiku, and K. Kadowaki. Angle-resolved photoemission spectroscopy study of the superconducting gap anisotropy in $Bi_2Sr_2CaCu_2O_{8+x}$. *Phys. Rev. B*, 54:R9678, 1996.

[19] D. A. Wollman, D. J. Van Harlingen, W. C. Lee, D. M. Ginsberg, and A. J. Leggett. Experimental determination of the superconducting pairing state in YBCO from the phase coherence of YBCO-Pb dc SQUIDs. *Phys. Rev. Lett.*, 71:2134, 1993.

[20] C. C. Tsuei, J. R. Kirtley, C. C. Chi, L. S. Yu-Jahnes, A. Gupta, T. Shaw, J. Z. Sun, and M. B. Ketchen. Pairing symmetry and flux quantization in a tricrystal superconducting ring of $YBa_2Cu_3O_{7-\delta}$. *Phys. Rev. Lett.*, 73:593, 1994.

[21] Y. Maeno, H. Hashimoto, K. Yoshida, S. Nishizaki, T. Fujita, J. G. Bednorz, and F. Lichtenberg. Superconductivity in a layered perovskite without copper. *Nature*, 372:532, 1994.

[22] H. Maeda, Y. Tanaka, M. Fukutomi, and T. Asano. A new high-T_c oxide superconductor without a rare-earth element. *Jap. J. Appl. Phys.*, 27:L209, 1988.

[23] M. K. Wu, J. R. Ashburn, C. J. Torng, P. H. Hor, R. L. Meng, L. Gao, Z. J. Huang, Y. Q. Wang, and C. W. Chu. Superconductivity at 93 K in a new mixed-phase Y-Ba-Cu-O compound system at ambient pressure. *Phys. Rev. Lett.*, 58:908, 1987.

[24] F. C. Zhang and T. M. Rice. Effective hamiltonian for the superconducting Cu oxides. *Phys. Rev. B*, 37:3759, 1988.

[25] P. W. Anderson. The resonating valence bond state in La_2CuO_4 and superconductivity. *Science*, 235:1196, 1987.

[26] P. A. Lee, N. Nagaosa, and X. G. Wen. Doping a mott insulator: physics of high-temperature superconductivity. *Rev. Mod. Phys.*, 78:17, 2006.

[27] N. Doiron-Leyraud, C. Proust, D. LeBoeuf, J. Levallois, J. B. Bonnemaison, R. X. Liang, D. A. Bonn, W. N. Hardy, and L. Taillefer. Quantum oscillations and the Fermi surface in an underdoped high-Tc superconductor. *Nature*, 447: 565, 2007.

[28] D. LeBoeuf, N. Doiron-Leyraud, J. Levallois, R. Daou, J. B. Bonnemaison, N. E. Hussey, L. Balicas, B. J. Ramshaw, R. X. Liang, D. A. Bonn, W. N. Hardy, S. Adachi, C. Proust, and L. Taillefer. Electron pockets in the Fermi surface of hole-doped high-Tc superconductors. *Nature*, 450:533, 2007.

[29] S. E. Sebastian, N. Harrison, E. Palm, T. P. Murphy, C. H. Mielke, R. X. Liang, D. A. Bonn, W. N. Hardy, and G. G. Lonzarich. A multi-component Fermi surface in the vortex state of an underdoped high-Tc superconductor. *Nature*, 454:200, 2008.

[30] B. Vignolle, A. Carrington, R. A. Cooper, M. M. J. French, A. P. Mackenzie, C. Jaudet, D. Vignolles, C. Proust, and N. E. Hussey. Quantum oscillations in an overdoped high-Tc superconductor. *Nature*, 455:952, 2008.

[31] J. Q. Meng, G. D. Liu, W. T. Zhang, L. Zhao, H. Y. Liu, X. W. Jia, D. X. Mu, S. Y. Liu, X. L. Dong, W. Lu, G. L. Wang, Y. Zhou, Y. Z., X. Y. Wang, Z. Y. Xu, C. T. Chen, and X. J. Zhou. Direct observation of Fermi pocket in high temperature cuprate superconductors, 2009. arXiv:0906.2682.

[32] K. Y. Yang, T. M. Rice, and F. C. Zhang. Phenomenological theory of the pseudogap state. *Phys. Rev. B*, 73:174501, 2006.

[33] W. Buckel and R. Kleiner. *Superconductivity*. Wiley-VCH, 2nd edition, 2004.

[34] V. J. Emery and S. A. Kivelson. Importance of phase fluctuations in superconductors with small superfluid density. *Nature*, 374:434, 1995.

[35] Y. Kamihara, T. Watanabe, M. Hirano, and H. Hosono. Chemical bonding and electronic and magnetic structure in LaOFeAs. *J. Am. Chem. Soc.*, 130:3296, 2008.

[36] H. Takahashi, K. Igawa, K. Arii, Y. Kamihara, M. Hirano, and H. Hosono. Superconductivity at 43 K in an iron-based layered compound $LaO_{1-x}F_xFeAs$. *Nature*, 453:376, 2008.

[37] X. H. Chen, T. Wu, G. Wu, R. H. Liu, H. Chen, and D. F. Fang. Superconductivity at 43 K in $SmFeAsO_{1-x}F_x$. *Nature*, 453:761, 2008.

[38] G. F. Chen, Z. Li, D. Wu, G. Li, W. Z. Hu, J. Dong, P. Zheng, J. L. Luo, and N. L. Wang. Superconductivity at 41 K and its competition with spin-density-wave instability in layered $CeO_{1-x}F_xFeAs$. *Phys. Rev. Lett.*, 100:247002, 2008.

[39] Z. A. Ren, G. C. Che, X. L. Dong, J. Yang, W. Lu, W. Yi, X. L. Shen, Z. C. Li, L. L. Sun, F. Zhou, and Z. X. Zhao. Superconductivity and phase diagram in iron-based arsenic-oxides $ReFeAsO_{1-\delta}$ (Re = rare-earth metal) without fluorine doping. *Europhys. Lett.*, 83:17002, 2008.

[40] H. H. Wen, G. Mu, L. Fang, H. Yang, and X. Y. Zhu. Superconductivity at 25 K in hole-doped $(La_{1-x}Sr_x)OFeAs$. *Europhys. Lett.*, 82:17009, 2008.

[41] C. Wang, L. J. Li, S. Chi, Z. W. Zhu, Z. Ren, Y. K. Li, Y. T. Wang, X. Lin, Y. K. Luo, S. Jiang, X. F. Xu, G. H. Cao, and Z. A. Xu. Thorium-dopingcinduced superconductivity up to 56 K in $Gd_{1-x}Th_xFeAsO$. *Europhys. Lett.*, 83:67006, 2008.

[42] M. Rotter, M. Tegel, and D. Johrendt. Superconductivity at 38 K in the iron arsenide $(Ba_{1-x}K_x)Fe_2As_2$. *Phys. Rev. Lett.*, 101:107006, 2008.

[43] N. Ni, S. L. Bud'ko, A. Kreyssig, S. Nandi, G. E. Rustan, A. I. Goldman, S. Gupta, J. D. Corbett, A. Kracher, and P. C. Canfield. Anisotropic thermodynamic and transport properties of single-crystalline $Ba_{1-x}K_xFe_2As_2$ ($x = 0$ and 0.45). *Phys. Rev. B*, 78:014507, 2008.

[44] K. Sasmal, B. Lv, B. Lorenz, A. M. Guloy, F. Chen, Y. Y. Xue, and C. W. Chu. Superconducting Fe-based compounds $(A_{1-x}Sr_x)Fe_2As_2$ with A=K and Cs with transition temperatures up to 37 K. *Phys. Rev. Lett.*, 101:107007, 2008.

[45] G. F. Chen, Z. Li, G. Li, W. Z. Hu, J. Dong, J. Zhou, X. D. Zhang, P. Zheng,

N. L. Wang, and J. L. Luo. Superconductivity in hole-doped $(Sr_{1-x}K_x)Fe_2As_2$. *Chin. Phys. Lett.*, 25:3403, 2008.

[46] F. Ronning, T. Klimczuk, E. D. Bauer, H. Volz, and J. D. Thompson. Synthesis and properties of $CaFe_2As_2$ single crystals. *J. Phys.: Condens. Matter*, 20: 322201, 2008.

[47] T. Park, E. Park, H. Lee, T. Klimczuk, E. D. Bauer, F. Ronning, and J. D. Thompson. Pressure-induced superconductivity in $CaFe_2As_2$. *J. Phys.: Condens. Matter*, 20:322204, 2008.

[48] G. Wu, H. Chen, T. Wu, Y. L. Xie, Y. J. Yan, R. H. Liu, X. F. Wang, J. J. Ying, and X. H. Chen. Different resistivity response to spin-density wave and superconductivity at 20 K in $Ca_{1-x}Na_xFe_2As_2$. *J. Phys.: Condens. Matter*, 20: 422201, 2008.

[49] N. Ni, S. Nandi, A. Kreyssig, A. I. Goldman, E. D. Mun, S. L. Bud'ko, and P. C. Canfield. First-order structural phase transition in $CaFe_2As_2$. *Phys. Rev. B*, 78:014523, 2008.

[50] M. S. Torikachvili, S. L. Bud'ko, N. Ni, and P. C. Canfield. Pressure induced superconductivity in $CaFe_2As_2$. *Phys. Rev. Lett.*, 101:057006, 2008.

[51] H. S. Jeevan, Z. Hossain, D. Kasinathan, H. Rosner, C. Geibel, and P. Gegenwart. High-temperature superconductivity in $Eu_{0.5}K_{0.5}Fe_2As_2$. *Phys. Rev. B*, 78:092406, 2008.

[52] X. C. Wang, Q .Q. Liu, Y. X. Lv, W. B. Gao, L. X. Yang, R. C. Yu, F. Y. Li,

and C. Q. Jin. The superconductivity at 18 K in LiFeAs system. *Solid State Commun.*, 148:538, 2008.

[53] M. J. Pitcher, D. R. Parker, P. Adamson, S. J. C. Herkelrath, A. T. Boothroyd, R. M. Ibberson, M. Brunelli, and Clarke. S. J. Structure and superconductivity of LiFeAs. *Chem. Commun.*, 2008:5918, 2008.

[54] J. H. Tapp, Z. J. Tang, B. Lv, K. Sasmal, B. Lorenz, P.C.W. Chu, and A. M. Guloy. LiFeAs: an intrinsic FeAs-based superconductor with $T_c = 18$ K. *Phys. Rev. B.*, 78:060505, 2008.

[55] F. C. Hsu, J. U. Luo, K. W. Yeh, T. W. Huang, P. M. Wu, Y. C. Lee, Y. L. Huang, Y. Y. Chu, D. C. Yan, and M. K Wu. Superconductivity in the PbO-type structure α-FeSe. *Proc. Natl. Acad. Sci. (USA)*, 105:14262, 2008.

[56] Y. Mizuguchi, F. Tomioka, S. Tsuda, T. Yamaguchi, and Y. Takano. Superconductivity at 27 K in tetragonal FeSe under high pressure. *Appl. Phys. Lett*, 93:152505, 2008.

[57] D. J. Singh and M. H. Du. Density functional study of $LaFeAsO_{1-x}F_x$: a low carrier density superconductor near itinerant magnetism. *Phys. Rev. Lett.*, 100: 237003, 2008.

[58] D.J. Singh. Electronic structure of Fe-based superconductors. *Physica C*, 469: 418, 2008.

[59] D. H. Lu, M. Yi, S. K. Mo, A. S. Erickson, J. Analytis, J. H. Chu, D. J. Singh,

Z. Hussain, T. H. Geballe, I. R. Fisher, and Z. X. Shen. Electronic structure of the iron-based superconductor LaOFeP. *Nature*, 455:81, 2008.

[60] T. Kondo, A. F. Santander-Syro, O. Copie, C. Liu, M. E. Tillman, E. D. Mun, J. Schmalian, S. L. Bud'ko, M. A. Tanatar, P. C. Canfield, , and A. Kaminski. Momentum dependence of the superconducting gap in $NdFeAsO_{0.9}F_{0.1}$ single crystals measured by angle resolved photoemission spectroscopy. *Phys. Rev. Lett.*, 101:147003, 2008.

[61] V. B. Zabolotnyy, D. S. Inosov, D. V. Evtushinsky, A. Koitzsch1, A. A. Kordyuk, G. L. Sun, J. T. Park, D. Haug, V. Hinkov, A. V. Boris, C. T. Lin, M. Knupfer, A. N. Yaresko, B. Büchner, A. Varykhalov, R. Follath, and S. V. Borisenko. (π, π) electronic order in iron arsenide superconductors. *Nature*, 457:569, 2008.

[62] H. Ding, P. Richard, K. Nakayama, K. Sugawara, T. Arakane, Y. Sekiba, A. Takayama, S. Souma, T. Sato, T. Takahashi, Z. Wang, X. Dai, Z. Fang, G. F. Chen, J. L. Luo, and N. L. Wang. Observation of Fermi-surface-dependent nodeless superconducting gaps in $Ba_{0.6}K_{0.4}Fe_2As_2$. *Europhys. Lett.*, 83:47001, 2008.

[63] S. E. Sebastian, J. Gillett, N. Harrison, P. H. C. Lau, D. J. Singh, C. H. Mielke, and G. G. Lonzarich. Quantum oscillations in the parent magnetic phase of an iron arsenide high temperature superconductor. *J. Phys.: Condens. Matter*, 20:422203, 2008.

[64] A. I. Coldea, J. D. Fletcher, A. Carrington, J. G. Analytis, A. F. Bangura, J. H.

Chu, A. S. Erickson, I. R. Fisher, N. E. Hussey, and R. D. McDonald. Fermi surface of superconducting LaFePO determined from quantum oscillations. *Phys. Rev. Lett.*, 101:216402, 2008.

[65] C. Liu, G. D. Samolyuk, Y. Lee, N. Ni, T. Kondo, A. F. Santander-Syro, S. L. Bud'ko, J. L. McChesney, E. Rotenberg, Valla. T, A. V. Fedorov, P. C. Canfield, B. N. Harmon, and A. Kaminski. K-doping dependence of the Fermi surface of the iron-arsenic $Ba_{1-x}K_xFe_2As_2$ superconductor using angle-resolved photoemission spectroscopy. *Phys. Rev. Lett.*, 101:177005, 2008.

[66] C. de la Cruz, Q. Huang, J. W. Lynn, J. Y. Li, W. Ratcliff II, J. L. Zarestky, H. A. Mook, G. F. Chen, J. L. Luo, N. L. Wang, and P. C. Dai. Magnetic order close to superconductivity in the iron-based layered $LaO_{1-x}F_xFeAs$ systems. *Nature*, 453:899, 2008.

[67] I. I. Mazin, D. J. Singh, M. D. Johannes, and M. H. Du. Unconventional superconductivity with a sign reversal in the order parameter of $LaFeAsO_{1-x}F_x$. *Phys. Rev. Lett.*, 101:057003, 2008.

[68] C. T. Chen, C. C. Tsuei, M. B. Ketchen, Z. A. Ren, and Z. X. Zhao. Integer and half-integer flux-quantum transitions in a niobium/iron-pnictide loop, 2009. arXiv:0905.3571.

[69] J. Bardeen. Tunneling from a many-particle point of view. *Phys. Rev. Lett.*, 6: 57, 1961.

[70] Ø. Fischer, M. Kugler, I. Maggio-Aprile, C. Berthod, and C. Renner. Scanning

tunneling spectroscopy of high-temperature superconductors. *Rev. Mod. Phys.*, 79(1):353, 2007.

[71] I. Giaever. Energy gap in superconductors measured by electron tunneling. *Phys. Rev. Lett.*, 5:147, 1960.

[72] I. Giaever. Electron tunneling and superconductivity. *Rev. Mod. Phys.*, 46:245, 1974.

[73] Michael Tinkham. *Introduction to superconductivity.* McGraw-Hill, New York, 2nd edition, 1996.

[74] R. D. Young. Surface microtopography. *Physics Today*, 24:42, 1971.

[75] G. Binnig, H. Rohrer, C. Gerber, and E. Weibel. Surface studies by scanning tunneling microscopy. *Phys. Rev. Lett.*, 49:5761, 1982.

[76] J. Tersoff and D. R. Hamann. Theory and application for the scanning tunneling microscope. *Phys. Rev. Lett.*, 50:1998, 1983.

[77] J. Tersoff and D. R. Hamann. Theory of the scanning tunneling microscope. *Phys. Rev. B*, 31:805, 1985.

[78] M. D. Kirk, J. Nogami, A. A. Baski, D. B. Mitzi, A. Kapitulnik, T. H. Geballe, and C. F. Quate. The origin of the superstructure in $Bi_2Sr_2CaCu_2O_{8+\delta}$ as revealed by scanning tunneling microscopy. *Science*, 242:1673, 1988.

[79] J. A. Slezak, J. Lee, M. Wang, K. McElroy, K. Fujita, B. M. Anderson, P. J. Hirschfeld, H. Eisaki, S. Uchida, and J. C. Davis. Imaging the impact on cuprate

superconductivity of varying the interatomic distances within individual crystal unit cells. *Proc. Natl Acad. Sci. (USA)*, 105:3203, 2008.

[80] X. L. Wu, Z. Zhang, Y. L. Wang, and C. M. Lieber. Structural and electronic role of lead in $(PbBi)_2Sr_2CaCu_2O_8$ superconductors by STM. *Science*, 248:1211, 1990.

[81] H. F. Hess, R. B Robinson, and J. V. Waszczak. STM spectroscopy of vortex cores and the flux lattice. *Physica B*, 169:422, 1991.

[82] S. H. Pan, E. W. Hudson, A. K. Gupta, K. W. Ng, H. Eisaki, S. Uchida, and J. C. Davis. STM studies of the electronic structure of vortex cores in $Bi_2Sr_2CaCu_2O_{8+\delta}$. *Phys. Rev. Lett.*, 85:1536, 2000.

[83] S. H. Pan, E. W. Hudson, K. M. Lang, H. Eisaki, S. Uchida, and J. C. Davis. Imaging the effects of individual zinc impurity atoms on superconductivity in $Bi_2Sr_2CaCu_2O_{8+\delta}$. *Nature*, 403:746, 2000.

[84] S. H. Pan, E. W. Hudson, and J. C. Davis. 3He refrigerator based very low temperature scanning tunneling microscope. *Rev. Sci. Instrum.*, 70:1459, 1999.

[85] C. J. Chen. *Introduction to scanning tunneling microscopy*. Oxford University Press, Inc., New York, 1st edition, 1993.

[86] Y. Yin, M. Zech, T. L. Williams, X. F. Wang, G. Wu, X. H. Chen, and J. E. Hoffman. Scanning tunneling spectroscopy and vortex imaging in the iron pnictide superconductor $BaFe_{1.8}Co_{0.2}As_2$. *Phys. Rev. Lett.*, 102:097002, 2009.

[87] X. F. Wang, T. Wu, G. Wu, H. Chen, Y. L. Xie, J. J. Ying, Y. J. Yan, R. H. Liu, and X. H. Chen. Anisotropy in the electrical resistivity and susceptibility of superconducting $BaFe_2As_2$ single crystals. *Phys. Rev. Lett.*, 102:117005, 2009.

[88] N. D. Zhigadlo, S. Katrych, Z. Bukowski, S. Weyeneth, R. Puzniak, and J. Karpinski. Single crystals of superconducting $SmFeAsO_{1-x}F_y$ by grown at high pressure. *J. Phys.: Condens. Matter*, 20:342202, 2008.

[89] R. Prozorov, M. E. Tillman, E. D. Mun, and P. C. Canfield. Intrinsic magnetic properties of the superconductor $NdFeAsO_{0.9}F_{0.1}$ from local and global measurements. *New J. Phys.*, 11:035004, 2009.

[90] Y. Yin, M. Zech, T. L. Williams, and J. E. Hoffman. Scanning tunneling microscopy and spectroscopy on iron-pnictides. *Physica C*, 469:535, 2009.

[91] S. H. Pan, J. P. O'Neal, R. L. Badzey, C. Chamon, H. Ding, J. R. Engelbrecht, Z. Wang, H. Eisaki, S. Uchida, A. K. Gupta, K. W. Ng, E. W. Hudson, K. M. Lang, and J. C. Davis. Microscopic electronic inhomogeneity in the high-tc superconductor $Bi_2Sr_2CaCu_2O_{8+\delta}$. *Nature*, 413:282, 2001.

[92] K. M. Lang, V. Madhavan, J. E. Hoffman, E. W. Hudson, H. Eisaki, S. Uchida, and J. C. Davis. Imaging the granular structure of high-T_c superconductivity in underdoped $Bi_2Sr_2CaCu_2O_{8+\delta}$. *Nature*, 415:412, 2002.

[93] K. McElroy, D. H. Lee, J. E. Hoffman, K. M. Lang, J. Lee, E. W. Hudson, H. Eisaki, S. Uchida, and J. C. Davis. Coincidence of checkerboard charge

order and antinodal state decoherence in strongly underdoped superconducting $Bi_2Sr_2CaCu_2O_{8+\delta}$. *Phys. Rev. Lett.*, 94:197005, 2005.

[94] K. K. Gomes, A. N. Pasupathy, A. Pushp, S. Ono, Y. Ando, and A. Yazdani. Visualizing pair formation on the atomic scale in the high-T_c superconductor $Bi_2Sr_2CaCu_2O_{8+\delta}$. *Nature*, 447:567, 2007.

[95] E. W. Hudson, K. M. Lang, V. Madhavan, S. H. Pan, H. Eisaki, S. Uchida, and J. C. Davis. Interplay of magnetism and high-tc superconductivity at individual magnetic impurity atoms in $Bi_2Sr_2CaCu_2O_{8+\delta}$. *Nature*, 411:920, 2001.

[96] K. Chatterjee, M. C. Boyer, W. D. Wise, T. Kondo, T. Takeuchi, H. Ikuta, and E. W. Hudson. Visualization of the interplay between high-temperature superconductivity, the pseudogap and impurity resonances. *Nat. Phys.*, 4:108, 2008.

[97] I. Maggio-Aprile, Ch. Renner, A. Erb, E. Walker, and Ø. Fischer. Direct vortex lattice imaging and tunneling spectroscopy of flux lines on $YBa_2Cu_3O_{7-\delta}$. *Phys. Rev. Lett.*, 75:2754, 1995.

[98] Ch. Renner, B. Revaz, J. Y. Genoud, K. Kadowaki, and Ø. Fischer. Pseudogap precursor of the superconducting gap in under- and overdoped $Bi_2Sr_2CaCu_2O_{8+\delta}$. *Phys. Rev. Lett.*, 80:149, 1998.

[99] B. W. Hoogenboom, K. Kadowaki, B. Revaz, M. Li, Ch. Renner, and Ø. Fischer. Linear and field-independent relation between vortex core state energy and gap in $Bi_2Sr_2CaCu_2O_{8+\delta}$. *Phys. Rev. Lett.*, 87:267001, 2001.

[100] J. E. Hoffman, E. W. Hudson, K. M. Lang, V. Madhavan, H. Eisaki, S. Uchida, and J. C. Davis. A four unit cell periodic pattern of quasi-particle states surrounding vortex cores in $Bi_2Sr_2CaCu_2O_{8+\delta}$. *Science*, 295:466, 2002.

[101] A. S. Sefat, R. Y. Jin, M. A. McGuire, B. C. Sales, D. J. Singh, and D. Mandrus. Superconductivity at 22 K in co-doped $BaFe_2As_2$ crystals. *Phys. Rev. Lett.*, 101: 117004, 2008.

[102] L. J. Li, Q. B. Wang, Y. K. Luo, H. Chen, Q. Tao, Y. K. Li, X. Lin, M. He, Z. W. Zhu, G. H. Cao, and Z. A. Xu. Superconductivity induced by ni doping in $BaFe_2As_2$. *New J. Phys.*, 11:025008, 2009.

[103] J. M. Tarascon, L. H. Greene, P. Barboux, W. R. McKinnon, G. W. Hull, T. P. Orlando, K. A. Delin, S. Foner, and E. J. McNiff. 3d-metal doping of the high-temperature superconducting perovskites La-Sr-Cu-O and Y-Ba-Cu-O. *Phys. Rev. B*, 36:8393, 1987.

[104] D. J. Derro, E. W. Hudson, K. M. Lang, S. H. Pan, J. C. Davis, J. T. Markert, and A. L. de Lozanne. Nanoscale one-dimensional scattering resonances in the CuO chains of $YBa_2Cu_3O_{6+x}$. *Phys. Rev. Lett.*, 88:097002, 2002.

[105] Q. Huang, Y. Qiu, Wei Bao, M. A. Green, J. W. Lynn, Y. C. Gasparovic, T. Wu, G. Wu, and X. H. Chen. Neutron-diffraction measurements of magnetic order and a structural transition in the parent $BaFe_2As_2$ compound of FeAs-based high-temperature superconductors. *Phys. Rev. Lett.*, 101:257003, 2008.

[106] I. R. Shein and A. L. Ivanovskii. Electronic structure of oxygen-free 38 k super-

conductor $Ba_{1-x}K_xFe_2As_2$ in comparison with $BaFe_2As_2$ from first principles, 2008. arXiv:0806.0750.

[107] J. C. Wojdel, I. D. R. Moreira, and F. Illas. Chemical bonding and electronic and magnetic structure in LaOFeAs. *J. Am. Chem. Soc.*, 131:906, 2009.

[108] M.A. Hossain, J.D.F. Mottershead, D. Fournier, A. Bostwick, J. L. McChesney, E. Rotenberg, R. Liang, W. N. Hardy, G. A. Sawatzky, I.S. Elfimov, D. A. Bonn, and A. Damascelli. In situ doping control of the surface of high-temperature superconductors. *Nat. Phys.*, 4:527, 2008.

[109] R. Hesper, L. H. Tjeng, A. Heeres, and G. A. Sawatzky. Photoemission evidence of electronic stabilization of polar surfaces in K_3C_{60}. *Phys. Rev. B*, 62:16046, 2000.

[110] S. de Jong, Y. Huang, R. Huisman, F. Massee, S. Thirupathaiah, M. Gorgoi, R. Follath, J. B. Goedkoop, and M. S. Golden. A high resolution, hard X-ray photoemission investigation of $BaFe_2As_2$: moderate influence of the surface and evidence for a low degree of Fe $3d$-As $4p$ hybridization of the near-E_F electronic states. *Phys. Rev. B*, 79:115125, 2009.

[111] 2009. M. Yi, L.H. Lu, private communication.

[112] M. C. Boyer, K. Chatterjee, G. F. Chen, J. L. Luo, N. L. Wang, and E. W. Hudson. Scanning tunneling microscopy of the 32 K superconductor $(Sr_{1-x}K_x)Fe_2As_2$. 2008.

[113] K. Terashima, Y. Sekiba, J. H. Bowen, K. Nakayama, T. Kawahara, T. Sato,

P. Richard, Y. M. Xu, L. J. Li, G. H. Cao, Z. A. Xu, H. Ding, and T. Takahashi. Fermi surface nesting induced strong pairing in iron-based superconductors. *Proc. Natl. Acad. Sci. (USA)*, 106:7330, 2009.

[114] D. J. Singh. Electronic structure and doping in $BaFe_2As_2$ and LiFeAs: Density functional calculations. *Phys. Rev. B*, 78:094511, 2008.

[115] F. Massee, Y. Huang, R. Huisman, S. de Jong, J.B. Goedkoop, and M. S. Golden. Nanoscale superconducting gap variations, strong coupling signatures and lack of phase separation in optimally doped $BaFe_{1.86}Co_{0.14}As_2$. 2008. arXiv:0812.4539.

[116] F. C. Niestemski, V. B. Nascimento, B. Hu, W. Plummer, J. Gillett, S. Sebastian, Z. Q. Wang, and V. Madhavan. Unveiling the atomic and electronic structure at the surface of the parent pnictide $SrFe_2As_2$. 2009. arXiv:0906.2761.

[117] G. Preosti, H. Kim, and P. Muzikar. Density of states in unconventional superconductors: Impurity-scattering effects. *Phys. Rev. B*, 50:1259, 1994.

[118] M. C. Boyer, W. D. Wise, K. Chatterjee, M. Yi, T. Kondo, T. Takeuchi, H. Ikuta, and E. W. Hudson. Imaging the two gaps of the high-temperature superconductor $Bi_2Sr_2CuO_{6+x}$. *Nat. Phys.*, 3:802, 2007.

[119] J.-H. Ma, Z.-H. Pan, F. C. Niestemski, M. Neupane, Y.-M. Xu, P. Richard, K. Nakayama, T. Sato, T. Takahashi, H.-Q. Luo, L. Fang, H.-H. Wen, Z. Wang, H. Ding, and V. Madhavan. Coexistence of competing orders with two energy

gaps in real and momentum space in the high temperature superconductor $Bi_2Sr_{2-x}La_xCuO_{6+\delta}$. *Phys. Rev. Lett.*, 101:207002, 2008.

[120] T. Kondo, R. Khasanov, T. Takeuchi, J. Schmalian, and A. Kaminski. Competition between the pseudogap and superconductivity in the high-T_c copper oxides. *Nature*, 457:296, 2009.

[121] H. Won and K. Maki. d-wave superconductor as a model of high-T_c superconductors. *Phys. Rev. B*, 49:1397, 1994.

[122] M. Kugler, Ø. Fischer, Ch. Renner, S. Ono, and Y. Ando. Scanning tunneling spectroscopy of $Bi_2Sr_2CuO_{6+\delta}$: New evidence for the common origin of the pseudogap and superconductivity. *Phys. Rev. Lett.*, 86:4911, 2001.

[123] U. Essmann and H. Traeuble. The direct observation of individual flux lines in type II superconductors. *Phys. Lett. A*, 24:526, 1967.

[124] H. F. Hess, R. B. Robinson, R. C. Dynes, J. M. Valles, and J. V. Waszczak. Scanning-Tunneling-Microscope observation of the Abrikosov flux lattice and the density of states near and inside a fluxoid. *Phys. Rev. Lett.*, 62:214, 1989.

[125] Ch. Renner, A. D. Kent, Ph. Niedermann, Ø. Fischer, and F. Lévy. Scanning tunneling spectroscopy of a vortex core from the clean to the dirty limit. *Phys. Rev. Lett.*, 67:1650, 1991.

[126] J. Hoffman, K. McElroy, D. H. Lee, K. M. Lang, H. Eisaki, S. Uchida, and J. C. Davis. Imaging quasiparticle interference in $Bi_2Sr_2CaCu_2O_{8+\delta}$. *Science*, 297: 1148, 2002.

[127] A. Grigorenko, S. Bending, T. Tamegai, S. Ooi, and M. Henini. A one-dimensional chain state of vortex matter. *Nature*, 414:728, 2001.

[128] M. R. Eskildsen, L. Ya. Vinnikov, T. D. Blasius, I. S. Veshchunov, T. M. Artemova, J. M. Densmore, C. D. Dewhurst, N. Ni, A. Kreyssig, S. L. Bud'ko, P. C. Canfield, and A. I. Goldman. Vortex studies in superconducting $Ba(Fe_{0.93}Co_{0.07})_2As_2$. *Phys. Rev. B*, 79:100501(R), 2009.

[129] M. Franz, C. Kallin, P. I. Soininen, A. J. Berlinsky, and A. L. Fetter. Vortex state in a d-wave superconductor. *Phys. Rev. B*, 53:5795, 1996.

[130] C. Caroli, P.G. De Gennes, and J. Matricon. Bound Fermion states on a vortex line in a type-II superconductor. *Phys. Lett.*, 9:307, 1964.

[131] J. D. Shore, M. Huang, A. T. Dorsey, and J. P. Sethna. Density of states in a vortex core and the zero-bias tunneling peak. *Phys. Rev. Lett.*, 62:3089, 1989.

[132] F. Gygi and M. Schluter. Electronic tunneling into an isolated vortex in a clean type-II superconductor. *Phys. Rev. B*, 41:822, 1990.

[133] F. Wang, H. Zhai, and D. H. Lee. Antiferromagnetic correlation and the pairing mechanism of the cuprates and iron pnictides: A view from the functional renormalization group studies. *Europhys. Lett.*, 85:37005, 2009.

[134] T. Timusk and B. Statt. The pseudogap in high-temperature superconductors: an experimental survey. *Rep. Prog. Phys.*, 62:61, 1999.

[135] J. X. Li, C. Q. Wu, and D. H. Lee. Checkerboard charge density wave and pseudogap of high-T_c cuprate. *Phys. Rev. B*, 74:184515, 2006.

[136] S. Hefner, M. A. Hossain, A. Damascelli, and G. A. Sawatzky. Two gaps make a high-temperature superconductor? *Rep. Prog. Phys.*, 71:062501, 2008.

[137] A. J. Millis. Gaps and our understanding. *Science*, 314:1888, 2006.

[138] W. W. Warren Jr., R. E. Walstedt, G. F. Brennert, R. J. Cava, R. Tycko, R. F. Bell, and G. Dabbagh. Cu spin dynamics and superconducting precursor effects in planes above Tc in $YBa_2Cu_3O_{6.7}$. *Phys. Rev. Lett.*, 62:1193, 1989.

[139] R. E. Walstedt, W. W. Warren Jr., R. F. Bell, R. J. Cava, G. P. Espinosa, L. F. Schneemeyer, and J. V. Waszczak. 63Cu NMR shift and linewidth anomalies in the $T_c = 60$ K phase of Y-Ba-Cu-O. *Phys. Rev. B*, 41:9574, 1990.

[140] C. C. Homes, T. Timusk, R. Liang, D. A. Bonn, and W. N. Hardy. Optical conductivity of c axis oriented $YBa_2Cu_3O_{6.70}$: Evidence for a pseudogap. *Phys. Rev. Lett.*, 71:1645, 1993.

[141] J. W. Loram, K. A. Mirza, J. R. Cooper, W. Y. Liang, and J. M. Wade. Electronic specific heat of $YBa_2Cu_3O_{6+x}$ from 1.8 to 300 K. *J. Supercond.*, 7: 243, 1994.

[142] A. G. Loeser, Z. X. Shen, D. S. Dessau, D. S. Marshall, C. H. Park, P. Fournier, and A. Kapitulnik. Excitation gap in the normal state of underdoped $Bi_2Sr_2CaCu_2O_{8+\delta}$. *Science*, 273:325, 1996.

[143] H. Ding, T. Yokoya, J. C. Campuzano, T. Takahashi, M. Randeria, M. R. Norman, T. Mochiku, K. Kadowaki, and J. Giapintzakis. Spectroscopic evidence

for a pseudogap in the normal state of underdoped high-tc superconductors. *Nature*, 382:51, 1996.

[144] A. Damascelli, Z. Hussain, and Z. X. Shen. Angle-resolved photoemission studies of the cuprate superconductors. *Rev. Mod. Phys.*, 75:473, 2003.

[145] M. Norman, H. Ding, M. Randeria, J. C. Campuzano, T. Yokoya, T. Takeuchi, T. Takahashi, T. Mochiku, K. Kadowaki, P. Guptasarma, and D.G. Hinks. Destruction of the Fermi surface in underdoped high-Tc superconductors. *Nature*, 392:157, 1998.

[146] J. M. Harris, P. J. White, Z. X. Shen, H. Ikeda, R. Yoshizaki, H. Eisaki, S. Uchida, W. D. Si, J. W. Xiong, Z. X. Zhao, and D. S. Dessau. Anomalous superconducting state gap size versus tc behavior in underdoped $Bi_2Sr_2Ca_{1-x}Dy_xCu_2O_{8+\delta}$. *Phys. Rev. B*, 54:R15665, 1996.

[147] P. A. Lee. From hign temperature superconductivity to quantum spin liquid: progress in strong correlation physics. *Rep. Prog. Phys.*, 71:012501, 2008.

[148] J. Orenstein and A. J. Millis. Advances in the physics of high-temperature superconductivity. *Science*, 288:468, 2000.

[149] J. Corson, R. Mallozzi, J. Orenstein, J. N. Eckstein, and I. Bozovic. Vanishing of phase coherence in underdoped $Bi_2Sr_2CaCu_2O_{8+\delta}$. *Nature*, 398:221, 1999.

[150] Z. A. Xu, N. P. Ong, Y. Wang, T. Kakeshita, and S. Uchida. Vortex-like excitations and the onset of superconducting phase fluctuation in underdoped $La_{2-x}Sr_xCuO_4$. *Nature*, 406:486, 2000.

[151] K. Tanaka, W. S. Lee, D. H. Lu, A. Fujimori, T. Fujii, Risdiana, I. Terasaki, D. J. Scalapino, T. P. Devereaux, Z. Hussain, and Z. X. Shen. Distinct Fermi-momentum-dependent energy gaps in deeply underdoped Bi2212. *Science*, 314: 1910, 2006.

[152] M. Le Tacon, A. Sacuto, A. Georges, G. Kotliar, Y. Gallais, D. Colson, and A. Forget. Two energy scales and two distinct quasiparticle dynamics in the superconducting state of underdoped cuprates. *Nat. Phys.*, 2:537, 2006.

[153] T. Kondo, T. Takeuchi, U. Mizutani, T. Yokoya, S. Tsuda, and S. Shin. Contribution of electronic structure to thermoelectric power in $(Bi,Pb)_2(Sr,La)_2CuO_{6+\delta}$. *Phys. Rev. B*, 72:024533, 2005.

[154] B. W. Hoogenboom, K. Kadowaki, B. Revaz, and Ø. Fischer. Homogeneous samples of $Bi_2Sr_2CaCu_2O_{8+\delta}$. *Physica C*, 391:376, 2003.

[155] Kyle McElroy. *Scanning Tunneling Microscopy Studies in both Real- and Momentum-space of the Doping Dependence of Cuprate Electronic Structure*. PhD thesis, University of California at Berkeley, 2005.

[156] K. McElroy, J. Lee, J. A. Slezak, D. H. Lee, H. Eisaki, S. Uchida, and J. C. Davis. Atomic-scale sources and mechanism of the nanoscale electronic disorder in $Bi_2Sr_2CaCu_2O_{8+\delta}$. *Science*, 309:1048, 2005.

[157] W. D. Wise, K. Chatterjee, M. C. Boyer, T. Kondo, T. Takeuchi, H. Ikuta, Z. J. Xu, J. S. Wen, G. D. Gu, Y. Y. Wang, and E. W. Hudson. Imaging nanoscale

Fermi-surface variations in an inhomogeneous superconductor. *Nat. Phys.*, 5: 213, 2009.

[158] D. L. Feng, D. H. Lu, K. M. Shen, C. Kim, H. Eisaki, A. Damascelli, R. Yoshizaki, J. i. Shimoyama, K. Kishio, G. D. Gu, S. Oh, A. Andrus, J. O'. Donnell, J. N. Eckstein, and Z. X. Shen. Signature of superfluid density in the single-particle excitation spectrum of $Bi_2Sr_2CaCu_2O_{8+\delta}$. *Science*, 289:277, 2000.

[159] A. N. Pasupathy, A. Pushp, K. K. Gomes, C. V. Parker, J. S. Wen, Z. J. Xu, G. D. Gu, S. Ono, Y. Ando, and A. Yazdani. Electronic origin of the inhomogeneous pairing interaction in the high-T_c superconductor $Bi_2Sr_2CaCu_2O_{8+\delta}$. *Science*, 320:196, 2008.

[160] G. Grüner. *Density waves in solids.* Perseus publishing, Cambridge, Massachusetts, 1st edition, 1994.

[161] Eric Hudson. *Investigating High-T_c superconductivity on the Atomic scale by Scanning Tunneling Microscopy.* PhD thesis, University of California at Berkeley, 1999.

[162] G. E. Volovik. Superconductivity with lines of GAP nodes: density of states in the vortex. *JEPT Lett.*, 58:469, 1993.

[163] K. Kudo, Y. Miyoshi, T. Sasaki, and N. Kobayashi. Hole-doping and magnetic-field effects on the pseudogap in $Bi_{1.74}Pb_{0.38}Sr_{1.88}CuO_{6+\delta}$ studied by the out-of-plane resistivity. *Physica C*, 426:251, 2005.

[164] G. Briceo, M. F. Crommie, and A. Zettl. Giant out-of-plane magnetoresistance in Bi-Sr-Ca-Cu-O: A new dissipation mechanism in copper-oxide superconductors? *Phys. Rev. lett.*, 66:2164, 1991.

[165] T. Shibauchi, L. Krusin-Elbaum, M. Li, M. P. Maley, and P. H. Kes. Closing the pseudogap by zeeman splitting in $Bi_2Sr_2CaCu_2O_{8+\delta}$ at high magnetic fields. *Phys. Rev. lett.*, 86:5763, 2001.

[166] K. Deligiannis, P. A. J. de Groot, M. Oussena, S. Pinfold, R. Langan, R. Gagnon, and L. Taillefer. New features in the vortex phase diagram of $YBa_2Cu_3O_{7-\delta}$. *Phys. Rev. lett.*, 79:2121, 1997.

[167] N. Morozov, L. Krusin-Elbaum, T. Shibauchi, L. N. Bulaevskii, M. P. Maley, Yu. I. Latyshev, and T. Yamashita. High-field quasiparticle tunneling in $Bi_2Sr_2CaCu_2O_{8+\delta}$: Negative magnetoresistance in the superconducting state. *Phys. Rev. lett.*, 84:1784, 2000.

[168] Ch. Renner, B. Revaz, K. Kadowaki, I. Maggio-Aprile, and Ø. Fischer. Observation of the low temperature pseudogap in the vortex cores of $Bi_2Sr_2CaCu_2O_{8+\delta}$. *Phys. Rev. Lett.*, 80:3606, 1998.

[169] D. L. Feng, A. Damascelli, K. M. Shen, N. Motoyama, D. H. Lu, H. Eisaki, K. Shimizu, J. i. Shimoyama, K. Kishio, N. Kaneko, M. Greven, G. D. Gu, X. J. Zhou, C. Kim, F. Ronning, N. P. Armitage, and Z. X. Shen. Electronic structure of the trilayer cuprate superconductor $Bi_2Sr_2Ca_2Cu_3O_{10+\delta}$. *Phys. Rev. Lett.*, 88:107001, 2002.

[170] M. Vershinin, S. Misra, S. Ono, Y. Abe, Y. Ando, and A. Yazdani. Local ordering in the pseudogap state of a high-tc superconductor $Bi_2Sr_2CaCu_2O_{8+\delta}$. *Science*, 303:1995, 2004.

[171] Y. J. Uemura *et al.* Universal correlations between T_c and n_s/m^* (carrier density over effective mass) in high-Tc cuprate superconductors. *Phys. Rev. Lett.*, 62: 2317, 1988.

[172] W. N. Hardy, D. A. Bonn, D. C. Morgan, R. X. Liang, and K. Zhang. Precision measurements of the temperature dependence of λ in $YBa_2Cu_3O_{6.95}$: Strong evidence for nodes in the gap function. *Phys. Rev. Lett.*, 70:3999, 1993.

[173] J. M. Kosterlitz and D. J. Thouless. Ordering, metastability and phase transitions in two-dimensional systems. *J. Phys. C*, 6:1181, 1973.

[174] V. Galitski and S. Sachdev. Paired electron pockets in the hole-doped cuprates. *Phys. Rev. B*, 79:134512, 2009.

[175] P. A. Lee T. Senthil. A synthesis of the phenomenology of the underdoped cuprates. 2009. arXiv:0903.0870.

[176] R. Corcoran, N. Harrison, C. J. Haworth, S. M. Hayden, P. Meeson, M. Springford, and P. J. van der Wel. De Haas-van Alphen effect in the superconducting state. *Physica B*, 206:534, 1995.